Diagnostic Development and Plasma-Material Interaction Studies on the ZaP-HD Device

Eleanor Forbes

A dissertation
submitted in partial fulfillment of the
requirements for the degree of

Doctor of Philosophy

University of Washington

2020

Reading Committee:

Uri Shumlak, Chair

Brian Nelson

Eric Meier

Program Authorized to Offer Degree:
Aeronautics and Astronautics

University of Washington

Abstract

Diagnostic Development and Plasma-Material Interaction Studies on the ZaP-HD Device

Eleanor Forbes

Chair of the Supervisory Committee:
Professor and Associate Chair for Research Uri Shumlak
Aeronautics and Astronautics

The ZaP-HD Flow Z-Pinch device was designed to investigate the use of a tri-axial electrode configuration to scale a sheared-flow stabilized Z pinch to high energy density conditions. Decoupling the power used to form the plasma from the power used to compress the pinch has resulted in temperatures and densities of 1 keV and 1×10^{18} cm^{-3} during quiescent periods of up to 60 μs. After demonstrating improved performance through the use of two power supplies, the ZaP-HD machine has seen further use as a test-bed for diagnostic development and high energy density plasma-material interactions (PMI). Two novel diagnostics have been fielded on the ZaP-HD machine: time-resolved spectroscopy and three-dimensional digital holographic interferometry (DHI). Time-resolved spectroscopy is used to make simultaneous measurements of plasma temperature and velocity over the course of the plasma lifetime. Three-dimensional DHI is used to reconstruct the full 3D electron density structure of approximately three centimeters of the length of the Z-pinch. These two diagnostics used in concert with magnetic field probes and other measurements provide a detailed history of the Z-pinch behavior and give comprehensive information on the variation in pinch performance with initial conditions.

A series of experiments were performed to better understand the role of plasma kinetic and thermal energy in material target deformation in high-energy density plasmas. Graphite and boron-nitride targets were exposed to plasmas of varying temperatures and velocities.

Plasma behavior was monitored with a diagnostic suite and the targets were examined with high-resolution surface diagnostics to characterize any deformation caused by plasma exposure. Significant differences in the surface structure are seen for graphite targets. Features vary with plasma ion energy and with orientation to the plasma flow. Energy deposition and sputtering yield are calculated for various parameters. Targets exposed to high-energy plasma pulses are found to exceed the BN and graphite sublimation temperature. The data are used to calculate graphite erosion times and may be useful for designing electrodes on future experiments and reactor concepts.

TABLE OF CONTENTS

LIST OF FIGURES

LIST OF TABLES

ACKNOWLEDGMENTS

This work would not have been completed without my vast and uwavering support network. First, I wish to thank my adviser, Professor Uri Shumlak, for supporting me throughout my undergraduate and graduate studies at the University of Washington. He is a fierce advocate for students, an excellent teacher, and a good friend and mentor. I will miss his advice and humor, and I hope our professional paths cross again. I would like to thank Dr. Michael Ross, who was my first mentor in the lab and inspired me to pursue a graduate degree. He and Michal Hughes were my first plasma physics teachers and both remain my good friends. I also owe gratitude to Professor Brian Nelson, Dr. Eric Meier, Dr. Raymond Golingo, Dr. Tobin Weber, Dr. Anton Stepanov, and Dr. Yue Zhang, who all provided training, assistance, and advice to me during my time at the lab. Special acknowledgement goes to Scott Braswell and the UW Molecular Analysis Facility for training and use of their equipment to collect the micrographs shown in this thesis.

The encouragement of my friends and family has been paramount to finishing my graduate work. My parents, god-parents, and extended family have provided much love and practical guidance. I would also like to thank my friends and coworkers Jennifer Garner, Steven Robinson, Chayse Aubuchon, Anna Sheppard, Shawn Doty, Elliot Claveau, Michael O'Dell, Aqil Khairi, and many more, for providing levity and camraderie when I needed it most. Finally, I would like to thank my partner, Justin Carpenter, for standing by me through the entire process of earning this degree and doing dishes while I stayed up late finishing my homework.

DEDICATION

To mom and dad. Thank you for everything.

Chapter 1

INTRODUCTION

Since the discovery of fusion reactions in the early twentieth century, humankind has aspired to harness fusion as a means to produce near-limitless energy on earth and to power manned space exploration. Controlled fusion has proven to be one of the most challenging problems tackled by scientists. Surmounting this challenge and providing clean, plentiful energy to the world will undoubtedly be one of the greatest achievements of the human race. However, this discovery will not come from a single "Eureka!" moment, but rather it will result from the collective incremental contributions of scientists and engineers across the globe. This body of work aims to become one of those small, incremental contributions that will help shape humanity's future.

The research presented in this dissertation shows increased plasma parameters from the ZaP Experiment, expands our ability to measure plasma parameters in pulsed, high energy experiments, and develops an understanding of some plasma-material interactions occurring the the ZaP-HD Device. Measurements from multiple diagnostics demonstrate that higher ion temperatures and electron densities are achieved with the tri-axial electrode configuration used on the ZaP-HD Device. All experiments were performed at the ZaP-HD Flow Z-Pinch Experiment at the University of Washington. Two novel diagnostics, a spatially and temporally-resolved ion Doppler spectrometer, and a three-dimensional digital holographic interferometer, were developed using ZaP-HD as a test bed. Plasma-material interaction studies used ZaP-HD as a plasma jet source to bombard targets with high-temperature protons. The results of these experiments will help to guide and diagnose the next generation of flow Z-pinch devices as ZaP Energy, Inc. begins the development of a prototype reactor.

1.1 Z Pinch Historical Context and Theory

The Z pinch is among the oldest and simplest methods of confining a plasma. Since the 1950's, Z pinches have been researched as a physics test bed and platform for magnetically confined fusion. Initial experiments investigated the compression of plasma filaments through high-current discharges in static rarefied gases [3]. Since that time, Z-pinch experiments have drastically increased in scale to produce some of the highest temperatures achieved by human-made devices. The largest of these is the Z-machine at Sandia National Labs, which uses a 22 MJ capacitor bank to drive 26 MA of current through a wire array, forming a pinch for approximately 2 ns [6]. These energy-dense pinches are used primarily to validate data from computer simulations of nuclear weapon explosions. While the conditions generated in Z are scientifically interesting, applying this technique practically is challenging as the installation of the array limits the experimental repetition rate to less than one plasma pulse per day.

Unlike wire array pinch experiments, the ZaP experiment has its roots in the work of John Marshall. Marshall experimented with a coaxial plasma accelerator, achieving 200 kA of current and an axial flow velocity around 1.5×10^5 m/s [35]. A geometry very similar to this coaxial accelerator is used to form the ZaP Z pinch and impart the flow shear necessary for pinch stability, which is discussed later in this chapter.

The simple geometry of the Z pinch is likely in part what made it attractive to early plasma physicists. Using a self-generated magnetic field, a linear column of plasma can be compressed to high energy density conditions. A diagram of the Z-pinch geometry is shown in Fig. 1.1. The magnetic pressure balances the plasma pressure and is described by the static Z-pinch equilibrium equation

$$\frac{d}{dr}\left(P + \frac{B_\theta^2}{2\mu_0}\right) = \frac{B_\theta^2}{\mu_0 r}. \tag{1.1}$$

The Z pinch is an attractive confinement option for fusion reactors because it requires no external magnetic field coils. However, the Z pinch is susceptible to pressure-driven

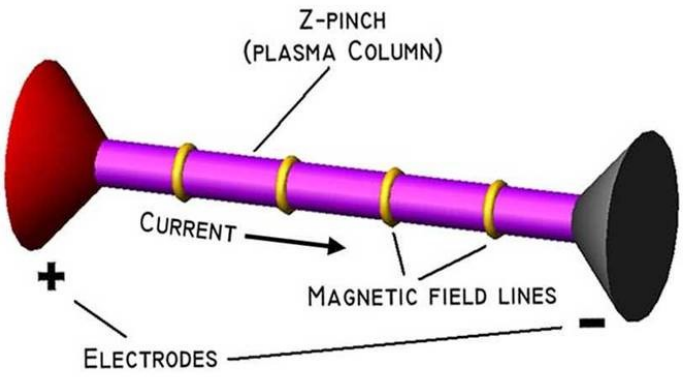

Figure 1.1: A diagram of the Z-pinch geometry. Current flowing through the plasma column generates an azimuthal magnetic field which balances the plasma pressure.

instability modes that make it difficult to sustain the plasma for longer than an instability growth time. The $m = 0$ sausage mode is caused by a constriction of the pinch at one axial location which results in an increased local magnetic field. This positive feedback loop continues to decrease the plasma radius until confinement is lost. The m = 1 kink mode is the result of a bend forming in the plasma, creating a larger magnetic field in regions of inward curvature. The bending increases until the kink breaks the plasma column and disrupts the pinch current. A diagram of these two instabilities is shown in Fig. 1.2. Both instability modes result in a rapid loss of confinement of the pinch on the order of an Alfvén transit time.

1.2 Z Pinch Stability

There are several known methods of stabilizing the Z pinch. Embedding an axial magnetic field, B_z, creates the magnetic shear necessary to stabilize the instability modes. This method

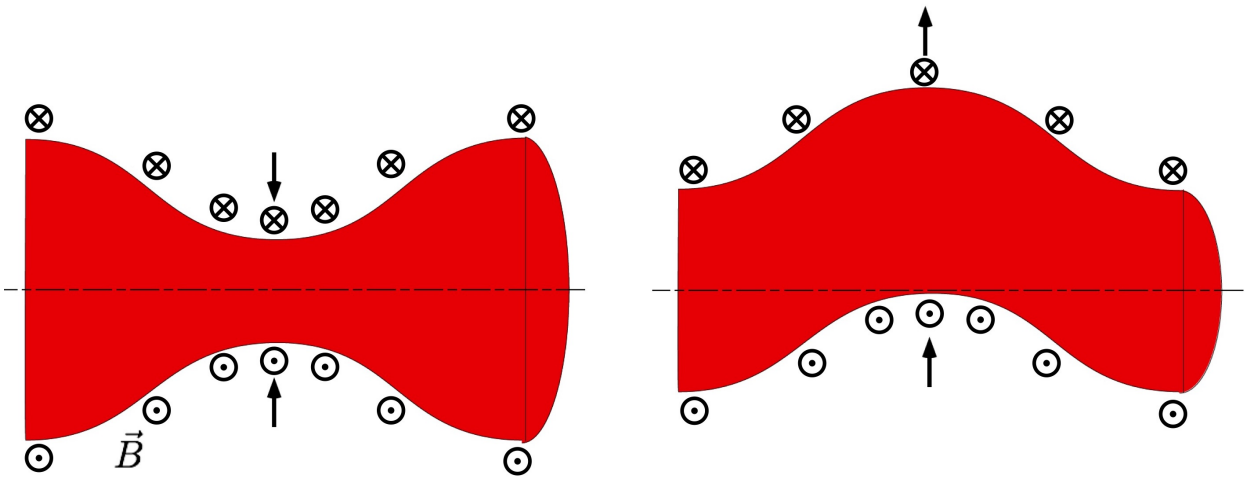

Figure 1.2: A diagram of static Z-pinch instabilities. The left hand side shows the $m = 0$ sausage instability. A slight local decrease in radius results in an increased local magnetic field which continues to pinch the plasma column until the current path breaks. The right image shows the $m = 1$ kink instability. A perturbation causes a bend in the plasma column which increases the magnetic field in regions of inward curvature and reduces field in regions of outward curvature. This causes the bending to increase until the current is disrupted.

restricts the maximum axial current and pressure, set by the Kruskal-Shafranov limit

$$\frac{B_\theta}{B_z} < \frac{2\pi a}{L} \tag{1.2}$$

where L is the pinch length and a is the pinch radius [49]. It also opens field lines, allowing energy to escape the equilibrium resulting in end losses and heating of the electrodes. In addition, the method requires external field coils, which increases the size and cost of an experimental device or fusion reactor.

Surrounding the plasma with a close conducting wall is another method of stabilizing the Z pinch. The plasma generates image currents in the wall which oppose m=0 and m=1 instabilities as they arise. To provide stability, the conducting wall must be located very close to the pinch, $r_w/a = 1.2$, where r_w is the wall radius and a is the plasma radius [1]. In a typical ZaP-HD plasma pulse, the pinch radius is on the order of three millimeters. A stabilizing wall would be subjected to extreme temperatures and energy fluxes from fusion plasmas, rendering this method unsuitable for experimental and reactor applications.

The $m = 0$ mode can be mitigated by controlling the radial pressure profile. By applying a functional minimization of the linear magnetohydrodynamic (MHD) equations, Kadomtsev showed the stability criterion to be

$$-\frac{d\ln p}{d\ln r} \leq \frac{4\gamma}{2+\gamma\beta} \tag{1.3}$$

where β is the ratio of the plasma pressure to the magnetic pressure

$$\beta = \frac{2\mu_0 p}{B^2} \tag{1.4}$$

and γ is the ratio of the specific heats $\gamma = C_p/C_v$ [27]. Here μ_0 is the permeability of free space and p is the plasma pressure $p = nk_BT$ where k_B is the Boltzmann constant. This shows that a pressure profile with a sufficiently gradual slope will stabilize the pinch against sausage modes. There is no effect on the kink mode instability.

1.3 Sheared Flow Stabilization

Another method of stabilizing the Z pinch to pressure-driven instabilities is through the application of radial shear to the axial flow velocity, v_z. A numerical linear stability analysis of the MHD equations has shown that the radial shear must be above the threshold [1]

$$\frac{dv_z}{dr} \geq 0.1kV_a \tag{1.5}$$

where k is the instability wavenumber and V_A is the Alfvén velocity given by

$$V_A = \frac{B_0}{\sqrt{\mu_0 \rho_0}} \tag{1.6}$$

where ρ_0 is the plasma mass density. Should an instability begin to arise, the radial shear creates a phase mismatch in the instability, effectively smoothing it and preventing further growth.

A cartoon of sheared velocity flow stabilizing a sausage instability is shown in Fig. 1.3.

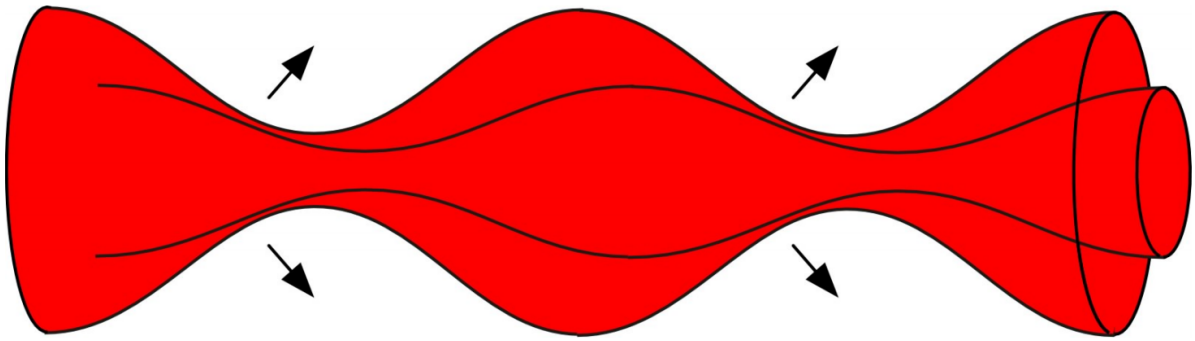

Figure 1.3: A cartoon of sheared flow stabilizing a sausage instability. In this case, the faster moving interior column pushes the pinched portions of the exterior column outward, effectively mixing the phases of the instability. This prevents the increasing magnetic pressure from further pinching the plasma.

This shear must be maintained along the entire axial extent of the pinch. This method been shown experimentally to stabilize a Z pinch for thousands of instability growth times [52].

1.4 Applications of the Shear Flow Stabilized Z Pinch

1.4.1 Thermonuclear Fusion Energy

The size and simplicity of the Z pinch makes it an attractive platform for a magnetically-confined fusion reactor. Compact Z-pinch reactors could replace humanity's need for unsustainable energy sources such as natural gas and coal. Power from fusion reactors could ultimately be extracted using the same methods as conventional systems, namely through steam generators, which could facilitate a relatively easy transition to a fusion-powered grid.

Nuclear fusion is the process of releasing energy by two or more atomic nuclei colliding and combining. Normally, atomic nuclei repel each other due to the Coulomb force. However, if the two nuclei move close enough together, the strong nuclear force overcomes the Coulomb force and the nuclei fuse. A fusion of light elements that produces a nucleus lighter than iron-56 or nickel-62 will generally yield a net energy release. The energy released in a fusion reaction is much greater than that released in a chemical reaction, since the binding energy of a nucleus is much greater than the energy holding the electrons to the nuclei. Several fusion reactions that have been proposed for use in reactors are listed in Table 1.1.

The reaction that requires the lowest temperature to produce peak fusing rate is deuterium-tritium. These are the proposed working gases for the fusion Z-pinch reactor. A diagram of the reactor design is shown in Fig. 1.4. A deuterium-tritium gas mixture is puffed into the annulus between concentric electrode and ionized, creating a current sheet that runs down the electrodes and forms a pinch. Conditions in the pinch cause the D-T to fuse, producing helium and neutrons. The neutrons impact a liquid Pb-Li or Sn-Li blanket and heat the liquid metal. The hot metal is pumped to a steam generator, where the thermal energy is converted into electrical energy. Impacts between neutrons and lithium in the liquid blanket produce more tritium to sustain the supply for the power plant. The breeding

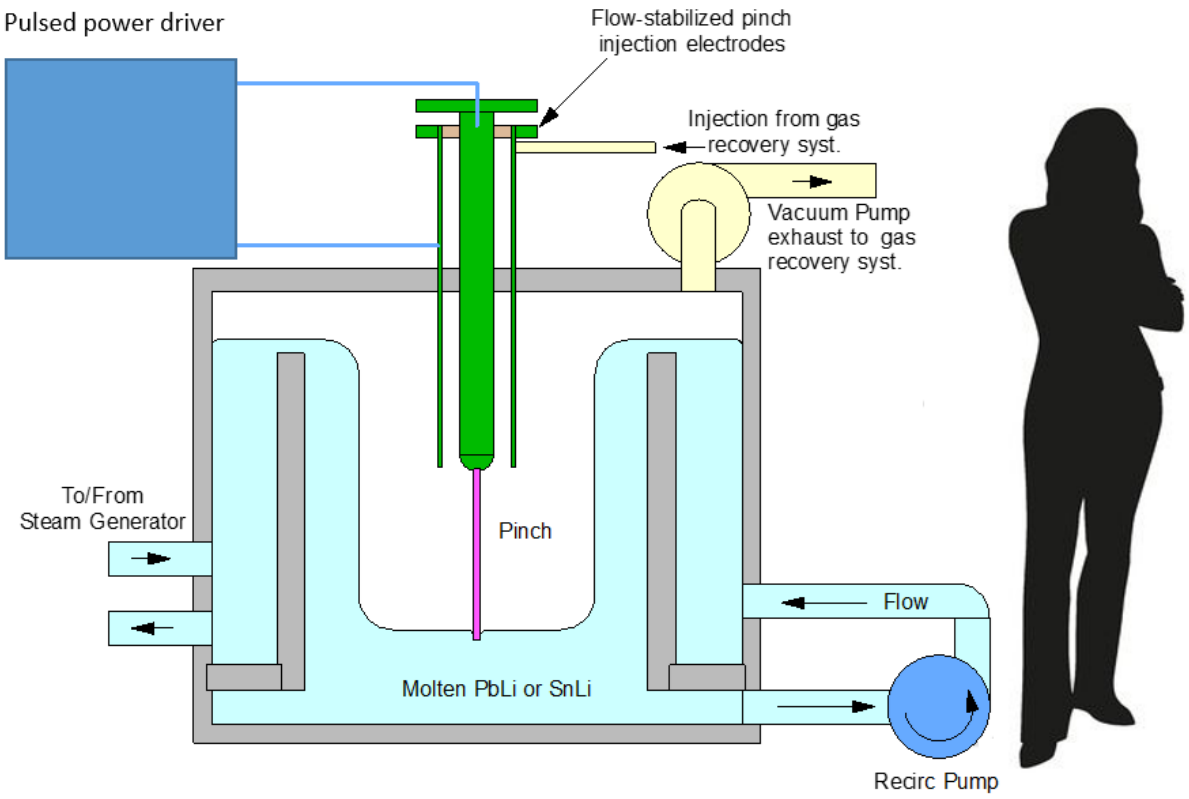

Figure 1.4: A concept for a Z pinch fusion reactor with a scientist for scale. Deuterium and tritium gas is ionized by a pulsed power driver and accelerated into a pinch formation. Molten Pb-Li or Sn-Li acts as a third electrode and heat transfer fluid. Remaining deuterium and any helium and tritium produced are extracted and recovered to be recycled or stored. The molten metal is pumped to a steam generator where the heat is converted into electrical energy.

Reactants	Products
D + D →	T (1.01 MeV) + p (3.02 MeV)
→	^{3}He (0.82 MeV) + n (2.45 MeV)
D + T →	^{4}He (3.52 MeV) + n (14.1 MeV)
D + ^{3}He →	^{4}He (3.6 MeV) + p (14.7 MeV)
p + ^{6}Li →	^{4}He (1.72 MeV) + ^{3}He (2.3 MeV)
p + ^{11}B →	3^{4}He (8.7 MeV)

Table 1.1: Selected fusion reactions and their products.

process is crucial to producing enough tritium fuel to support reactor operations.

1.4.2 Deep Space Propulsion

The requirements of traveling to the outer reaches of our solar system necessitate developing new methods of space propulsion beyond conventional rockets. Chemical rockets are limited by the energy released from burning fuel. Electric propulsion devices can impart more energy to propellants, but are limited by the power supply used to ionize and accelerate the fuel. Using a fusing plasma as a platform for space propulsion would provide the power and propellant in one system. A fusion system could provide much higher energies and exhaust velocities than current electric propulsion systems while using much less fuel than a chemical rocket.

Increasing exhaust velocities beyond those achieved by chemical rockets is imperative to reducing the fuel mass needed for spacecraft missions. The fuel mass is related to exhaust velocity through the rocket equation

$$\frac{m_0}{m_f} = \exp\left(\frac{\Delta V}{c_e}\right) \tag{1.7}$$

where m_0 is the initial mass, m_f is the final mass, ΔV is the required change in velocity for executing a spacecraft maneuver, and c_e is the exhaust velocity. As the energy required for

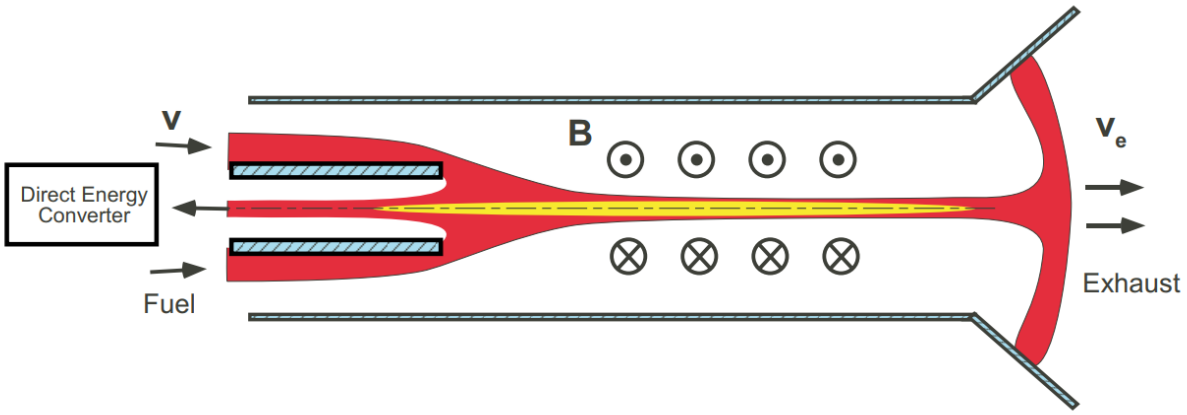

Figure 1.5: Schematic of a fusion Z-pinch thruster. Fusing propellant is exhausted through an expanding nozzle to the right. Some fusion power is diverted to an energy converter to power the rest of the spacecraft. This concept can achieve temperatures and densities to produce aneutronic $p - B^{11}$ fusion reactions [51].

the mission increases, the initial fuel mass increases exponentially. Higher exhaust velocities lower the required mass.

A flow Z pinch could be implemented as a fusion thruster. This concept would provide the propulsion and power system for a spacecraft. A schematic is shown in Fig. 1.5. Fuel is ionized and compressed into a Z pinch in an identical method to the reactor concept. Some of the energy from the fusion reactions is captured using a direct energy converter and used to power other spacecraft systems. In this case, instead of impinging on a flowing metal wall, the fusing plasma is directed out of the chamber through a nozzle. As the exhaust expands, the propellant cools and the charged particles recombine into neutrals. This thruster is capable of achieving exhaust velocities of 1×10^6 m/s and thrusts of 1×10^5 N even when operated in a pulsed configuration [51].

The design for this fusion-based thruster has advantages over other fusion-based propulsion systems. Z pinches require no applied magnetic fields which reduces the thruster mass.

In addition, the high confinement of the Z pinch allows $p - B^{11}$ fuel to be used, which produces aneutronic fusion reactions. This eliminates the requirement for heavy neutron shielding on the spacecraft, further reducing the weight.

Chapter 2

THE ZAP-HD FLOW Z-PINCH EXPERIMENT

The ZaP-HD device was designed to investigate the scaling of a sheared flow stabilized Z pinch to high energy density (HED) conditions. In order to drive higher currents in the pinch, two separate power supplies are used to decouple the power used to ionize and accelerate the plasma from the power used for pinch compression and confinement. This is accomplished in the experiment by using three electrodes. A cross section of the ZaP-HD electrode configuration is shown in Fig. 2.1.

2.1 Operational Overview of the ZaP-HD Device

The formation of a Z pinch in the ZaP-HD device begins with neutral gas injection in the acceleration region. Gas is injected at two separate locations: from one valve with eight exhaust ports located inside the inner electrode 50 cm upstream of the nosecone, and from eight valves 95 cm upstream of the nosecone. A 680 μF capacitor bank with a 90 μs half-cycle time is used to ionize the gas and accelerate it axially along the meter-long acceleration region via the Lorentz force. Upon exiting the acceleration region plasma compresses radially to form a pinch and the axial flow is maintained. A second 680 μF capacitor bank is used to apply voltage across the inner and outer electrodes, compressing the pinch on axis. Additional flowing plasma is supplied from the acceleration region throughout the pulse to provide the radial shear of the axial velocity necessary to sustain the pinch. A diagram of the pinch formation and compression is shown in Fig. 2.2.

The short lifetime and extreme temperatures of the plasma necessitate the use of passive diagnostics capable of sub-microsecond time resolution. It is paramount to understand how

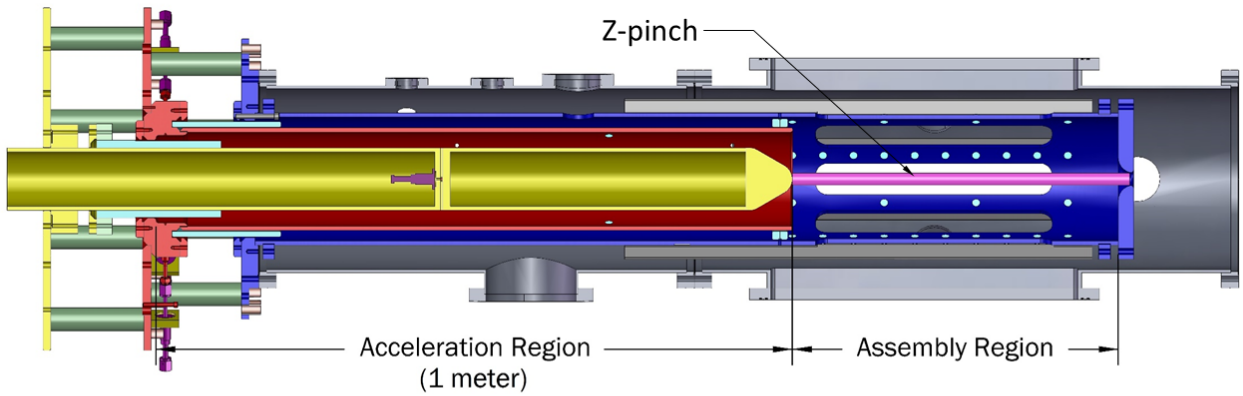

Figure 2.1: A cross section of the ZaP-HD experiment. The inner, middle, and outer electrodes are shown in yellow, red, and blue respectively. The vacuum chamber is shown in gray and the plasma in pink. Neutral gas is injected at two locations between the inner and middle electrodes in the acceleration region. A single valve injects gas 50 cm upstream of the nosecone tip, and an array of eight gas puff valves inject gas above the insulator 95 cm upstream of the nosecone tip. The valves are shown here in purple and the insulator in light green. The cyan circles indicate the locations of embedded magnetic field probes in the assembly region. Additional probes are set into a linear array along the acceleration region.

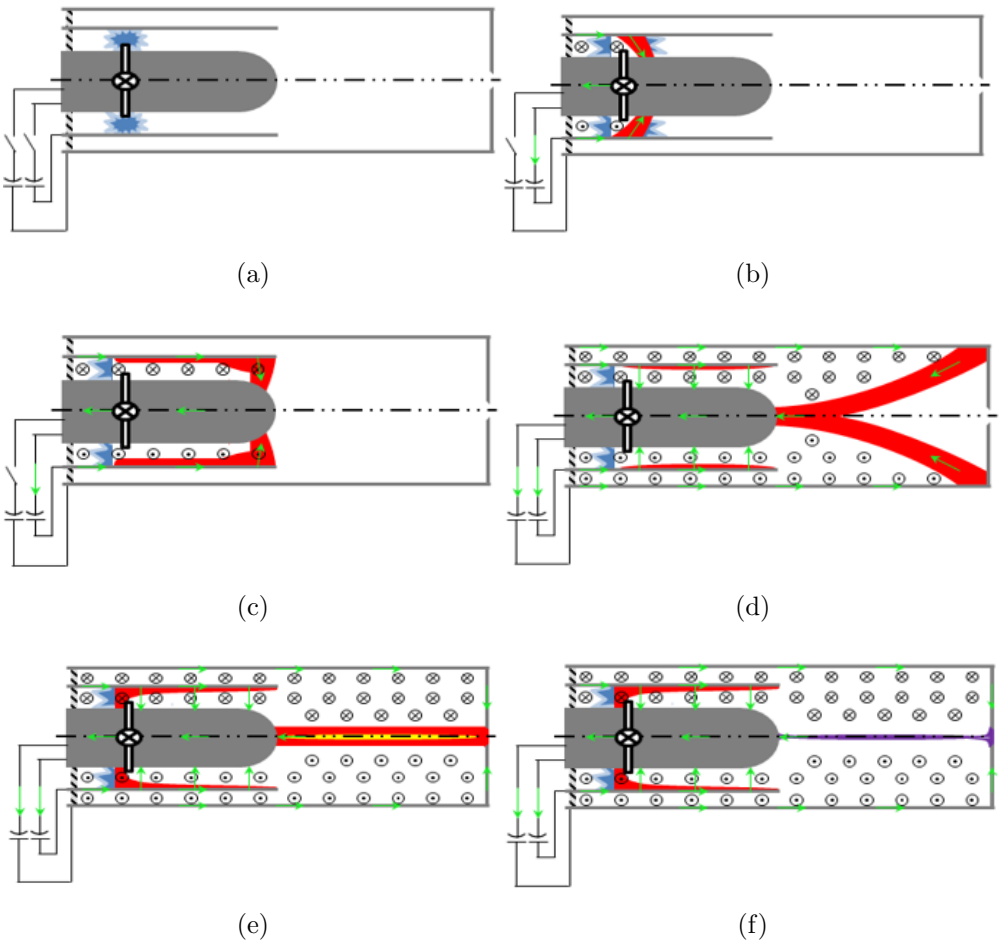

Figure 2.2: Details of the formation process of the ZaP-HD Z pinch. (a) Neutral gas is puffed into the annular gap between the middle and inner electrodes. (b) An ignitron is triggered to apply a voltage across the inner and middle electrode. The capacitor voltage causes the gas to break down and form a current sheet. The plasma is accelerated via the Lorentz force down the experiment, leaving some residual gas in the acceleration region. (c) The plasma forms a snowplow front as it is accelerated down the electrode. (d) A second set of ignitrons is engaged to apply a voltage between the inner and outer electrode to compress the pinch. (e) Residual gas supplies the pinch with additional flowing plasma. (f) Pinch current compresses and heats the plasma.

initial conditions such as the amount of gas and the current waveform affect plasma longevity, temperature, density, and radius. Without characterizing the plasma scaling and the effects of engineering variables such as machine geometry, the sheared flow stabilized Z pinch cannot be used in the applications described in Chapter 1. Plasma temperature, density, and lifetime are particularly important to fusion applications where a hot, dense plasma is required to facilitate fusion reactions. The product of density, temperature, and time is called the triple product, which for steady-state devices is expressed as

$$nT\tau_E \geq \frac{12k_B}{E_{ch}}\frac{T^2}{\langle\sigma v\rangle} \tag{2.1}$$

where τ_E is the energy confinement time, E_{ch} is the energy of charged fusion products, and $\langle\sigma v\rangle$ is the cross section. A fusing plasma must meet the triple product criteria to attain ignition, that is, to maintain the plasma temperature against all losses. While a Z-pinch configuration that meets the required triple product for ignition will likely never be achieved in the ZaP lab, understanding the physics of ZaP-HD through experimental measurements will facilitate the construction of such a device in the future.

2.2 Diagnostic Suite

ZaP-HD has an extensive diagnostic suite to characterize the pinch throughout the pulse. Some diagnostics, such as magnetic field probes, are embedded in the machine, while others require optical access through the large rectangular windows in the machine assembly region. Current, voltage, and magnetic field probe measurements indicate the spatiotemporal evolution of the magnetic field topography. Spectroscopy measures the Doppler broadening of impurity line radiation to determine ion temperature and velocity. Digital holographic interferometry (DHI) is used to record a two-dimensional electron density measurement at one point in time during each plasma pulse. A fast-framing camera records visible light emission from the plasma to provide a qualitative measure of plasma performance. The use of these diagnostics in concert resolves the plasma behavior over the pinch lifetime.

2.2.1 Current and Voltage Measurements

The plasma current, compression current, and capacitor bank currents are measured on ZaP-HD using Rogowski coils. The Rogowski coils are constructed from 32-gauge magnet wire tightly coiled around the insulator of a coaxial cable. A BNC plug is attached to the end of each cable. The Rogowski coils are attached to the experiment to enclose the current to be measured. The current passing through the center of the coil generates a time-changing magnetic field. By Faraday's law, the changing magnetic flux through the loops of wire in the Rogowski cable generate a voltage at the coil terminals

$$V_{meas} = -\frac{d\Phi}{dt} = -\mu_0 n A \frac{dI}{dt} \tag{2.2}$$

where $n = N/l$, the total number of turns N divided by the length of the Rogowskii coil l, and A is the coil area. The current passing through the coil is found by integrating this voltage signal. Figure 2.3 shows a simple diagram of how a Rogowski coil is wound.

There are six Rogowski coils in use on the ZaP-HD experiment. Three provide a measure of the current through each ignitron switch on the capacitor banks (one for the acceleration bank and two for the compression bank). Two Rogowski coils measure total plasma current and compression current. The acceleration current is inferred by subtracting the compression current from the total plasma current. A single Rogowski coil is embedded in the end wall of the outer electrode around a hole through which plasma can exhaust. This coil is designed to measure any plasma flowing through the hole in the end wall.

The voltage across each electrode pair is measured by connecting 500 Ω high power carborundum resistors between the electrodes. A small amount of the power supply current is diverted through these resistors, which is measured by a Pearson current probe. From this current and known resistance, the voltage is computed by Ohm's law, $V = IR$.

Voltage measurements are taken between the inner and outer electrodes (compression voltage V_C) and the inner and middle electrodes (acceleration voltage V_A). The middle

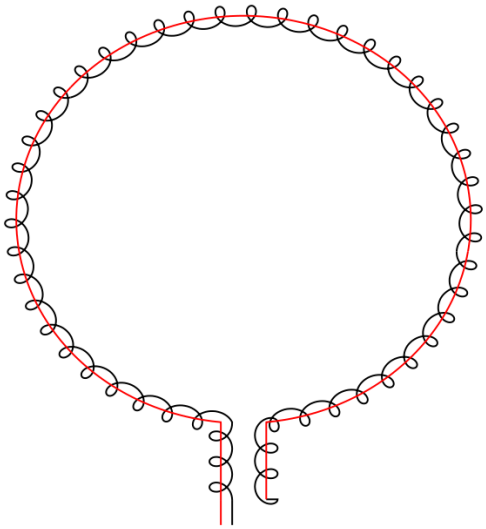

Figure 2.3: Simple diagram of a Rogowski coil. The coil windings are shown in black and the return wire is shown in red. The return wire is run through the center of the coil to cancel any flux picked up perpendicular to the plane of the winding [16].

electrode voltage is inferred by subtracting the acceleration voltage from the compression voltage,

$$V_M = V_C - V_A \tag{2.3}$$

2.2.2 Magnetic Field Probes

Several arrays of magnetic field probes are embedded in the middle and outer electrodes of the ZaP-HD machine. These probes measure the magnetic field topography in the assembly and accelerator regions and are a primary diagnostic in ascertaining the structure and stability properties of the pinch. The probes consist of ten windings of 32-gauge magnet wire wrapped around a Kel-F form. The form is bonded to a boron nitride shield with Torr-Seal, which serves to protect the windings from contact with the plasma. Each probe is inserted into a hole machined in the electrodes and affixed with vented, silver-plated screws. Probes are actively integrated before being digitized. The accelerator probes are digitized at 20 MHz by 8-bit T2008 digitizers. The assembly probes are digitized at 40 MHz by Joerger TR1612 12-bit digitizers.

A total of 71 probes are installed in the machine, 56 in the assembly region and 15 in the acceleration region. The acceleration region probes are arranged into a linear array with an inter-probe spacing of 5 cm spanning 5 cm to 75 cm upstream of the cathode nosecone. The assembly region has four eight-probe azimuthal arrays and six four-probe azimuthal arrays, shown in Fig. 2.4.

The time-changing magnetic field produces a voltage across the ends of the magnetic probe leads according to Faraday's Law, $V = -\frac{d\Phi}{dt} = -NA\frac{dB}{dt}$. The azimuthal probe arrays in the assembly region are used to determine the stability characteristics of the pinch. A Fourier decomposition of the raw azimuthal field data yields the axial current and current centroid at the location of the probe array. The discrete form of the Fourier decomposition is

$$B_\theta(\theta_i) = \sum_{j=0,m} a_j \cos(j\theta_i) + \sum_{j=1,m} b_j \sin(j\theta_i) \tag{2.4}$$

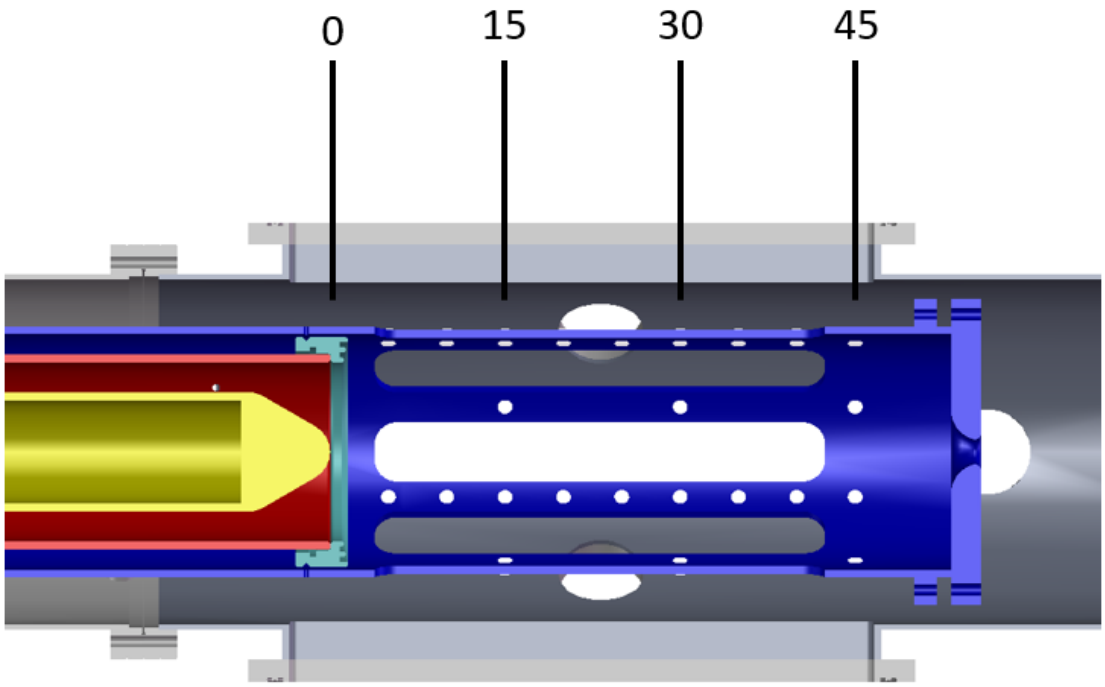

Figure 2.4: Locations of the probe arrays in the assembly region. The eight-probe arrays are located at the indicated axial values, with two sets of four-probe arrays between each eight-probe array.

where θ_i is the azimuthal location of the probe. The azimuthal mode amplitudes are found by solving for the coefficients a_j and b_j in the Fourier series

$$m_j = \sqrt{a_j^2 + b_j^2} \tag{2.5}$$

$$\phi_j = \tan^{-1}\left(\frac{b_j}{a_j}\right). \tag{2.6}$$

The measured fields, unknown coefficients, and sine and cosine terms are arranged into three separate arrays, **B**, **C**, and **A**. Taking the pseudo-inverse of the matrix **A** yields the coefficients a_j and b_j [16]

$$\mathbf{C} = \left(\mathbf{A}^T\mathbf{A}\right)^{-1}\mathbf{A}^T\mathbf{B} \tag{2.7}$$

The mode amplitudes m_j indicate the contributions of different modal shapes to the measured current distribution. To resolve a mode m_j requires a probe array containing $2m_j + 1$ probes. The ZaP-HD assembly region probe arrays with eight probes are equipped to measure up to $m = 3$. Determination of the Z-pinch stability relies heavily on measuring the m_0 and m_1 modes, which respectively measure the mean amplitude of the magnetic field, and the radial displacement of current from the geometric center of the array. The m_1 displacement is particularly important, as it is the primary metric used to assess pinch quiescence. The normalized m_1 is related to the displacement of the current by

$$\frac{m_1}{m_0} = 2\frac{\Delta r}{r_{wall}} \tag{2.8}$$

assuming axially uniform current perturbations and that $\Delta r/r_{wall} < 0.5$ [16]. If the value of m_1/m_0 is less than 0.2, the current centroid is within a centimeter of the axis of the electrode.

The Z pinch in ZaP-HD is defined to be stable if for an extended time both $m_1/m_0 < 0.2$ and $m_0 > 0$. This criteria stipulates there must be significant current flowing along the machine access for a quiescent pinch to be present. Some sample magnetic field probe data are plotted in Figs. 2.5 and 2.6. Figure 2.5 is a plot of the mean m_1 magnetic mode data in black and its standard deviation in gray. A level of 0.2 is indicated by the blue horizontal

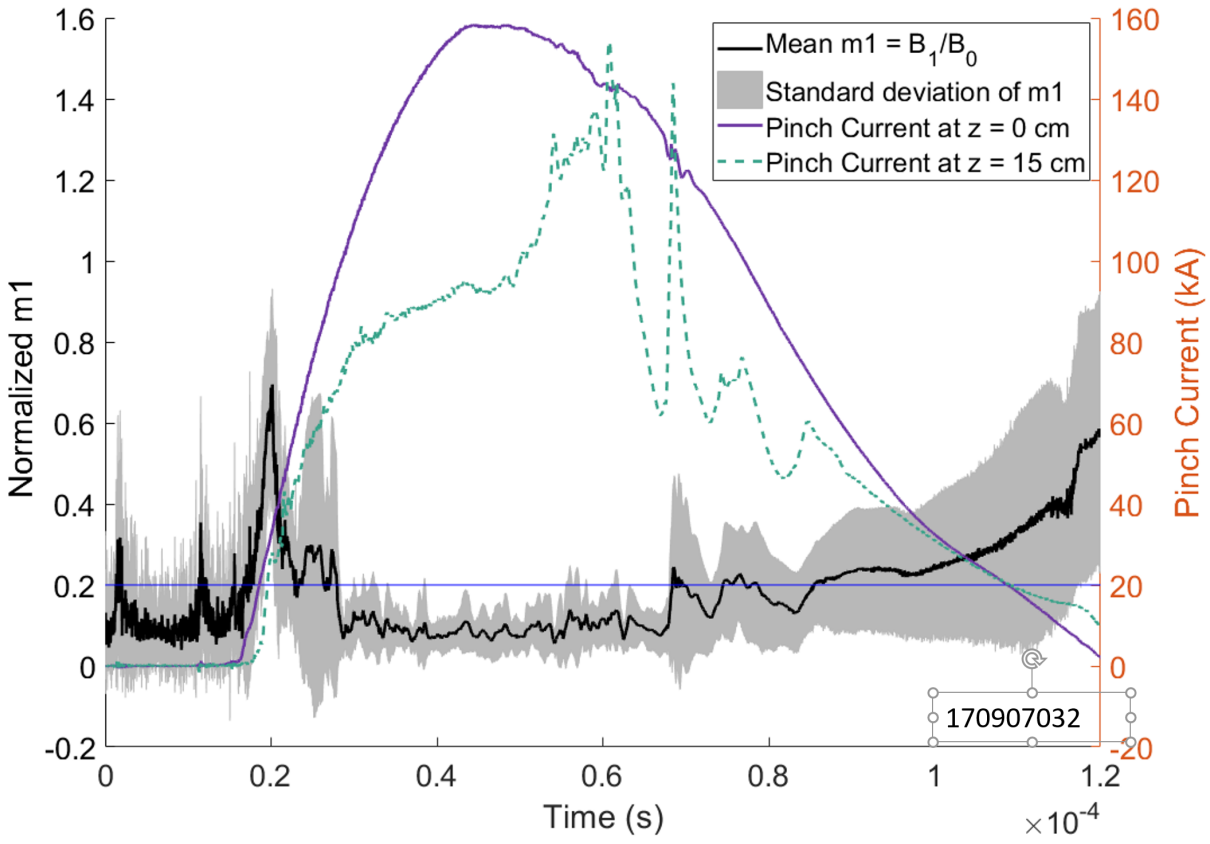

Figure 2.5: Normalized m = 1 magnetic mode data and pinch current. The axial mean of m_1/m_0 is shown in black, with the standard deviation window around it in gray. A horizontal line indicates where the mode data are below 0.2, the criteria for a quiescent pinch. The pinch current at $z = 0$ and $z = 15$ cm from the nosecone is shown in solid purple and dotted green respectively. This pulse has a quiescent period from t = 30 μs to t = 70 μs.

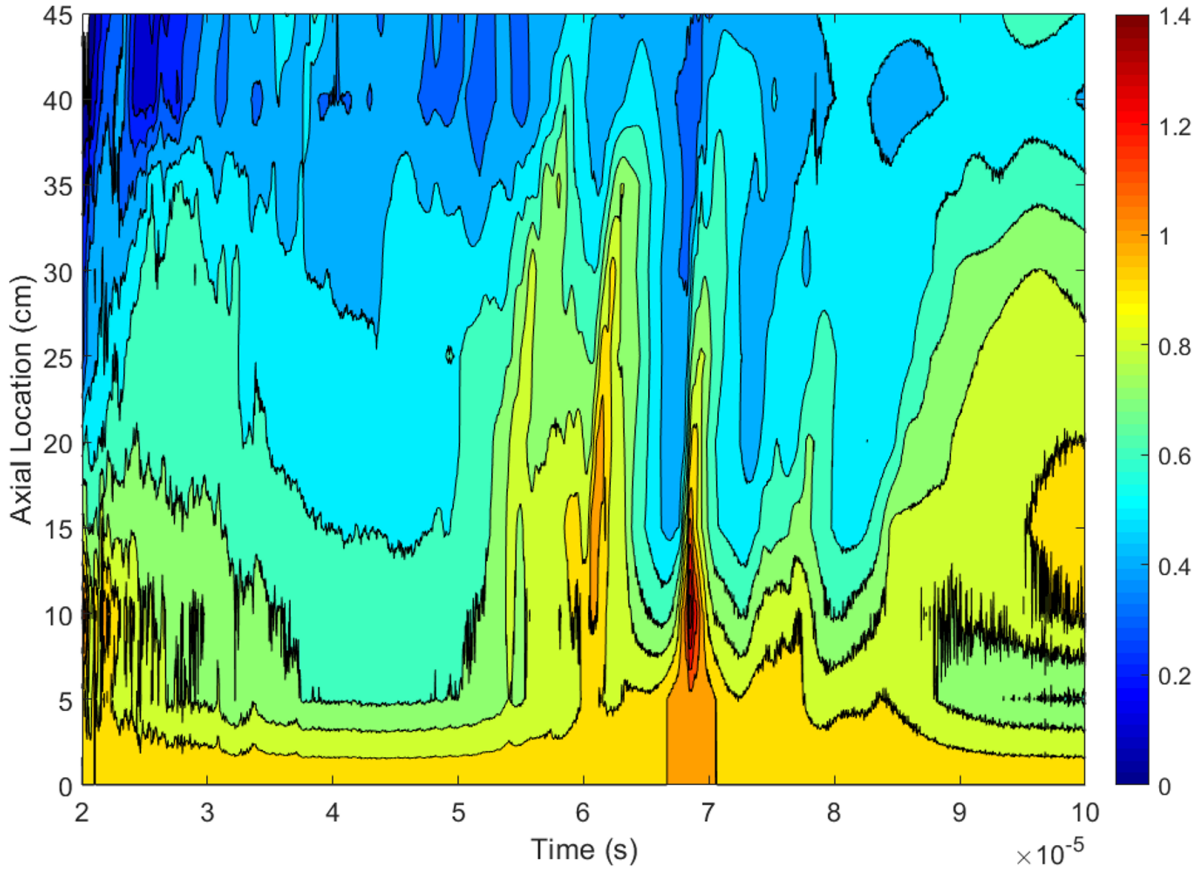

Figure 2.6: Normalized azimuthal magnetic field in the assembly region. The field strength at each axial location has been normalized by the value of the magnetic field at the nosecone ($z = 0$). During the quiescent period, there are few fluctuations in the magnetic field. The field strength decreases along the pinch due to radial currents in the assembly region. Around 70 μs the field spikes near $z = 10$ cm. This coincides with the end of the quiescent period shown in Fig. 2.5.

line. The solid purple and dotted green lines show the current in the pinch at $z = 0$ and $z = 15$ cm from the nosecone. This plasma pulse shows an extended quiescent period of approximately 40 μs, beginning around 30 μs after the pulse trigger time. Figure 2.6 is a contour plot of the normalized magnetic field strength in the assembly region over time. The field strength is normalized to the measured field value at the nosecone. The magnitude of the field decreases along the pinch axis due to the presence of radial currents. Around 70 μs, a disruption occurs, coinciding with a spike in the current at $z = 15$ (shown in dashed green in Fig. 2.5) and the end of the quiescent period.

2.2.3 Spectroscopy

Theory

Ion Doppler spectroscopy (IDS) is a versatile and common technique used to measure plasma parameters from radiating plasma ions. IDS is a convenient passive diagnostic that does not require a physical probe to be inserted into the plasma. The versatility of this diagnostic is evident from the wide variety of plasma experiments that field spectrometers to measure plasma density, temperature, and confinement times, from long-lived, lower-temperature tokamaks such as the National Spherical Torus Experiment to the nanosecond-pulses and extreme temperatures of the National Ignition Facility [39, 29, 26, 13].

Spectroscopy can infer plasma parameters by observing line radiation. Line radiation is the result of an excited bound electron falling from a high energy state to a lower energy state. Bound electrons are excited in the plasma through collisions with free electrons of sufficient energy. When the excited bound electron decays to a lower energy level, the electron emits a photon with energy proportional to the energy lost by the bound electron

$$\Delta E = h\nu \tag{2.9}$$

where ΔE is the difference in energy between the two levels, h is Planck's constant, and ν is the radiation frequency. A diagram of this process is shown in Fig. 2.7. The wavelength

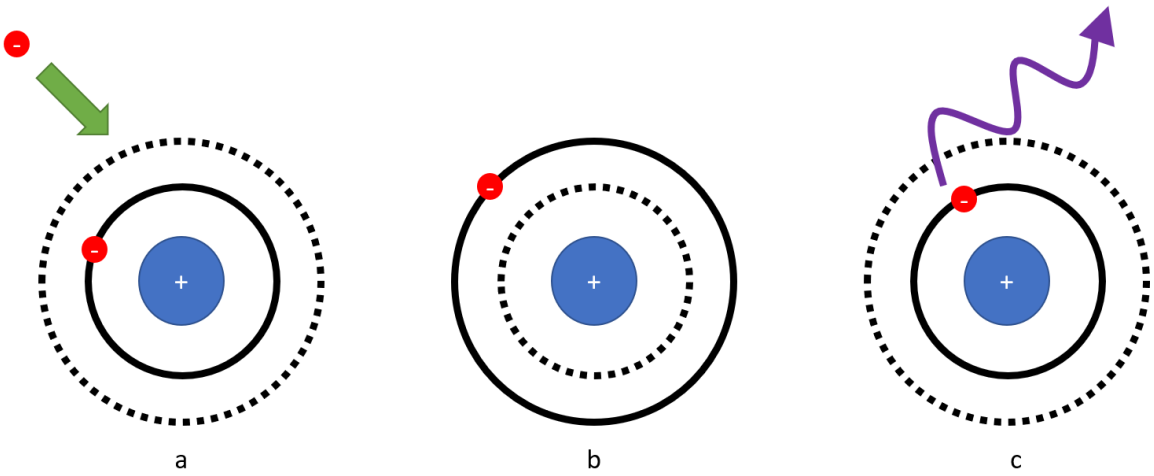

Figure 2.7: Line radiation caused by excitation of a bound electron. On the left, a free electron impacts an atom with a bound electron. In the center, the bound electron is excited by the impact to a higher energy level. On the right, the bound electron decays back to the ground state and emits a photon in the process with energy proportional to the energy lost by the bound electron.

of the radiated photon is well known for each element due to the discrete nature of electron energy levels.

It is possible that the electron impact will impart enough energy to ionize the atom. The working gas in ZaP-HD is hydrogen, which only has one electron. Therefore, no line radiation will be emitted by the bulk plasma. Instead, impurity line radiation is used to compute plasma properties. The most commonly used impurities in ZaP-HD spectroscopy are carbon and oxygen. The presence of different ionization states of these impurities can indicate the energy density of the plasma, as each electron requires increasing amounts of energy to remove.

Plasma temperature is determined by measuring the Doppler broadening of line radiation [38, 30]. Doppler broadening is an effect caused by the random motion of particles in the

plasma. The velocity of each particle imparts a Doppler shift to the observed radiation emitted from that particle. The cumulative effect of these shifts is a broadening of the observed line radiation. The random motion of the particles is related to the temperature through the Maxwell distribution

$$P_v(v) = \sqrt{\frac{m}{2\pi kT}} \exp\left(-\frac{mv^2}{2kT}\right) \tag{2.10}$$

where m is the particle mass, T is the temperature, and k is the Boltzmann constant. The velocity distribution can be related to the frequency distribution by

$$P_f(f)df = P_v(v_f)\frac{dv}{df}df \tag{2.11}$$

where $v_f = c\left(\frac{f}{f_0} - 1\right)$, the rest frequency is f_0 and f is the shifted frequency. Substituting this in, the distributions are related by

$$P(f)df = \frac{c}{f_0} P\left(c\left(\frac{f}{f_0} - 1\right)\right) df \tag{2.12}$$

and therefore the Maxwell distribution can be written in terms of the frequency shift

$$P_f(f)df = \left(\frac{c}{f}\right) df = \left(\frac{c}{f_0}\right) \sqrt{\frac{m}{2\pi kT}} \exp\left(-\frac{m\left[c\left(\frac{f}{f_0} - 1\right)\right]^2}{2kT}\right) df \tag{2.13}$$

which simplifies to

$$P_f(f)df = \sqrt{\frac{mc^2}{2\pi kT f_0^2}} \exp\left(-\frac{mc^2(f - f_0)^2}{2kT f_0^2}\right) df. \tag{2.14}$$

This is a Gaussian profile. By fitting a Gaussian function to the line radiation profile, the temperature can be extracted from the full width at half maximum

$$\Delta f_{FWHM} = \sqrt{\frac{8kT \ln 2}{mc^2}} f_0. \tag{2.15}$$

It is often convenient to express this in terms of wavelength, as intensity measurements on ZaP-HD are made with respect to wavelength, rather than frequency,

$$\Delta\lambda_{fwhm} = 2\sqrt{2 \ln 2 \frac{kT}{mc^2}} \lambda_0. \tag{2.16}$$

Density can be extracted from a spectroscopic measurement by examining the Stark broadening of the line radiation. Stark broadening is a pressure effect that changes the shape of the line emission. Particle collisions in the plasma can interrupt the emission process, changing the characteristic emission time and increasing the uncertainty in the energy emitted. The broadening is described by the Lorentz distribution function,

$$P(f; f_0, \gamma) = \frac{1}{\pi\gamma}\left[\frac{\gamma^2}{(f - f_0)^2 + \gamma^2}\right] \tag{2.17}$$

where γ scale parameter specifying the half width at half maximum.

Both Doppler broadening and Stark broadening will be present at the same time in a hot, dense plasma. The result is that the spectral shape will be the convolution of a Gaussian and a Lorentzian curve, which is called a Voigt profile [59]. Sensitivity studies of ZaP-HD spectra have shown that Stark broadening accounts for less than 1% of the line broadening at the measured temperatures and densities. Lorentzian broadening is therefore generally neglected in the analysis of ZaP-HD data.

Measuring impurity line radiation requires a spectrometer to separate the light by wavelength. This is accomplished with a diffraction grating. A diffraction grating uses closely spaced slits or grooves to disperse light. The groove spacing dictates the dispersion of the diffracted light and therefore the resolution of the spectrometer. Light diffracted off the grating is composed of the sum of interfering wave components emanating from each groove. The grating is turned at an angle to the detector such that the diffracted light has a maximum at the wavelength of interest. The relationship between the wavelength of light and the angle where the maxima occur is

$$d(\sin\theta_i - \sin\theta_m) = m\lambda \tag{2.18}$$

where d is the center-to-center distance of the grooves, λ is the wavelength, θ_m is the angle between the maximum of the diffracted ray and the grating's normal vector, m is the integer propagation mode of interest, and θ_i is an arbitrary angle of incidence of the wave. A diagram of the geometry is shown in 2.8.

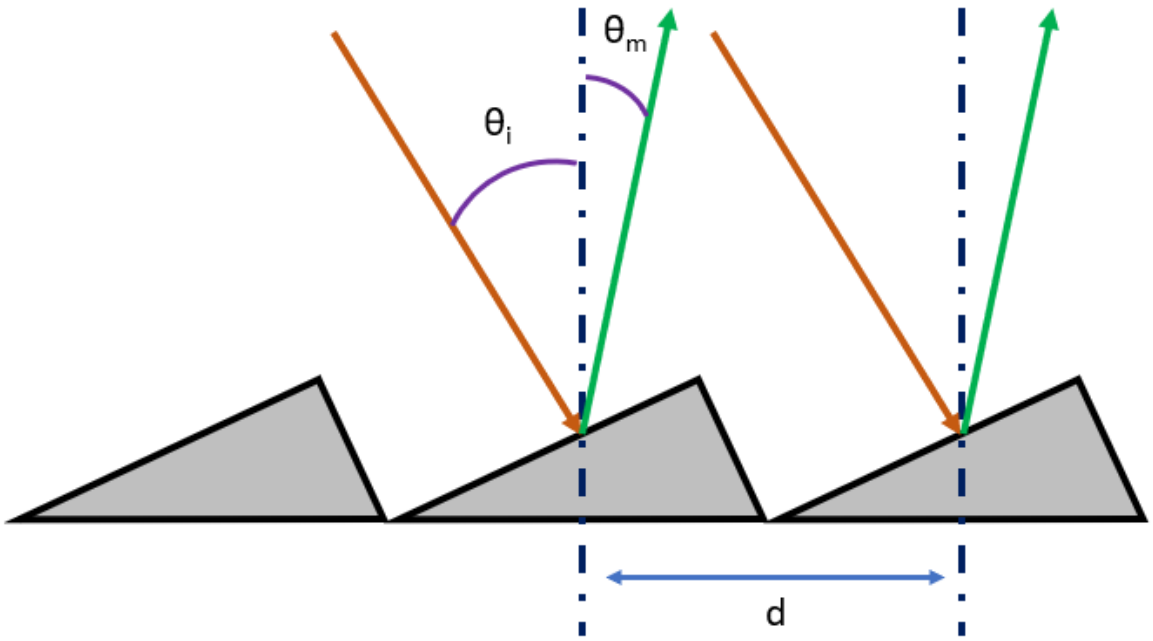

Figure 2.8: A diagram depicting the geometry of a diffraction grating. Light is incident on the grating groove at an angle θ_i. The grating is turned so that the diffracted light with the wavelength of interest interferes constructively on the spectrometer detector.

Implementation

There are two spectrometers fielded on the ZaP-HD machine. An 0.5 m Czerny-Turner Acton SpectraPro 500i is attached to an intensified charge-coupled device (ICCD) Roper Scientific Pi-MAX camera. The Acton has three different diffraction gratings to obtain spectra of varying resolution. A 150 groove per millimeter (g/mm) grating produces a spectrum spanning approximately 100 nm and is useful for line identification. A 2400 g/mm grating and a 3600 g/mm grating resolve spectra spanning only a few nanometers across the entire detector in the visible and ultraviolet ranges respectively. The ICCD records one spectrum per pulse with an exposure time of between 100 and 500 ns. The other spectrometer is an 0.5 m Jarrell Ash model 82-020 spectrometer coupled to a Santa Barbara Research Group ST-6 CCD camera and a photo-multiplier tube (PMT). This instrument gives the time-resolved intensity of light from a single impurity line as well as a single spectrum which is integrated over the entire pulse. A 50/50 beam splitter divides the light to record both measurements simultaneously.

The ICCD spectrometer views the plasma through two telescopes, one mounted perpendicular to the plasma flow and one at an angle of 45 degrees to the plasma flow [17, 19]. Both telescopes collect light through the rectangular windows in the machine assembly region. The telecentric telescopes are connected to fiber bundles which route light back to the spectrometer. Two fiber bundles are used: one with 20 parallel chords, the "wide" bundle, that can be used at one axial location, and one bundle with two sets of 10 parallel chords, the "split" bundle, that may be used at two separate axial locations. The split bundle is also used to simultaneously collect velocity and temperature data from the same axial location. The wide bundle has an inter-fiber spacing of 1.2 mm and images 24 mm across the plasma diameter. The split bundle has the same total spread but with an inter-fiber spacing of 2.4 mm.

Both telescopes record Doppler broadening of the line radiation. The oblique telescope measures the Doppler shift of impurity lines to detect bulk plasma flows. Typically, the

bright carbon-III line at 229.687 nm is used to measure velocities because it is detectable throughout the duration of the pulse. The radial telescope is insensitive to Doppler shifts from the bulk plasma flows, and therefore only measures the Doppler broadening (and Stark broadening if the temperatures are low enough). Higher ion temperatures in ZaP-HD are typically measured with the carbon-V lines at 227.1 nm and 227.7 nm. At any point in the plasma, multiple ionization states of impurity ions can be present. For instance, carbon-III will be visible when carbon-V is present, but the carbon-III will appear at a lower temperature since collisions with hot electrons will cause the carbon-III to ionize.

2.2.4 Digital Holographic Interferometry

Digital holographic interferometry (DHI) measures plasma electron density by recording the phase shift of a laser beam that has passed through the plasma. DHI produces one measurement per plasma pulse of the two-dimensional, line-integrated electron density. This high-resolution measurement of line-integrated density can be Abel-inverted to produce the electron number density. Applying the Bennett relations to the 2D electron density profile yields the electron temperature and magnetic field.

Theory

When an electromagnetic wave passes through a plasma, the phase velocity shifts as a result of the plasma refractive index. The shift in phase is measured with holography and used to determine the line-integrated electron density,

$$\phi_{n_e} = -\frac{e^2}{4\pi c^2 m_e \epsilon_0} \lambda N_e \tag{2.19}$$

where

$$N_e = \int n_e dl \tag{2.20}$$

To measure this phase shift, a laser beam is passed through the plasma and the interference of the resulting wavefront with the original wavefront is recorded. As light-sensitive detectors

can only measure light intensity, not phase, the deformed wavefront must be reconstructed to extract the amplitude and phase.

The wavefront is reconstructed using the Huygens-Fresnel principle, which states that every point on a wavefront is a source for mutually interfering spherical wavelets. Mathematically, the Fresnel approximation allows us to calculate propagation of the scene beam from the (x, y) detector plane to the (ξ, η) reconstruction plane a distance d away as

$$\Gamma(\xi,\eta) = \frac{ia}{\lambda d}\exp\left[-i\frac{\pi}{\lambda d}\left(\xi^2+\eta^2\right)\right]\times\int_{-\infty}^{\infty}\int_{-\infty}^{\infty} t(x,y)\exp\left[-i\frac{\pi}{\lambda d}(x^2+y^2)\right]\times\exp\left[i\frac{2\pi}{\lambda d}\left(x\xi+y\eta\right)\right]dxdy \tag{2.21}$$

Here $\Gamma(\xi, \eta)$ is the complex amplitude of the diffracted wave, the first term is the complex amplitude of the source, $t(x, y)$ is the transmittance of the recorded interference pattern, which is convolved with the complex amplitude of the secondary wavelets and an inclination factor. This equation yields the complex amplitude for a continuous wavefront [47]. However, when recording a hologram with a digital detector, it is discretized into an array of $N \times N$ points with spacing Δx and Δy. We replace the coordinates ξ and η with $m\Delta\xi$ and $n\Delta\eta$ where m and n are integers and $\Delta\eta$ and $\Delta\xi$ are pixel sizes in the reconstructed image. Using the relationships between the spatial coordinates [25]

$$\Delta\xi = \frac{\lambda d}{N\Delta x},\ \Delta\eta = \frac{\lambda d}{N\Delta y} \tag{2.22}$$

we can write a discretized representation of Eqn.2.21

$$\Gamma(m,n) = \exp\left[-\frac{i\pi}{\lambda d}\left(\frac{m^2}{N^2\Delta x^2}+\frac{n^2}{N^2\Delta y^2}\right)\right]\times\sum_{k=0}^{N-1}\sum_{l=0}^{N-1} t(k,l)\exp\left[-i\frac{\pi}{\lambda d}(k^2\Delta x^2+l^2\Delta y^2)\right]... \times\exp\left[i2\pi\left(\frac{km}{N}+\frac{ln}{N}\right)\right]$$

Numerically, this is a representation of the Fresnel approximation in terms of an inverse discrete Fourier transform.

The reconstructed wave field $\Gamma(m, n)$ is a complex function and can be used to calculate both intensity and phase. The intensity is given by

$$I(m,n) = |\Gamma(m,n)|^2 \tag{2.23}$$

and the phase from

$$\phi(m,n) = \arctan \frac{\Im\left[\Gamma(m,n)\right]}{\Re\left[\Gamma(m,n)\right]} \tag{2.24}$$

Implementation

Extracting the plasma density with DHI begins by creating a hologram. To image the plasma, a laser is expanded and split into two beams, a scene beam and a reference beam, shown in Fig. 2.9. The scene beam passes through the Z pinch. The reference beam is diverted around the plasma so that the original wavefront is preserved. The two beams are incident on the same detector with a slight misalignment angle between them. The misalignment angle creates an interference pattern which is recorded on the detector. The angle between the beams must be small enough that the detector can resolve the fringes. The fringe spacing δ decreases as misalignment angle θ increases by

$$\delta = \frac{\lambda}{\sin\theta} \tag{2.25}$$

where λ is the wavelength of the laser light.

The recorded hologram contains the amplitude and phase of the scene beam. The hologram is reconstructed numerically through a fast Fourier transform in Matlab, following the mathematical methods described in the theory section. The reconstruction algorithms were developed by Michael Ross and have been described in detail in his dissertation [44].

The phase that is extracted using Eqn. 2.24 will have a value between $-\pi$ and π. A phase shift greater than 2π will result in a discontinuous fringe jump. The phase map can be recreated by unwrapping the fringe jumps. The unwrapping algorithm examines the derivative of the phase and adds a value of $\pm 2\pi$ when the derivative exceeds a critical value.

Once the phase is unwrapped and the line-integrated density is found using Eqn. 2.19, the electron number density is found with an Abel inversion. The conversion between measured N_e and n_e is expressed as

$$N_e(y) = 2\int_y^\infty \frac{n_e(r) r dr}{\sqrt{r^2 - y^2}} \tag{2.26}$$

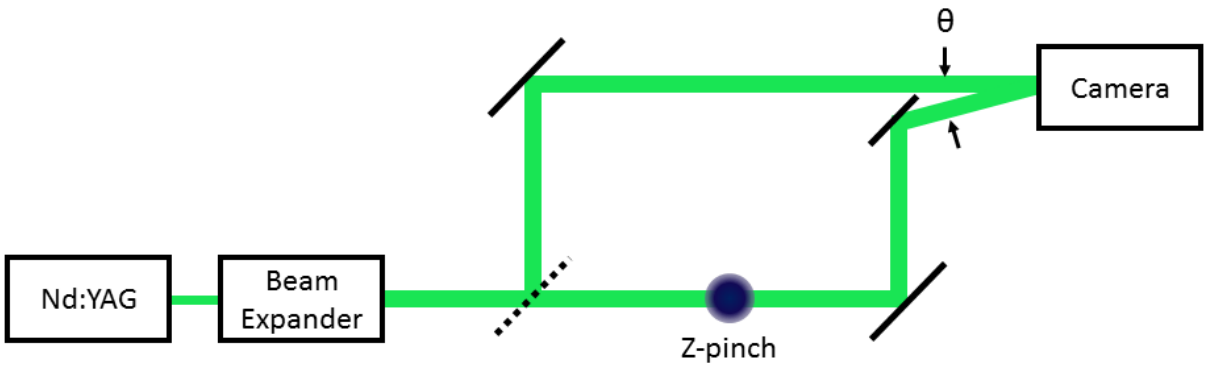

Figure 2.9: A cartoon of the DHI setup. The laser beam passes through a beam expander to create the largest possible hologram and then through a 50/50 beam splitter. One beam (the scene beam) is passed through the plasma. The other (the reference beam) is diverted around the plasma to preserve the original wavefront of the laser. The beams are recombined on the camera sensor. A slight misalignment angle is included to produce reference fringes so that the phase shift of the scene beam may be determined.

where y is the impact parameter and r is the radius. This transform requires that the density n_e be axisymmetric, that is n_e is not a function of θ. In practice, the analysis code discretizes this transform by splitting the plasma into concentric nested shells of uniform density. This is manifested as

$$\vec{N}_e = 2\Delta r \mathbf{A} \vec{n}_e \tag{2.27}$$

where the matrix $\mathbf{A}$ indicates the path length through each shell. A visual representation of this process is shown in Fig. 2.10. The electron density n_e is determined simply by inverting the discretization matrix

$$\vec{n}_e = \frac{1}{2\Delta r} \mathbf{A}^{-1} \vec{N}_e \tag{2.28}$$

2.2.5 Fast Framing Photography

An ultra-fast framing camera has the unique benefit of providing immediate qualitative data on plasma behavior following a pulse. The Kirana-05M high speed camera has the capability of capturing 180 frames at up to 5 million frames per second (FPS). The 10-bit monochrome sensor has a resolution of 924×786 pixels with a 30 μm pixel size. The sensor can record light in the visible range and can view ultraviolet emission with an attachable phosphor intensifier unit.

In general, visible light emission in the plasma either comes from bremsstrahlung radiation or from hot gaseous hydrogen. Bremsstrahlung radiation, or braking radiation, is light emitted as a result of a free electron in the plasma experiencing Coulomb collisions with ions. The collision changes the trajectory and velocity of electron, and this change in energy results in the electron emitting a photon. Bremsstrahlung radiation is dependent upon the plasma temperature and density [23]

$$P_{Brem} = 1.69 \times 10^{-38} Z_{eff}^2 n_e^2 T_e^{1/2} \tag{2.29}$$

where Z_{eff} is the effective charge state. Hot gaseous hydrogen emits in the visible spectrum at 656.28 nm. Line radiation from hydrogen tends to occur in cooler regions of the plasma

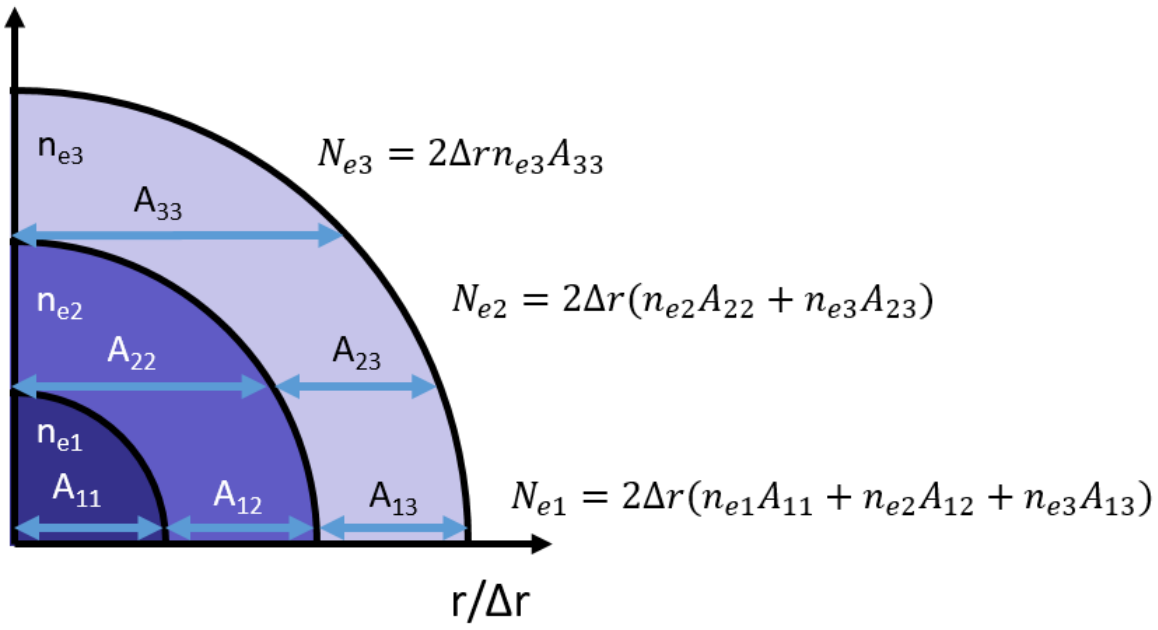

Figure 2.10: A simple diagram of an Abel inversion. Here a cylinder is broken up into concentric shells, each with a uniform density. In this case, the line-integrated density is expressed as a product of each uniform density and its corresponding chord length dictated by the matrix **A**.

and bremsstrahlung radiation from hotter regions of the plasma. To filter out light emitted by the hydrogen, a band pass filter can be employed in front of the Kirana camera lens. The filter used for ZaP-HD experiments is comprised of Wratten #18 and #12 filters to pass only light in the 500-600 nm range. The images in Fig. 2.11 show the formation and compression of a pinch with the bremsstrahlung filter attached.

2.3 Experimental Results from ZaP-HD

Experiments on ZaP-HD have shown that the tri-axial electrode configuration is effective for extending the life and increasing plasma parameters in the sheared flow stabilized Z pinch. Measurements of magnetic modes, ion temperature, and electron density have shown quiescent periods of up to 60 μs, temperatures of 1 keV, and densities of 1×10^{24} m^{-3}. These measured parameters can be compared to the values expected from adiabatic scaling of the Bennett relation.

An expression of the Bennett relation can be found by integrating the two-fluid equilibrium

$$\frac{d}{dr}\left(n_i k_B T_i + n_e k_B T_e\right) = -\frac{B_\theta}{\mu_0 r}\frac{d}{dr}\left(r B_\theta\right) \tag{2.30}$$

over the plasma volume [8] to yield

$$(1+Z) N_i k_B \left\langle T \right\rangle = \frac{\mu_0 I^2}{8\pi}. \tag{2.31}$$

Here I is the axial plasma current, $\langle T \rangle$ is the average temperature, Z is the ionization state, and N_i is the linear ion number density. This assumes that the electron and ion temperatures are equal. The linear ion number density is found from

$$N_i = \int_0^a n_i(r) 2\pi r dr. \tag{2.32}$$

Equation 2.31 is valid for all equilibrium density and magnetic field profiles and can be used to derive a temperature scaling relation [52]

$$\frac{T_2}{T_1} = \left(\frac{I_2}{I_1}\right)^2 \frac{N_1}{N_2}. \tag{2.33}$$

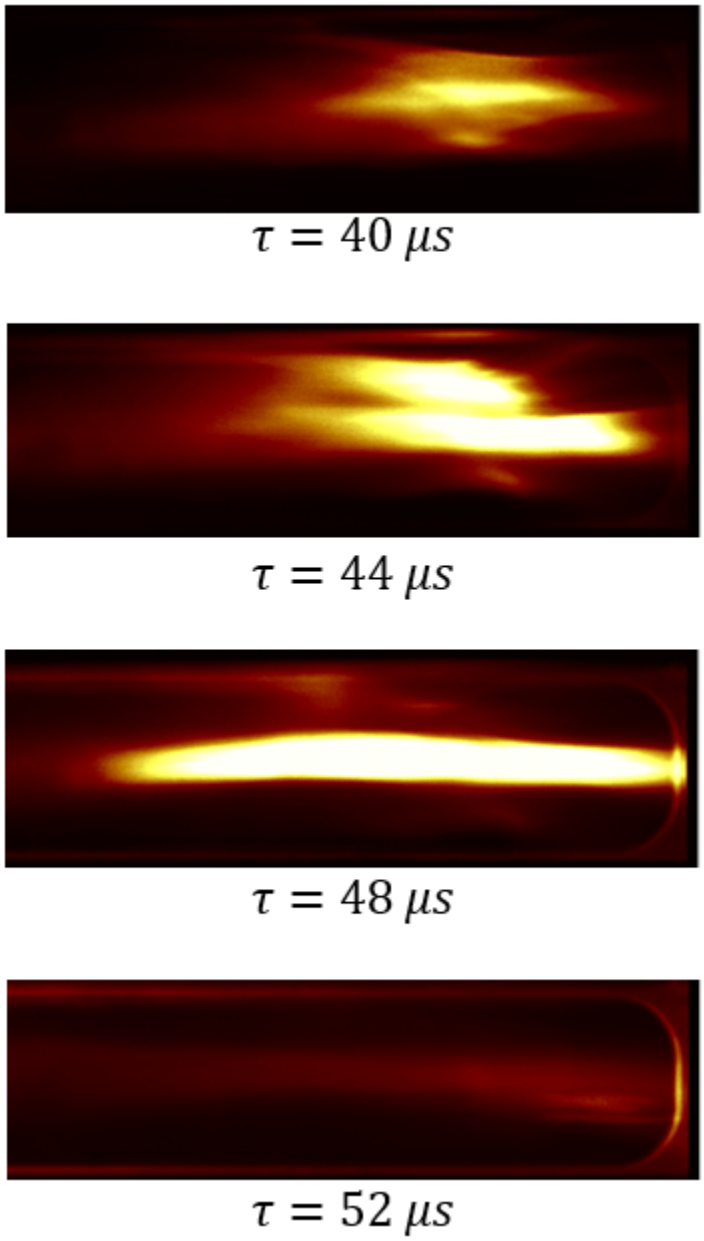

Figure 2.11: Visible light images of the formation and compression of a Z pinch. The view extends from z = 0 cm to z = 25 cm. Over the course of the frames the flowing plasma is compressed into a bright column near the axis of the electrode. The plasma begins to dissipate after approximately 50 μs but is still visible in the bottom frame. The images are false color and have been recorded with a bremsstrahlung filter in front of the lens.

If the pinch compression is assumed to be adiabatic and the plasma density and temperature are assumed to be uniform within a pinch radius such that $n_i = n,\ n_e = Zn$ and $T_i = T_e = T$, expressions for the scaling of pinch radius a and number density are also found

$$\frac{n_2}{n_1} = \left(\frac{I_2}{I_1}\right)^{\frac{2}{\gamma-1}} \left(\frac{N_1}{N_2}\right)^{\frac{1}{\gamma-1}} \tag{2.34}$$

$$\frac{a_2}{a_1} = \left(\frac{I_1}{I_2}\right)^{\frac{1}{\gamma-1}} \left(\frac{N_2}{N_1}\right)^{\frac{\gamma}{2(\gamma-1)}}. \tag{2.35}$$

These relations provide a theoretical basis for scaling the Z pinch to HED conditions.

Sample data from experimentation on ZaP-HD are presented in this section and compared to the values expected from the adiabatic scaling relations. The plasmas were produced with the highest possible bank charge voltages of 9 kV acceleration and 8 kV compression. Sample mode data and current traces are shown in Fig. 2.12. The quiescent period for this pulse begins around 30 μs and ends at approximately 85 μs. The current at $z = 0$ is shown in purple and the current at $z = 15$ in green. The difference between the two indicates significant radial current flowing downstream of the nosecone. Both IDS and DHI were triggered during the quiescent period, IDS at 45 μs and DHI at 85 μs. The measurements were made at a location 10 cm downstream of the nosecone.

Figure 2.13 shows the ion temperature profile calculated from Doppler broadening of carbon impurity ion radiation. Two temperature profiles are shown, one calculated from the 229.687 nm carbon-III line and one from the 227.091 nm carbon-V line. Radiation from carbon-III is seen across every viewing chord and shows a flat background with a temperature of approximately 200 eV. The carbon-V radiation is only seen near the machine axis and indicates a peaked temperature profile with a maximum of 500 eV and a radius of 2 - 3 mm. Both temperatures can be recorded simultaneously due to the chord-integrated nature of the spectrometer measurements.

The presence of the flat background and peaked, centered profile suggests a hot pinch core surrounded by cooler plasma. This is the first measurement that has shown that a stable, hot pinch can exist within a cooler background plasma. The measurement is concurrent with

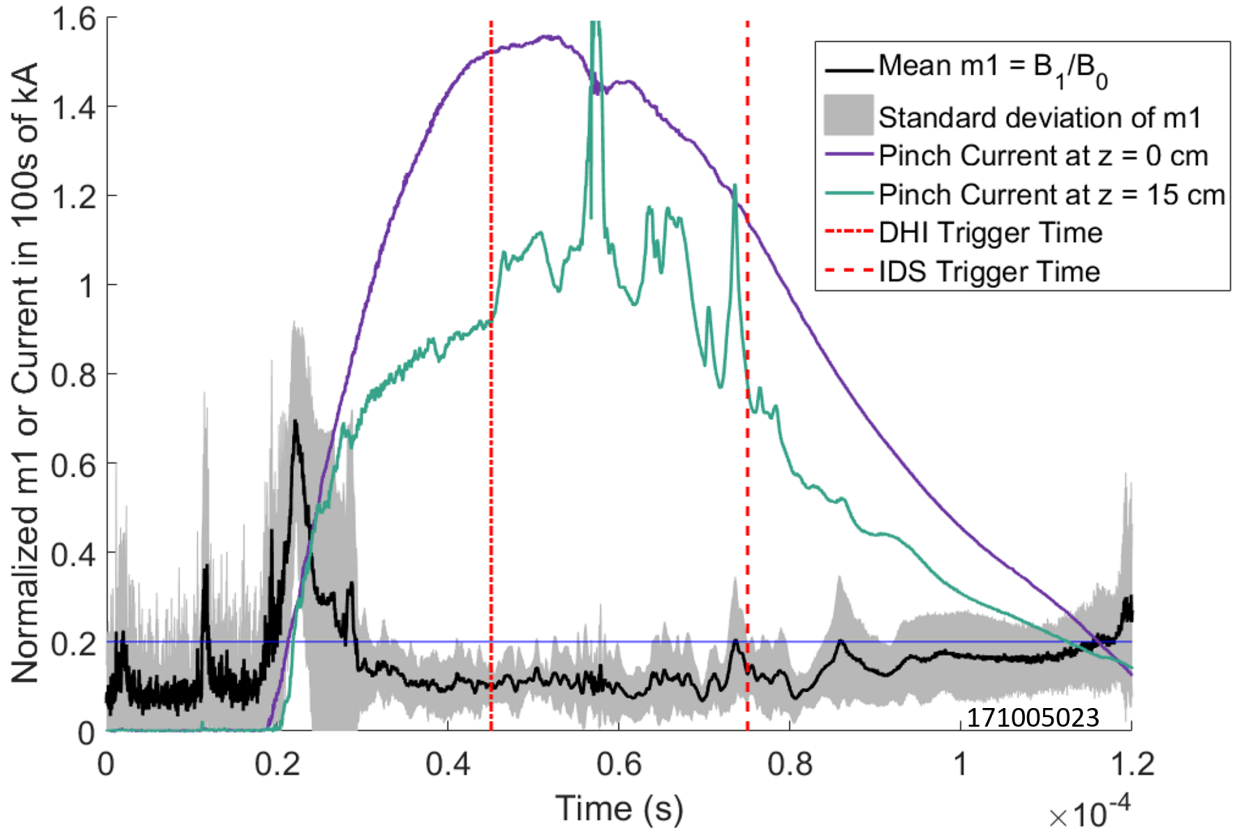

Figure 2.12: Current traces and average axial mode data for the sample holography and ICCD pulses shown in this section. The dotted lines indicate the trigger times for ion Doppler spectroscopy and DHI. Pinch current is shown for $z = 0$ and $z = 15$. Mean axially averaged m_1 and the standard deviation are shown in black and gray

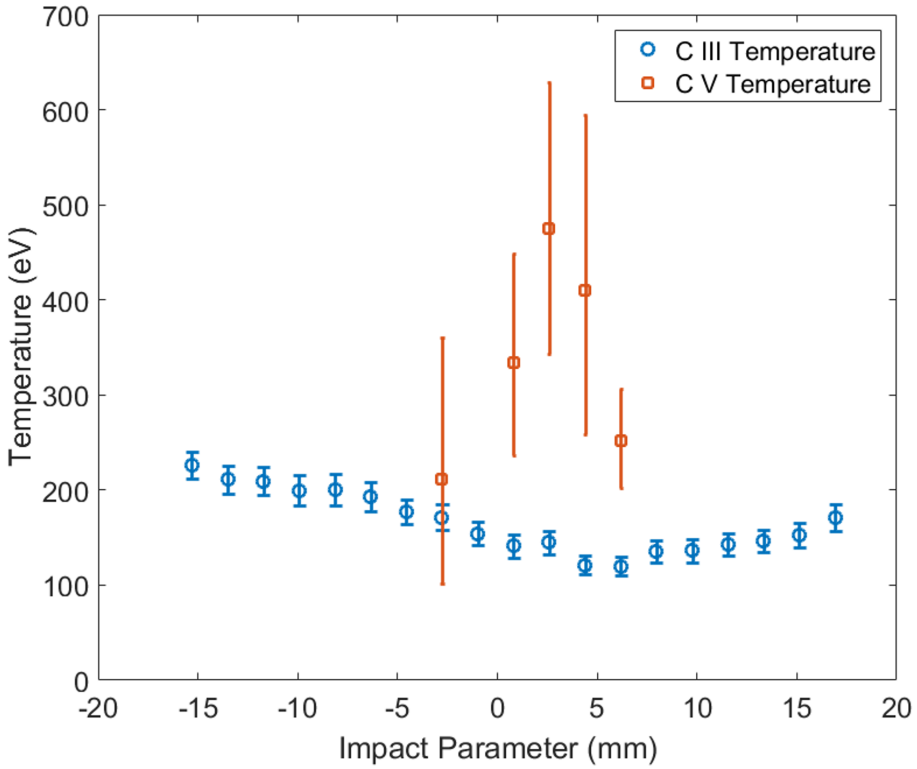

Figure 2.13: Plasma ion temperature computed from carbon-III and carbon-V impurity ion radiation. A lower-temperature carbon-III background is present across all chords, with a peaked carbon-V profile near the machine axis.

a quiescent period indicated by the low value of the standard deviation of the magnetic mode data in Fig. 2.12. The extended quiescent period evidenced by the mode data suggests the pinch remains stable even in the presence of a background plasma.

The profile measured by IDS is corroborated by measurements made with DHI. The Abel-inverted, two-dimensional n_e profile is shown in Fig. 2.14. The calculated centroids of the pinch along the axis are shown with black circles. The electron density peaks at 1.5×10^{24} m^{-3}. Some electron density is also measured outside of the pinch radius, and is most easily seen at positive impact parameter on the upstream side of the image. The radius of the Z pinch is between 1 and 2 mm. One consequence of the presence of electron

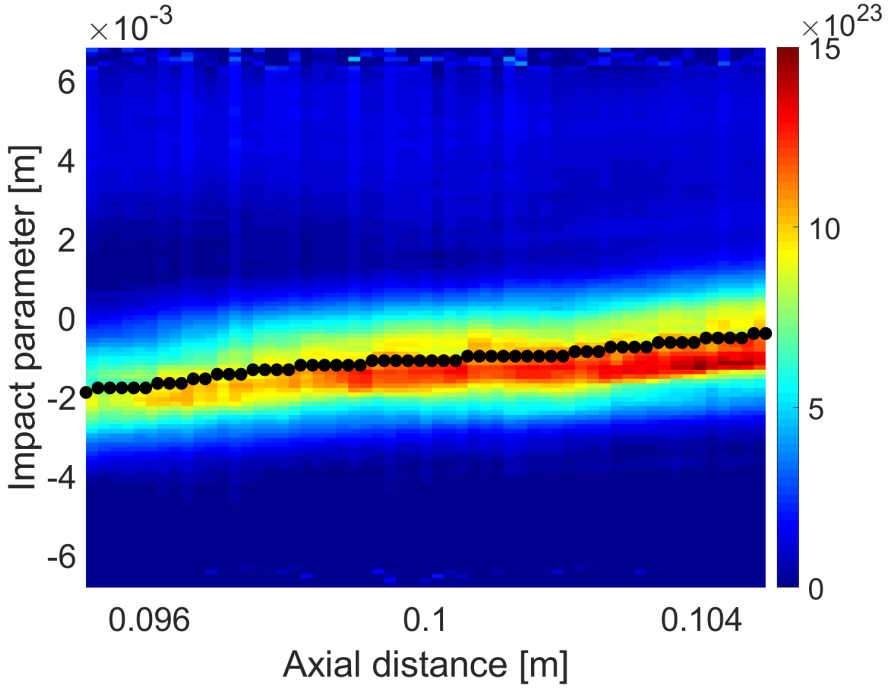

Figure 2.14: Electron number density of a Z pinch measured with DHI. The centroids used to compute the Abel inversion are shown as black dots. Density peaks near 1.5×10^{24} m^{-3}. The pinch radius is between 1 and 2 mm.

density outside of the core Z pinch is that the Abel inversion algorithm calculates a lower peak density for the "upper" density profiles. This is a result of the algorithm attempting to minimize the difference between the top and bottom number density profiles. To ameliorate this, an average profile is calculated at each axial location and shown in Fig. 2.15a. A single radial profile from this average with error bars is shown in Fig. 2.15b.

The measured density profile can be coupled with an equilibrium model [14] to calculate other plasma parameters. This method was developed by Michael Ross and is detailed in Chapter 4 of his dissertation [44]. The analysis assumes a spatially uniform drift velocity

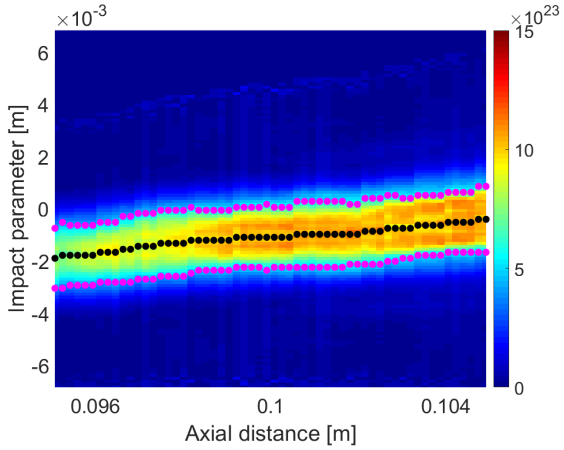

(a) Electron Density (m^{-3}).

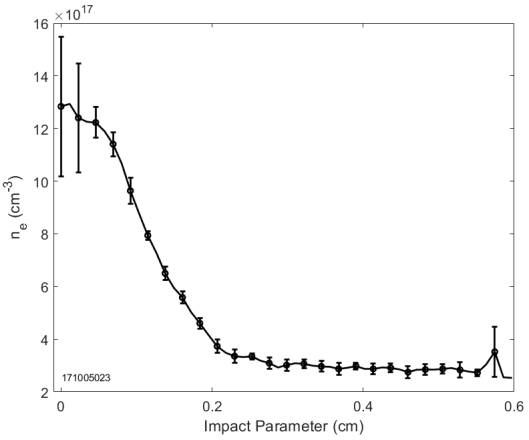

(b) Electron Density (m^{-3}).

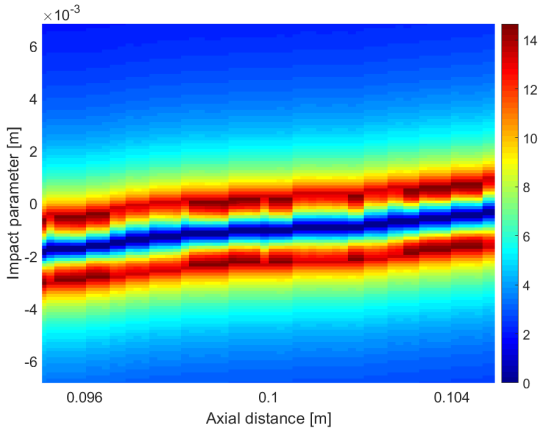

(c) Magnetic Field (T).

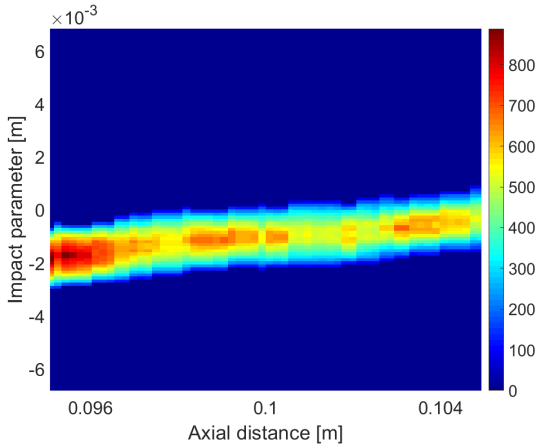

(d) Electron Temperature (eV).

Figure 2.15: Average two-dimensional electron density, an average radial density profile with error bars, two-dimensional magnetic field and electron temperature computed from average electron number density. The two-dimensional profile shown in (a) is computed by taking the average of the top and bottom number density profiles from Fig. 2.14. One such average profile from z = 10 cm is shown in (b). The two-dimensional profile is used to calculate the magnetic field (c) and the electron temperature (d).

such that the current becomes proportional to the charge carrier number density

$$v_d = v_e - v_i \tag{2.36}$$

$$j_z(r) = -v_d e n_e(r) \tag{2.37}$$

The drift velocity is found through a numerical integration of the measured electron density

$$v_d = -\frac{I}{2\pi e \int_0^a n_e(r) r dr} \tag{2.38}$$

where I is the total current computed from measurements made by the magnetic field probe array at $z = 0$ and a is the pinch radius. All current is assumed to flow within the pinch. The magnetic field and temperature can then be expressed in terms of the measured electron density by integrating Ampere's law and force balance respectively to give

$$B_\theta(r) = \begin{cases} \frac{\mu_0 e v_d}{r} \int_0^r n_e(R) R dR, & r < a \\ \frac{\mu_0 I}{2\pi r}, & r \geq a \end{cases} \tag{2.39}$$

$$T_e(r) = \begin{cases} \frac{e v_d}{2 n_e(r) k} \int_a^r n_e(R) B_\theta(R) dR, & r < a \\ 0, & r \geq a. \end{cases} \tag{2.40}$$

Here R is a dummy variable for integration and k is Boltzmann's constant. For this analysis, the radius a is arbitrarily set to the point at which the electron density falls to half the peak value. This value is set to facilitate comparisons to previous data from ZaP and ZaP-HD, and the validity of this assumption is discussed further, along with some alternatives, in [44].

The profiles of magnetic field and temperature calculated using this method are shown in Figs. 2.15c and 2.15d. The magnetic field peaks at 14 T and the peak electron temperature reaches over 800 eV, but generally falls within a range of 500 to 600 eV along the axis. From previous measurements on ZaP-HD, we expect $T_i = T_e$ [28]. Most of the values of T_e calculated from DHI data are within the range measured from the Doppler broadening of carbon-V in Fig. 2.13. In addition, the pinch radius observed from carbon-V broadening is

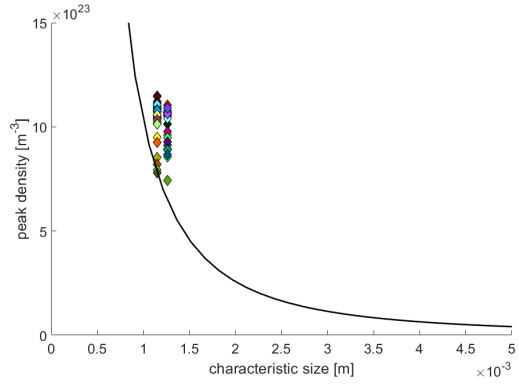

(a)

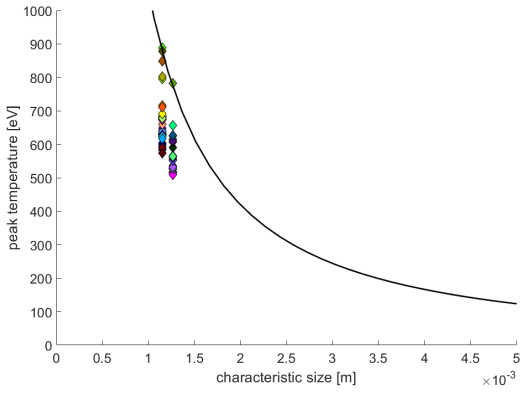

(b)

Figure 2.16: Comparison of computed n_e and T_e to values predicted by adiabatic scaling.

similar to the radius computed in the DHI analysis. It is important to note the measurements were made at the same axial location and for the same pulse settings, but are from different plasma pulses. Overall, the agreement between measurements provides strong indication of high-density, high temperature, stable Z pinches in the ZaP-HD machine.

Some of the results obtained from the holography equilibrium analysis can be compared to the adiabatic scaling relations presented at the beginning of this chapter. Equations 2.34, 2.35, and 2.33 can be manipulated to plot the temperature and peak electron density scaling

with respect to pinch radius,

$$\frac{T_2}{T_1} = \left(\frac{a_2}{a_1}\right)^{-2(\gamma-1)} \left(\frac{N_2}{N_1}\right)^{\gamma-1} \tag{2.41}$$

$$\frac{n_2}{n_1} = \left(\frac{a_2}{a_1}\right)^{-2} \left(\frac{N_2}{N_1}\right) \tag{2.42}$$

These curves have been plotted in Figs. 2.16a and 2.16b. The Z-pinch mass, and therefore the linear density, is assumed to be constant. The pinch conditions at the most upstream point in the hologram are chosen for n_1, T_1, and a_1 and the curves are plotted for a range of a_2, with $\gamma = 5/3$. Peak n_2 and T_e are plotted for each axial location. The pinch captured in Fig. 2.15a has a high degree of radial uniformity along the axis, and values are confined to two characteristic radii due to the limits of the diagnostic resolution. For both parameters, some values lie along the scaling relation, but many lie below the temperature and above the density curve. Both of these regions are characterized by increasing linear density. This may suggest that the assumption of constant linear density is invalid. The discrepancy could also be indicative that the arbitrary choice of plasma radius does not accurately represent the system.

Chapter 3

TIME-RESOLVED ION DOPPLER SPECTROSCOPY

Spectroscopy is a powerful and versatile tool that has produced important results on the ZaP-HD machine. However, the system used on ZaP-HD had a limited ability to resolve plasma properties in time. Over the course of a plasma pulse, the ion temperatures and velocities can vary rapidly as the pinch evolves. A plot of time-resolved velocity is shown in Fig. 3.1. This plot concatenates data taken from many plasma pulses at a single axial location. The trigger time of the ICCD was varied to scan the velocity in time. The plot shows a sustained radial shear of the axial velocity which reverses approximately half way through the quiescent period.

Plots like the one shown in Fig. 3.1 reveal much about the pinch behavior. However, time-resolved data take several weeks to compile for one set of initial conditions and one axial location, since many pulses must be taken at each trigger time. In addition, the pinch behavior can vary between pulses due to factors such as machine temperature or gas puff anomaly. Plots like this can only be produced for settings where data are repeatable. To improve the measurement capabilities of the system, a time-resolved spectrometer is developed. This is accomplished by replacing the ICCD with a fast-framing camera.

3.1 Construction and Implementation on ZaP-HD

To record light from the spectrometer, both the Kirana 05M ultra-fast framing camera and an SIL ultraviolet intensifier module are used in the system. The SIL intensifier uses a phosphor screen that fluoresces when excited by ultraviolet light. The decay time of the phosphor screen limits the frame rate of the diagnostic to 1 MFPS. The system can record 100 spectra during the plasma pulse.

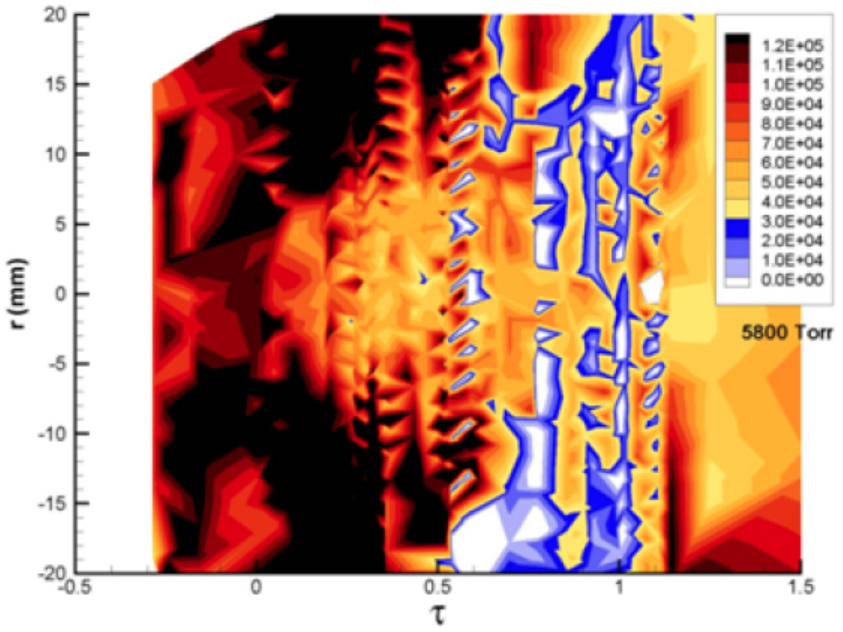

Figure 3.1: Velocity at a single axial location in the pinch over time. These data were collected over the course of several hundred identical pulses and compiled into a time-resolved plot. The x-axis shows the pulse time normalized to the start and length of the quiescent period. The y-axis shows the impact parameter. Approximately half way through the quiescent period, the velocity shear reverses, indicated by the outer chords transitioning from a high velocity to a low one. Plot first appeared in Ref. [50].

The first step of implementation was to marry the detector system to the Acton spectrometer. The spectrometer exit flange requires the detector to be hard mounted with bolts, while the SIL unit has a conventional Nikon F-mount for a camera lens. In addition, most ICCD detectors have coupling optics that move the focal point of the spectrometer exit to the detector plane. The focal point must be precisely at the detector plane to avoid unintentional broadening or aberration of the spectrum. Coupling the Kirana system to the spectrometer required construction of an optical system that moved the focal point to the SIL phosphor screen.

A coupling optics system was designed and constructed to connect the detector to the spectrometer. A simple telescope was constructed from two UV-grade fused silica plano-convex lenses with identical focal lengths. A first iteration of this design had the lenses in a fixed position inside a rigid beam tube. The tube was threaded into a plate on the spectrometer exit flange and attached to an F-mount adapter at the phosphor screen entrance. The rigidity of this design made installation difficult as the height of the detector system had to be adjusted to match the height of the spectrometer. In addition, the focal length of the thick lenses fluctuated with wavelength, and the beam tube design made lens adjustments difficult. A second iteration was developed to improve the alignment process. In the final design, the optics are mounted in small lens tubes and installed on individual translation stages. Alignment is facilitated by optical breadboards and leveling devices. Once aligned, the system is covered in black-out fabric to prevent stray light from being recorded by the camera.

To ensure the lenses are set at the positions necessary to focus the wavelengths of interest, a calibration is performed. Calibration lamps that emit line radiation in the wavelength range of interest are used to test the system alignment. The distance between the lenses and the focal points of the spectrometer and ultraviolet intensifier are adjusted with translation stages until the width of the measured line is minimized. The measurement can then be used as a baseline to eliminate instrument broadening effects when measuring plasma radiation. A proper calibration is paramount to effectively measuring plasma parameters with

this system, as the Kirana has no native software to identify line radiation, unlike the ICCD camera.

Data from time-resolved spectroscopy are collected and processed using methods identical to those described in Section 2.2.3. Both split and wide fiber bundles can be used with the time-resolved spectroscopy set-up. Data are primarily collected with the split fibers to resolve both ion temperature and velocity throughout the pulse. Once data are collected, the video file can be imported into Matlab where each frame is binned by chord and fitted with a Gaussian function. The data are then compiled into contour plots to give the continuous evolution of ion temperature and velocity throughout the pulse.

3.2 Results from Time-Resolved Spectroscopy

The time-resolved spectrometer was fielded on ZaP-HD to measure ion parameters for Z-pinch plasmas made from a mixture of hydrogen and methane gas. The pinches were produced with methane to increase the signal from carbon impurity ion radiation and subsequently the measurement accuracy. The methane concentration ranged between 5 and 50%. This ensured that the ultraviolet intensifier, which is less sensitive than the ICCD, could record radiation throughout the pulse.

Videos are recorded for every pulse and analyzed in Matlab. Kirana data initially saves as an ".SVF" file type and must be converted into an ".AVI" to be processed. A frame from a spectra video is shown in Fig. 3.2. Each bright spot indicates an individual chord. The full resolution of the camera detector is 924 x 768 pixels, but the image is cropped to more clearly show the chord positions. Eleven chords are visible in the image, indicating an emission extent of 16 mm. Solid white lines bound chords collecting light with the oblique telescope to measure velocity, while dotted lines bound chords collecting light with the radial telescope, used to measure temperature. Both telescopes are positioned to collect light from the same axial location in the Z pinch. The raw output of the Kirana is in gray scale, but has been converted to false color here for enhanced contrast.

Once the data are converted to the appropriate file format they can be processed in

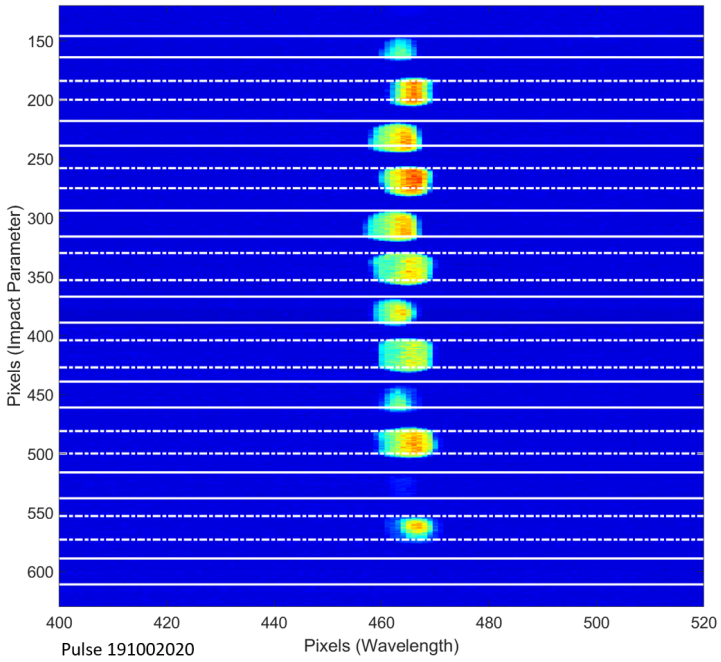

Figure 3.2: One frame of a Kirana spectroscopy video. The image has been cropped to enlarge the signal from individual chords. The full size of the sensor is 924 x 768 pixels. Carbon-III impurity ion radiation is collected with the split fiber bundle, which facilitates simultaneous measurements of ion velocity and temperature. Chords measuring velocity are bounded by solid white lines, while chords measuring temperature are bounded by dotted lines. The image is presented in false color for better contrast. The raw output of the Kirana camera is in gray scale.

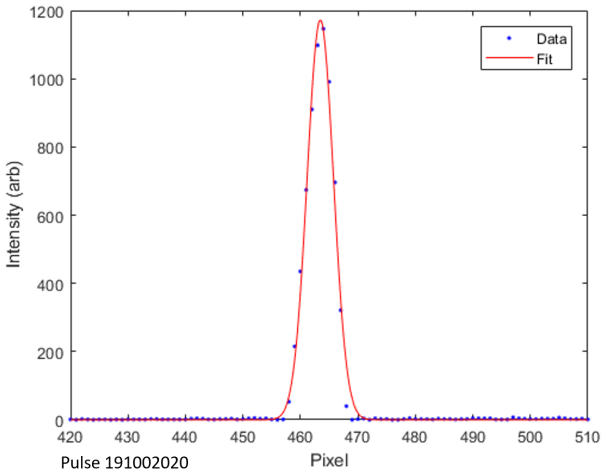

Figure 3.3: A sample fit of raw spectroscopy data. The emission profile, shown in blue, is fitted with a Gaussian function after being corrected for optical aberrations with a baseline subtraction.

Matlab. Each chord is binned and corrected for optical aberrations with a baseline subtraction. The chords are then numerically fit with a Gaussian function. The ion temperature and velocity are extracted using the methods described in Section 2.2.3. Data from each frame are compiled into plots showing the temporal evolution of ion temperature and axial velocity for each pulse.

The time-resolved ion temperature profile for a single plasma pulse is shown in Fig. 3.4a. The abscissa shows the time from the pulse trigger, and the ordinate indicates the impact parameter. Color contours show the temperature in eV. The initial conditions of the plasma were a 10% CH_4 in H_2 gas mixture, with bank charge voltages of 5 kV acceleration and 3 kV compression. Peak measured temperatures of 300 eV occur between 80 and 90 μs. The data indicate the temperature profile is collimated with a peak near the machine axis for a majority of the pulse duration.

The corresponding velocity profile for the pulse is shown in Fig. 3.4b. Here, contours indicate the ion velocity in km/s. When carbon-III is initially detected, the velocity profile

is relatively flat. A small amount of radial variation in axial velocity develops later in the pulse. In general, the velocity is seen to decrease as the current in the acceleration decreases.

A single radial temperature profile is plotted in Fig. 3.5. The radial profile is measured 80 μs after the pulse trigger time. The measurement indicates a temperature profile that peaks on axis, with a radius of approximately 6 mm. The error bars show a 90% confidence interval for each measurement. The emission profile shape is similar to measurements seen with the ICCD, although temperatures measured for this pulse are lower than those seen in the high-energy ZaP-HD pulses presented in Chapter 2.

To verify the accuracy of the intensity of carbon-III measured by the Kirana, the data are compared to the signal measured with the PMT attached to the CCD spectrometer. The PMT has a higher dynamic range than the Kirana and digitizes the intensity signal at 20 MHz, a rate twenty times faster than the camera. Subsequently, data obtained with the PMT will show more rapid, small scale intensity fluctuations than the traces measured with the Kirana camera. Time-resolved intensity profiles are shown in Fig. 3.6. Data from the PMT are shown in black and data from the Kirana are shown in red and blue. The red trace is intensity measured with the radial telescope, while the blue is measured with the oblique telescope. Each trace has been normalized by its maximum value to better compare the shape of the measured emission.

Impurity line radiation measured by the Kirana tracks relatively well with the light intensity measured with the PMT. The magnitude and timing of the intensity fluctuations are similar across all three traces. The traces do show some discrepancies beginning around 80 μs, which could be due to a number of factors. The PMT views a plasma volume 10 cm downstream of the spectroscopy fiber bundle, and the measurement could differ due to axial variation in plasma parameters. In addition, both the PMT and Kirana measurements are line-integrated at their respective locations, which would provide another source of variation in the measured intensity. Finally, the discrepancy could be indicative of a time-dependent response of the phosphor screen. A similar fluctuation in response is seen from the Kirana sensor and is corrected in the data analysis. In order to quantify variation in the phosphor

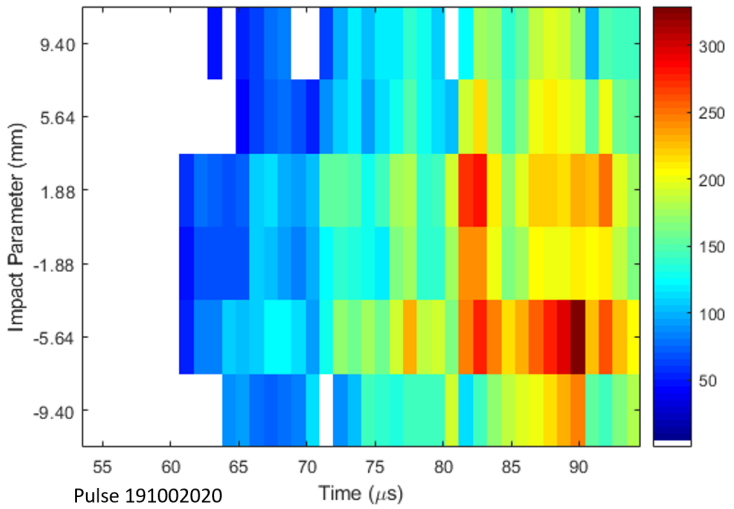

(a) Ion temperature (eV).

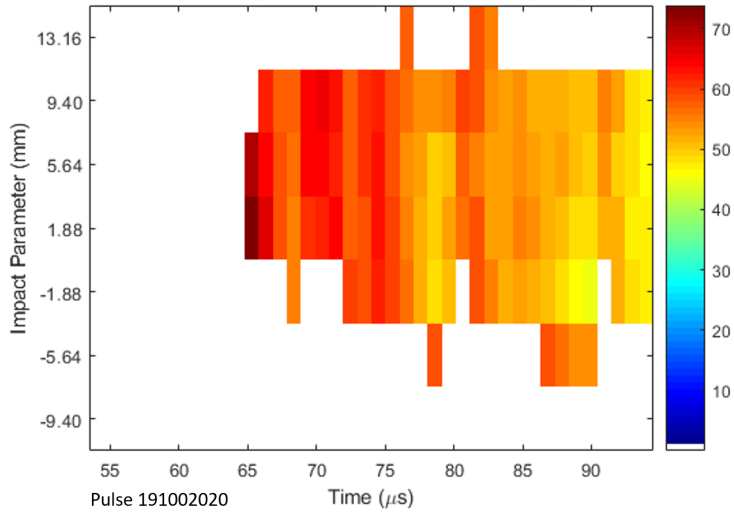

(b) Ion velocity (km/s).

Figure 3.4: Time-resolved profiles of ion temperature and velocity made from a single plasma pulse. These profiles were produced with a 90% H_2, 10% CH_4 gas mixture and charge voltages of 5 kV/3 kV. Detection of significant radiation from carbon-III begins around 60 μs from the pulse trigger time. Color contours in (a) indicate ion temperature in electron-volts. Contours in (b) show ion velocity in km/s. In both plots white space indicates the recorded signal was too dim for an accurate measurement.

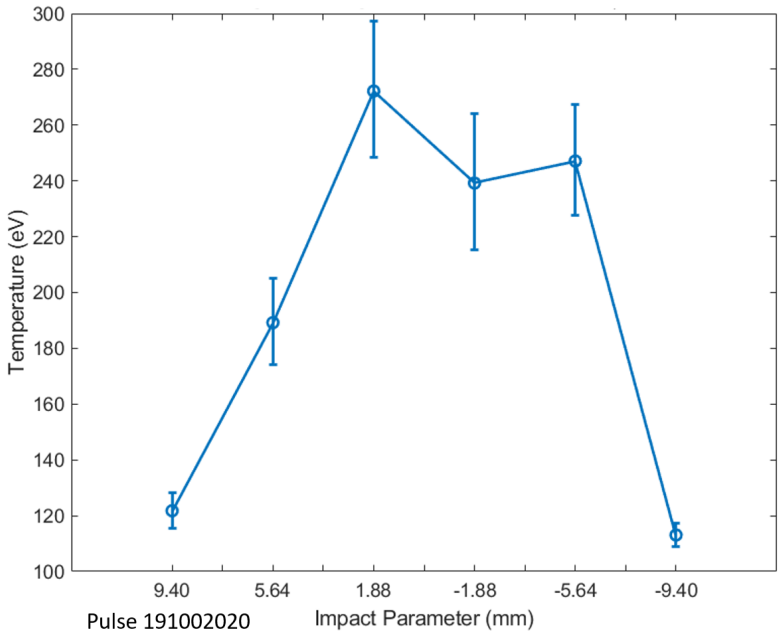

Figure 3.5: A single radial temperature profile from the time-resolved plot shown in Fig.3.4a. The profile is measured at 80 μs from the pulse trigger time. Measurements indicate a peaked temperature profile on axis. Error bars show a 90% confidence interval.

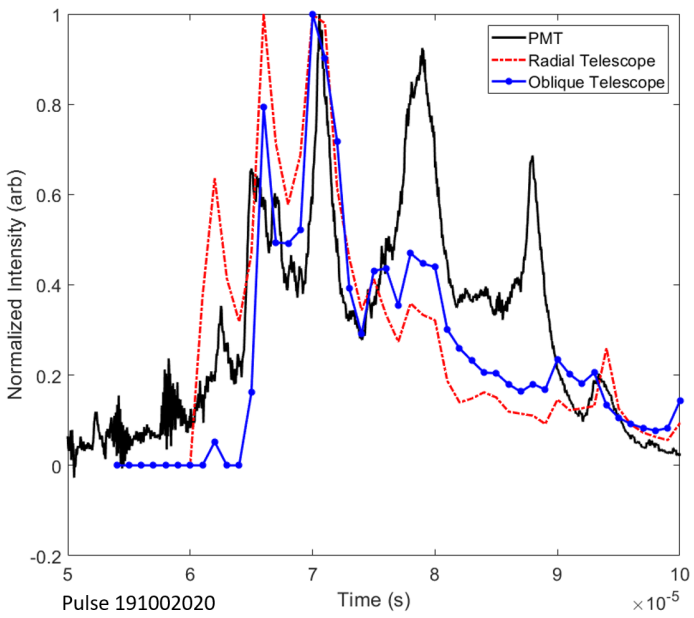

Figure 3.6: Time-resolved intensity of carbon-III radiation measured by the Kirana (red and blue) and photomultiplier tube (black). Each trace has been normalized by its maximum value to facilitate a comparison of the intensity profiles. The Kirana measurements were made 15 cm downstream of the nosecone while the PMT measurement was recorded 25 cm downstream of the nosecone.

Case	Accel Voltage(kV)	Compress Voltage (kV)	Peak Pinch Current (kA)	H_2/CH_4
I	5	3	42	90/10
II	7	5	70	90/10
III	9	8	142	95/5

Table 3.1: Key parameters for time-resolved spectroscopy cases presented in this chapter.

screen response, a very bright ultraviolet radiation source would be required.

As the plasma current increases, the profiles measured by the spectrometer change in both shape and value. The cases discussed in this chapter are shown in Table 3.1. The plots shown in Fig. 3.4 were created from case I data. Data for case II are shown in Fig. 3.7. This case has the same concentration of methane with an increase in peak pinch current from 42 kA to 70 kA. For this case, the emission diameter is approximately 2 cm. The temperature profile is flat and generally reaches higher temperatures. Ion velocity exhibits similar behavior to case I, with a fast-moving front measured earlier in time, followed by slower plasma as the current in the acceleration region decreases. Several radial velocity profiles from this pulse are shown in Fig. 3.8. For this case, the velocity appears to remain near approximately 100 km/s at the edge of the plasma but decrease near the machine axis.

Time-resolved profiles for the third case are shown in Fig. 3.9. The measured ion temperature profile shows large temporal and spatial fluctuations. A closer view of the spatial variation of temperature across the plasma diameter is shown in Fig. 3.10. The velocity profile is similar to the one shown for case II, but with fewer oscillations. The measured velocity starts high and falls off as the current decreases. Several radial velocity profiles for this case are shown in Fig. 3.11. For this case, there is no clear evidence of symmetric variation across plasma diameter that might indicate a pinch structure.

The velocity profiles measured for cases II and III do show some similarities to the composite profile shown for the ZaP experiment. Each profile has a fast-moving front, followed

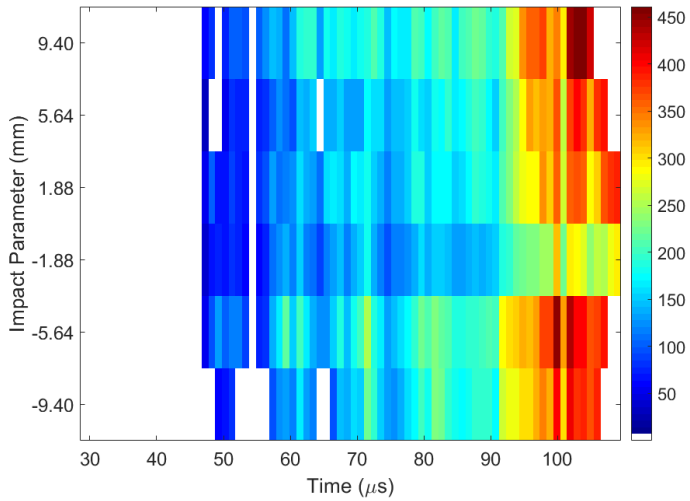

(a) Ion temperature (eV).

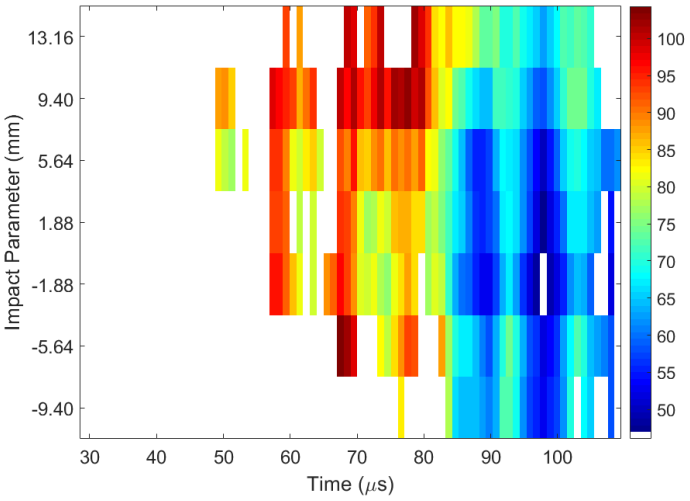

(b) Ion velocity (km/s).

Figure 3.7: Ion temperature and velocity profiles created from case II conditions. Figure (a) has temperature contours in eV and (b) shows velocity contours in km/s. This case shows a flatter temperature profile that increases with time. The velocity is less uniform than the profile seen in Fig. 3.4b. Data are from pulse 191002046.

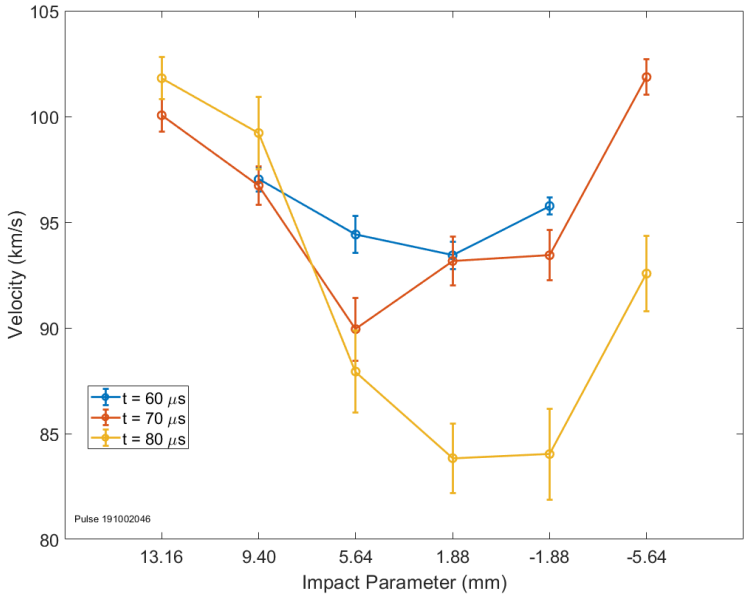

Figure 3.8: Several radial velocity profiles for case II taken from Fig. 3.7b. As time increases, the velocity near the machine axis appears to slow. Velocity on the $+x$ edge remains near 100 km/s.

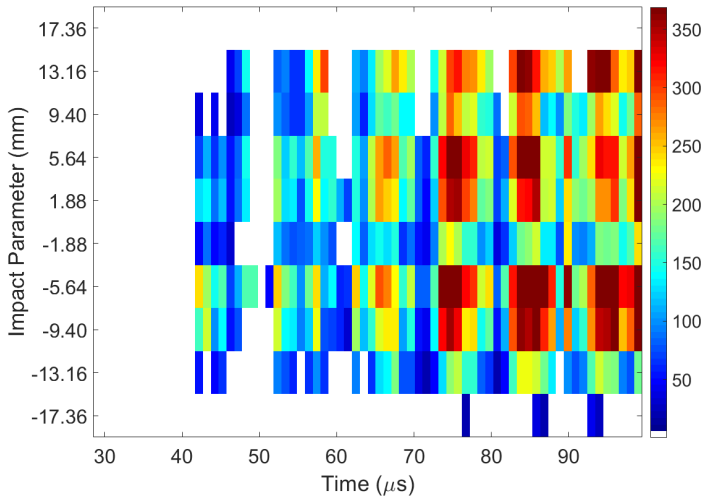

(a) Ion temperature (eV).

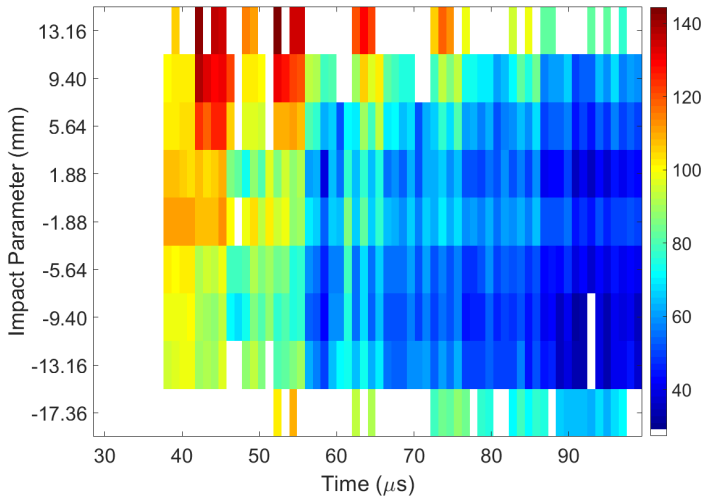

(b) Ion velocity (km/s).

Figure 3.9: Ion temperature and velocity profiles created from case III conditions. Figure (a) has temperature contours in eV and (b) shows velocity contours in km/s. This case shows a temperature profile that fluctuates randomly in time and space, although in general the temperature increases with time. The velocity profile is similar to case II, but has a higher peak velocity and is more radially uniform. Data are from pulse 190918007.

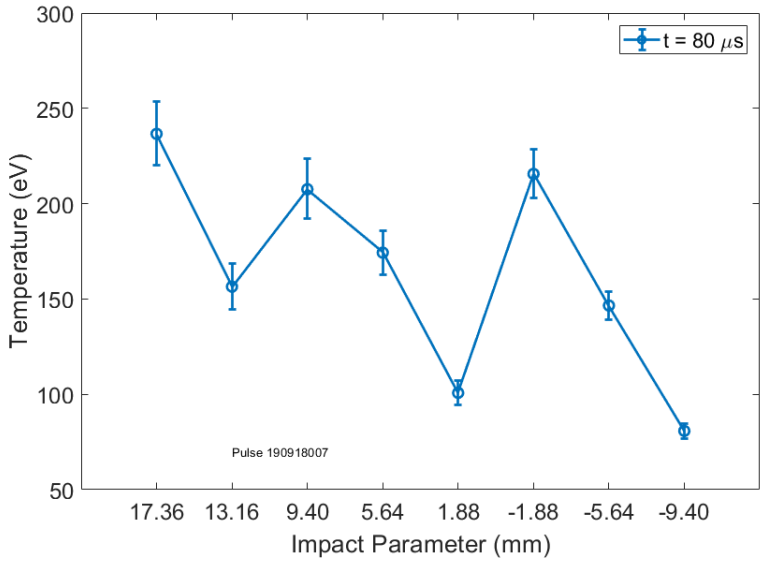

Figure 3.10: A radial temperature profile from the pulse shown in Fig. 3.9. Unlike the peaked temperature profile seen for the measurements of the pinch with lower current, this profile has no clear peak.

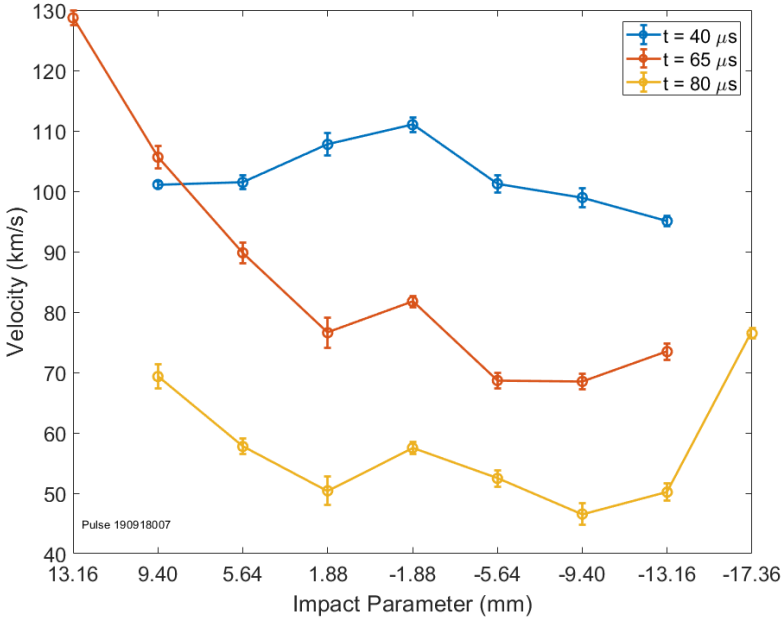

Figure 3.11: Several radial velocity profiles for case III. In this case, the velocity remains mostly flat across the diameter of the plasma and the value decreases over time. The early-time profile appears to show higher velocity near the machine axis, while later in time the velocity at the plasma edge is higher.

by a decrease in velocity that begins near the axis of the machine. The plots for ZaP-HD do not exhibit the "shear reversal" that is seen near $\tau = 0.5$ on Fig. 3.1. In addition, the velocity gradients measured in the ZaP composite plot are much steeper than those seen in Figs. 3.7b and 3.9b. During the first half of the quiescent period ($0 < \tau < 0.5$) for the original ZaP data, the velocity at the edge is 120 km/s, twice the velocity on axis. The flow shear, dv_z/dr, during the quiescent period is $7 - 12 \times 10^6$ s^{-1}. This exceeds the required flow shear calculated from typical ZaP parameters, $\frac{dv_z}{dr} \geq 0.1 k V_A = 5 \times 10^6 s^{-1}$ [50].

A range of required axial flow shear can be estimated from typical measured parameters on ZaP-HD. Simultaneous measurements of plasma radius, temperature, and density can be difficult to achieve. Diagnostic space is generally limited to one or two measurements at a single axial location, and in this case the plasma density was not measured simultaneously with time-resolved spectroscopy. However, measured parameters from prior experimental campaigns can be used to bound the estimated required shear for stability.

In general, typical values for pinch radius measured on ZaP-HD are between 10 and 1 mm. Using density data measured with DHI, the linear density is computed to be $\lambda_e = \lambda_i = 3.14 \times 10^{19}$ m^{-1} and assumed to be constant as the pinch radius changes. The magnetic field measured at $z = 15$ cm can be used with these values and Eqns. 1.5 and 1.6 to calculate the required radial shear of the axial velocity for stability for each case. The ion mass is assumed to be the mass of hydrogen, 1.67×10^{-27} kg. The perturbation wavelength is assumed to be equal to the pinch diameter, resulting in a wave number $k = \pi/a$. Calculated and computed values are shown in Figs. 3.12 and 3.13. Axially averaged mode data are also shown for each pulse, along with plasma current and pinch current measured at $z = 0$ and $z = 15$ cm. Measured velocity shear is calculated for each spectrum frame by taking the difference between adjacent measurements and dividing by the center-to-center spacing of the chords,

$$\frac{dv_z}{dr} = \left| \frac{v_{n+1} - v_n}{0.00367} \right| \tag{3.1}$$

where n is the chord number and the denominator indicates the chord spacing of 3.76 mm. The position of the shear measurement is chosen to be the impact parameter halfway between

two chord locations. For example, the shear value for an impact parameter of 0 mm is calculated from the velocity measurements made at 1.88 mm and -1.88 mm. These values are plotted over the calculated required shear for stability.

As indicated by the shear plots in Figs. 3.12 and 3.13, as the plasma current increases, so does the measured velocity shear. The number of measurements exceeding the lower stability threshold increases greatly between case I and case II. For case I, there is only a brief period of time around 85 μs where the standard deviation of the axially averaged mode data (shown in Fig. 3.12c) is entirely below 0.2. This indicates that the plasma is not well centered during the pulse. Case II mode data in Fig. 3.12d show low values of m_1 from 55 to 70 μs and again from 80 to 90 μs. Measured values of shear begin exceeding the minimum stability threshold for a 10 mm, $n_i = 10^{23}$ m^{-3} pinch around 70 μs and increase between 80 and 90 μs. Of particular note, the shear values at -3.76 mm and 7.52 mm are similar and relatively high between 80 μs and 90μs. The presence of this relatively symmetric shear could be indicative of a well-centered pinch.

Just as required shear values can be computed from measured parameters, a minimum pinch radius can be extracted from the measured values of velocity shear. Equations 1.6 and 1.5 can be manipulated to give the radius in terms of the shear and linear mass

$$a \geq 0.1 \left(\frac{dv_z}{dr} \right)^{-1} \sqrt{\pi \mu_0} \frac{I}{2\sqrt{m_i \lambda}}. \tag{3.2}$$

For case I, the mean computed radius that could be stabilized by the observed shear is $a_{mean} = 25$ mm. This is wider than the observed emission radius from the carbon-III measurements. For case II, the mean radius computed from the measured shear values is $a_{mean} = 13$ mm. This value is close to the distance between the symmetric shear measurements at -3.76 mm and 7.52 mm, providing further indication that the measured shear is correlated to the late-time quiescent period.

Case III shows significant shear beginning around 50 μs and continuing to the end of the pulse. The axially-averaged mode data in Fig. 3.13b are lowest between 50 and 60 μs, but do not show a clear duration where the plasma is well centered along the entire axis for

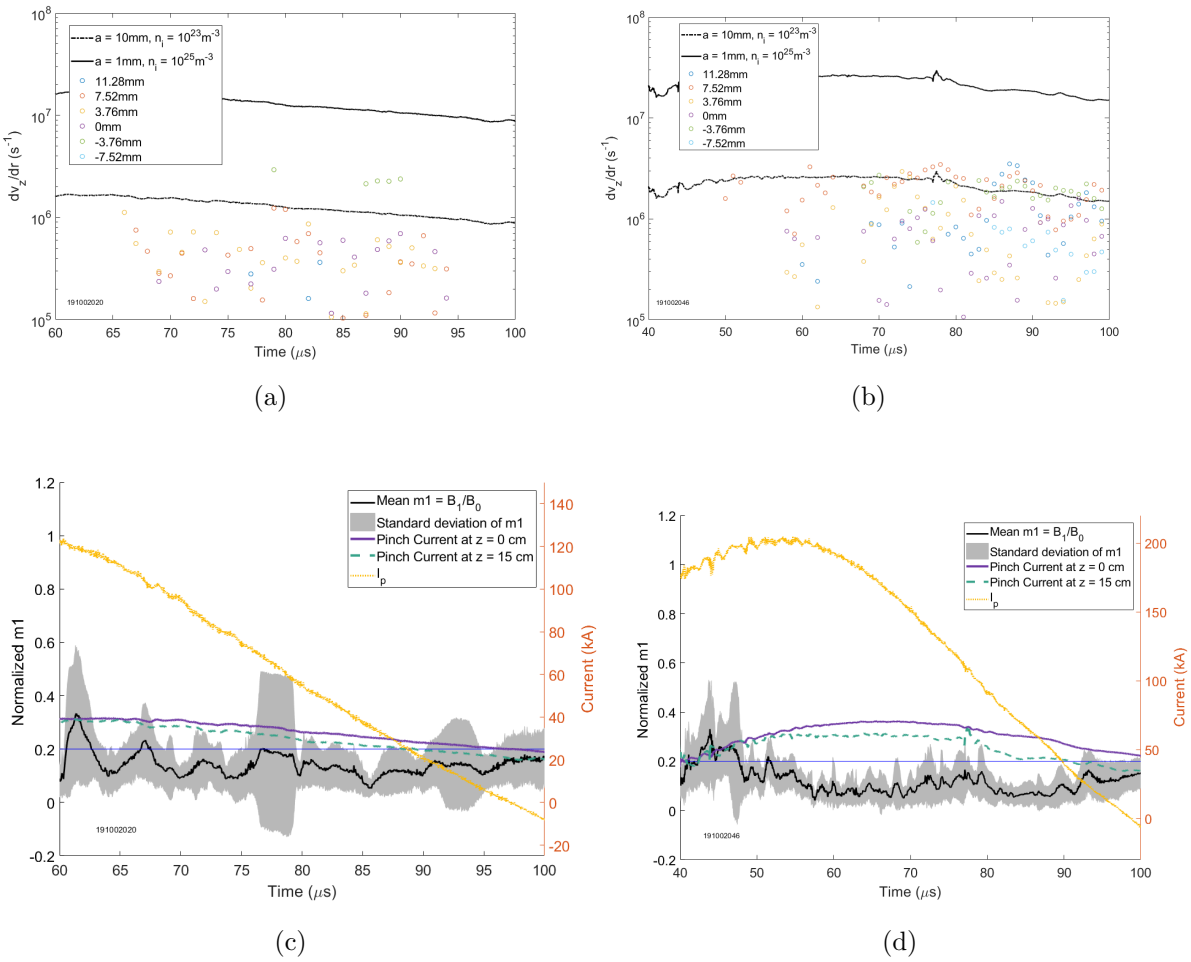

Figure 3.12: Calculated required radial shear of axial velocity and mode data for cases I and II. The black lines in (a) and (b) show the required velocity shear for a 10 mm radius pinch with $n = 10^{23}$ m^{-3} for the lower line and a 1 mm radius pinch with $n = 10^{25}$ m^{-3} for the upper line. Data for case I are shown in (a) and (c) and data for case II in (b) and (d). Of the cases, only case II has shear at multiple radial locations that persists in time.

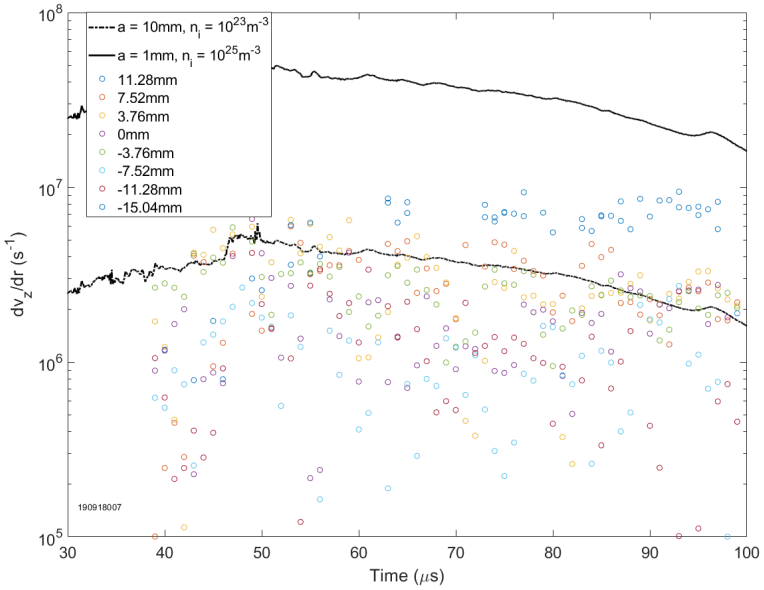

(a)

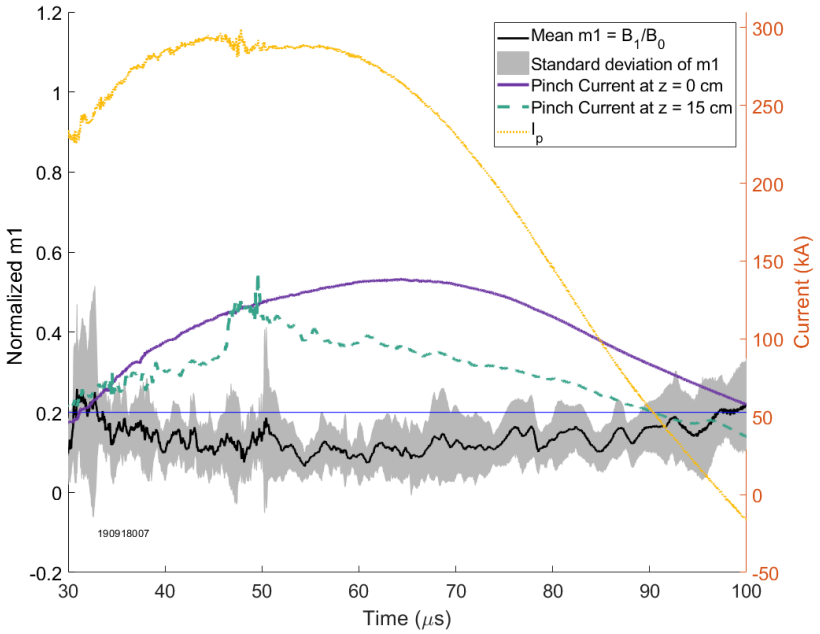

(b)

Figure 3.13: Radial shear of axial velocity and mode data for case III. The highest values of shear are seen almost exclusively on the $+x$ side of the measured profile. There is no clear extended quiescent period for this pulse.

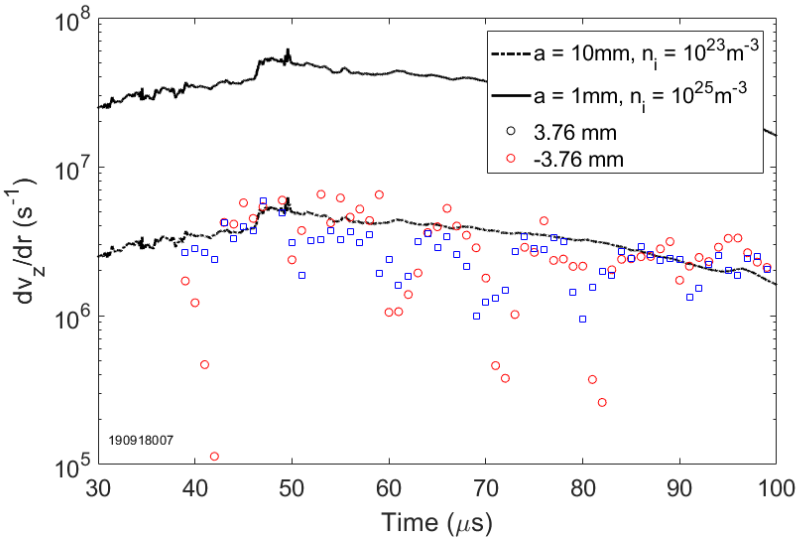

Figure 3.14: Shear measurements for case III at ±3.76 mm. The values are not identical, but seem to track relatively well.

an extended period of time. The highest shear values measured appear at the edge of the diagnostic at 11.28 mm, where the distortion from optical aberrations tends to significantly impact measurements. The shear measured at ±3.76 mm tends to be symmetric, although the value does not exceed the threshold to stabilize a 4 mm radius pinch with the chosen linear density. A plot of the shear values measured at ±3.76 mm is shown in Fig. 3.14. If we instead make the assumption that the pinch has a radius of 3.76 mm, we can use Eqn. 3.2 and the measured shear to determine what the linear density of the pinch might be. From the measured values, the mean linear density required for the pinch to be stable is $\lambda_i \geq 3.34 \times 10^{20}$ m^{-1}, approximately an order of magnitude higher than the value assumed for this analysis. This would result in a pinch with density $n_i = 6.62 \times 10^{24}$ m^{-3}, higher than any density measured on ZaP-HD. The lack of sufficient measured shear could account for the high fluctuations in the magnetic mode data and lack of clear quiescent period.

While there does appear to be some correlation between quiescent mode data and the presence of shear seen in the plasma, it is not clear that the data are concurrent enough to

indicate causality for these measurements. In particular, strong shear is not measured for case II during the low fluctuations in m_1 from 55 to 70 μs. Data presented in [50] show a clear correlation between the presence of shear in the assembly region of ZaP and a decrease in magnetic mode activity. One hypothesis is that the discrepancy is due to the chord-integrated nature of the measurement. In Fig. 2.13, the radiation from carbon-III indicated a flat temperature field similar to the one shown in Fig. 3.9a. Temperature measurements from carbon-V indicated a hotter, smaller structure present in the plasma. Likewise, without the ability to measure carbon-V with the time-resolved spectrometer, we cannot determine if there is a smaller, hotter, and faster-moving sheared structure present within a cooler bulk plasma. Resolving velocity profiles from carbon-V would increase the accuracy of the shear measurements for higher temperature plasmas.

The diagnostic limitations have an additional affect on the plasma performance. The limited dynamic range of the Kirana sensor requires that the plasma be doped with impurity ions, unlike the ICCD, which can generally resolve carbon impurity radiation with little to no impurity doping. Even with a methane concentration of 50%, the Kirana was unable to measure line radiation from carbon-V. In addition, the heavier methane gas changes the plasma behavior, decreasing the length of the quiescent period. This could be another explanation for why relatively weak velocity shear and low ion temperatures were measured.

Though there are limitations to the diagnostic resolution, time-resolved spectroscopy is a powerful tool for characterizing the behavior of Z pinches in the ZaP-HD experiment. Changes could be made to improve the accuracy and the resolution for pure H_2 plasmas. One possibility for increasing the amount of carbon present in the plasma without using methane would be to incorporate a graphite electrode. The FuZE device saw increased intensities of carbon line emission after installing a graphite nosecone. Should this diagnostic be used on FuZE, it is likely that measurements could be made without using a gas mixture. In addition, the diagnostic would benefit from installation of larger format focusing optics. The current optics used to relay light from the spectrometer to the ultraviolet intensifier are several centimeters thick at the mid point. Their curvature causes distortion of edge

chords, as well as any light at wavelengths higher or lower than 1 nm away from the focal wavelength. This is particularly detrimental for measuring the carbon-V line at 227.1 nm, which needs to be offset from the center to remove the bright light from carbon-III which can saturate the sensor. Increasing the size of the optics would reduce distortion and could allow the time-resolved spectrometer to collect data for carbon-V.

Chapter 4

THREE-DIMENSIONAL DIGITAL HOLOGRAPHIC INTERFEROMETRY

The digital holographic interferometer was developed on ZaP-HD to make detailed measurements of the plasma electron density structure. The diagnostic has successfully been used to measure small radii, high density pinches formed in the ZaP-HD experiment. To expand the capabilities of this diagnostic, an additional chord is added to the system to create three-dimensional measurements of the electron density in the Z pinch.

Three-dimensional holographic interferometry has been used in the past to image fluid jets [37]. A Korad ruby laser and holographic plates were used to take multiple simultaneous holograms of jet flow at different angles. The holograms were used to produce a three dimensional fluid density profile in r and z, shown in Fig. 4.1. This method required multiple sets of holograms to construct the density profile, rather than a single set of holograms. Data obtained from this diagnostic agreed well with previous results, indicating the usefulness of this early method. Three-dimensional DHI has also been successfully employed to measure strain in solid materials [2]. This method used a single sensor and three lasers of different wavelengths to record holograms at different angles to the solid surface. These experiments demonstrate the usefulness of three-dimensional DHI, although the technique varies from the procedure employed on ZaP-HD.

The three-dimensional interferometer developed for ZaP-HD was designed to use as much of the existing equipment and analysis as possible. Most of the optical components were carried over from the old system, and the EKSPLA NL 120 laser is operated at a higher amplification to expand the system to two chords. Additional beam splitters and two new DSLR cameras were procured to finish the expansion. The data processing largely uses the

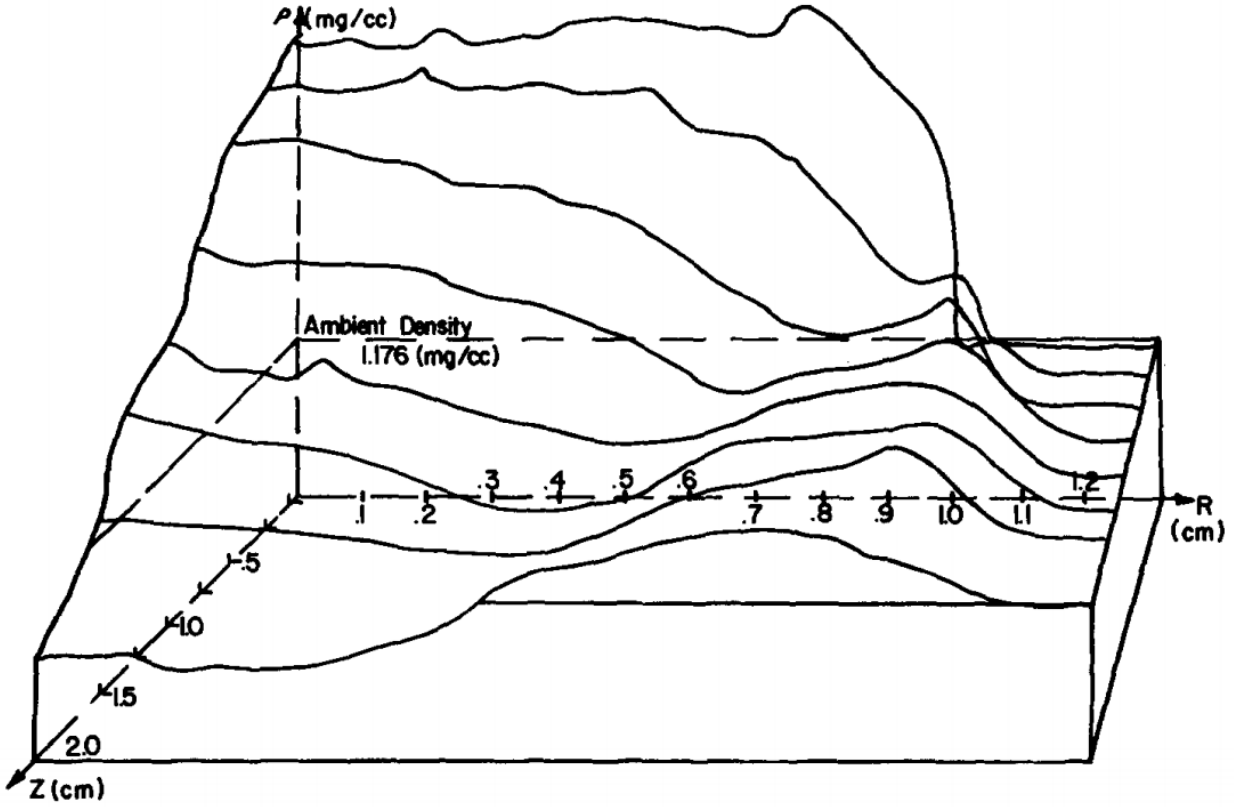

Figure 4.1: Three-dimensional results from multi-angle holographic interferometry measurements of a jet. The density is found by physically reconstructing the first order diffraction image and counting fringes. Error is introduced by unsteady flow and gaps in the data. The results are comparable to previous solutions obtained from an Abel inversion method. This image first appeared in [37].

same algorithms developed by Michael Ross. With some slight modifications, the new DHI system is able to produce three-dimensional renderings of the plasma electron density.

4.1 Experimental Apparatus

To collect an additional chord with DHI, the optical system was expanded and the mounting geometry altered. An additional camera was procured to collect holograms made by the second chord. The first camera was upgraded to capture a larger field of view with both chords.

Selecting a camera to record holograms required consideration of both the laser beam size and the fringe spacing given by Eqn. 2.25. The DHI system designed by Michael Ross used a Nikon D3200 DSLR camera with a 23.2 mm by 15.4 mm CMOS sensor and pixel size 2.85 microns. The size of the sensor was significantly smaller than the 35 mm beam diameter. Upgrading to a camera with a larger format sensor provides not only a view of a longer axial extent of the pinch, but also additional resolution in radius. This improves the ability of the system capture pinch structure that may be off axis.

Two Nikon D750 cameras were purchased as detectors for the new system. The D750 sensor size is 36 mm by 24 mm and has a pixel size of 5.9 microns. The larger format sensor can image the entire beam diameter in one direction. However, from equation 2.25, the misalignment angle between the scene and reference beams for this camera must be less than 2.5°, smaller than the D3200 misalignment angle requirement of less than 4°.

A challenge of designing a three-dimensional interferometer is that the two views of the plasma must be orthogonal to each other. All previous interferometry systems used in the ZaP lab have looked solely at the horizontal view of the pinch. This is easily accomplished with optical tables on either side of the machine. To create a view in the vertical direction, a truss to mount optics above and below the windows is required. A truss system to hold mirrors and beam splitters was designed out of 80/20 T-slot aluminum channel. The truss was designed from parts already available for use in the lab. For versatility of measurement, the truss spans as much of the assembly region as possible.

A rendering of the truss as it was first installed on ZaP-HD is shown in Fig. 4.2. A machine drawing of the final truss assembly is shown in Fig. 4.3. The truss is 44 cm wide to span most of the rectangular window. Additional crossbars were added to the bottom of the truss to increase the rigidity. The 80/20 aluminum material is slotted such that the cross bars can be easily positioned at various axial locations to move the DHI measurement. The extruded aluminum bars are secured with 80/20 specialty brackets and 1/4-20 screws, which facilitate easy attachment of optical equipment. Once the truss is installed around the machine assembly region, several 6" by 4" optical breadboards are installed on the aluminum beams where mirrors and beam splitters need to be positioned.

The mirror and beam splitter set-up is designed to minimize the number of optical towers needed and the keep the laser path lengths within the coherence distance of 0.9 m. Figure 4.4 shows a diagram of the beam paths around the vacuum chamber. An optical tower and the truss are shown in light gray, mirrors as solid black lines, beam splitters as dashed black lines, and a neutral density filter as a dotted black line. Approximate locations of the optical tables are indicated by black boxes. The beam propagation direction is shown with an arrow. The beam is split three times, once on the optical table upstream of the vacuum chamber and twice above the vacuum chamber. One DSLR camera is mounted above the optical table downstream of the vacuum chamber while the other is mounted below the table.

A careful alignment is required to ensure the beams have a misalignment angle less than 2.5°. For each beam pair, the path length for the scene and reference beams are measured from the final turning mirror to the camera. The angle between the beams is calculated and the mirror positioning is adjusted if necessary. A wire crosshair is used for fine-tuning the alignment of the scene and reference beams on the camera sensor. To better match the beam intensities, a neutral density (ND) filter is installed after the first beam splitter. ND filters are also attached to each camera to prevent stray light from the plasma from obscuring the hologram.

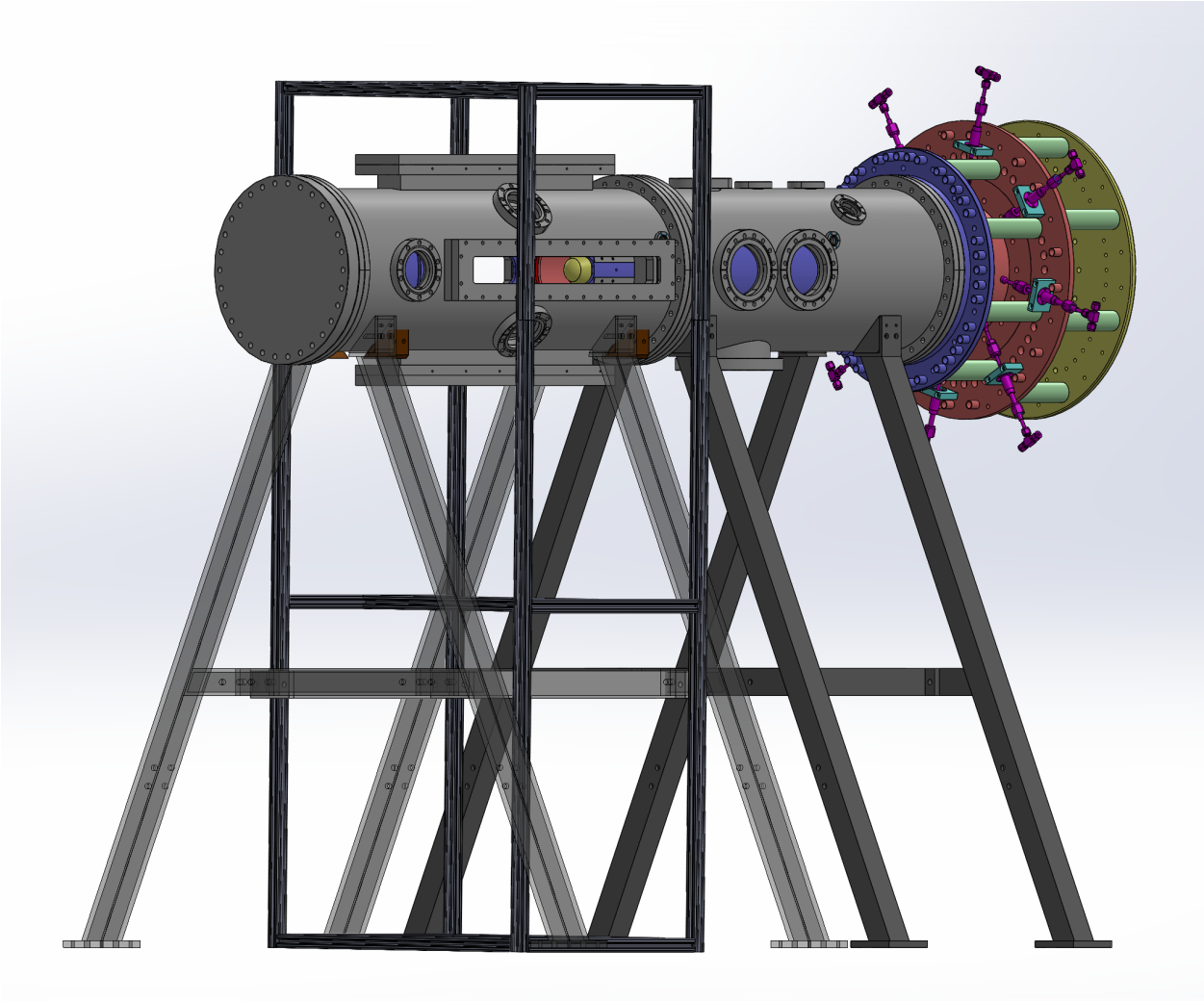

Figure 4.2: A rendering of the optical truss installed on ZaP-HD. Several cross bars allow placement of optics at a wide range of axial locations along the rectangular windows. .

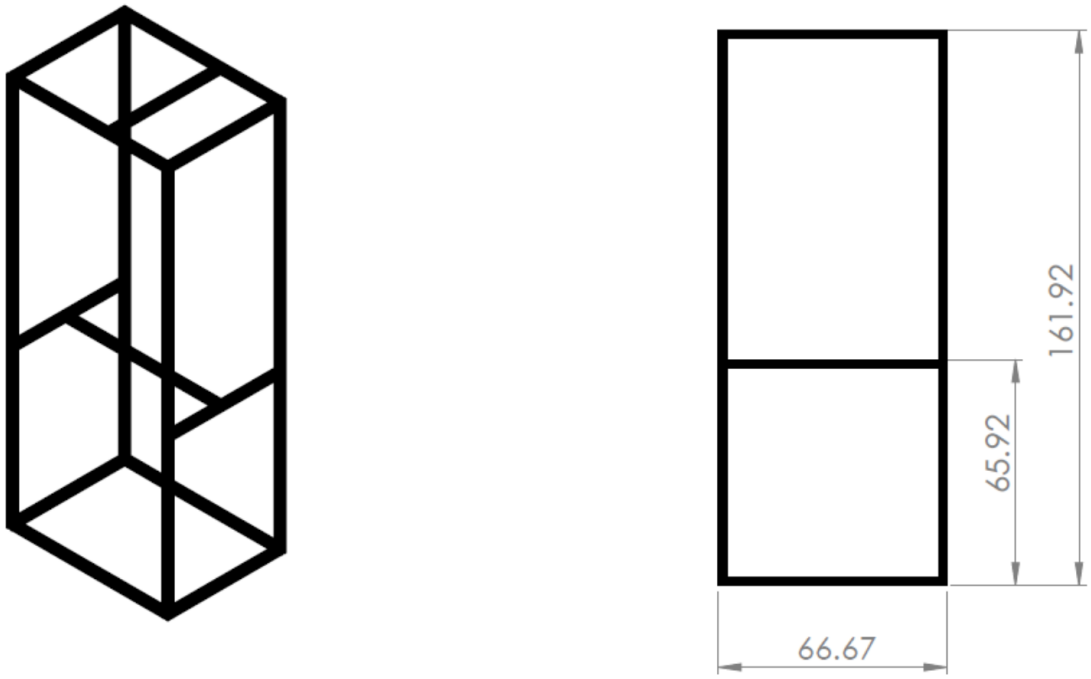

Figure 4.3: A machine drawing of the final design of the optical truss. Relevant measurements are shown in cm on the right hand view. The 80/20 aluminum material is slotted such that the cross bars can be moved to change the position of the optics. The width of the truss, which is not shown in the drawing, is 44 cm.

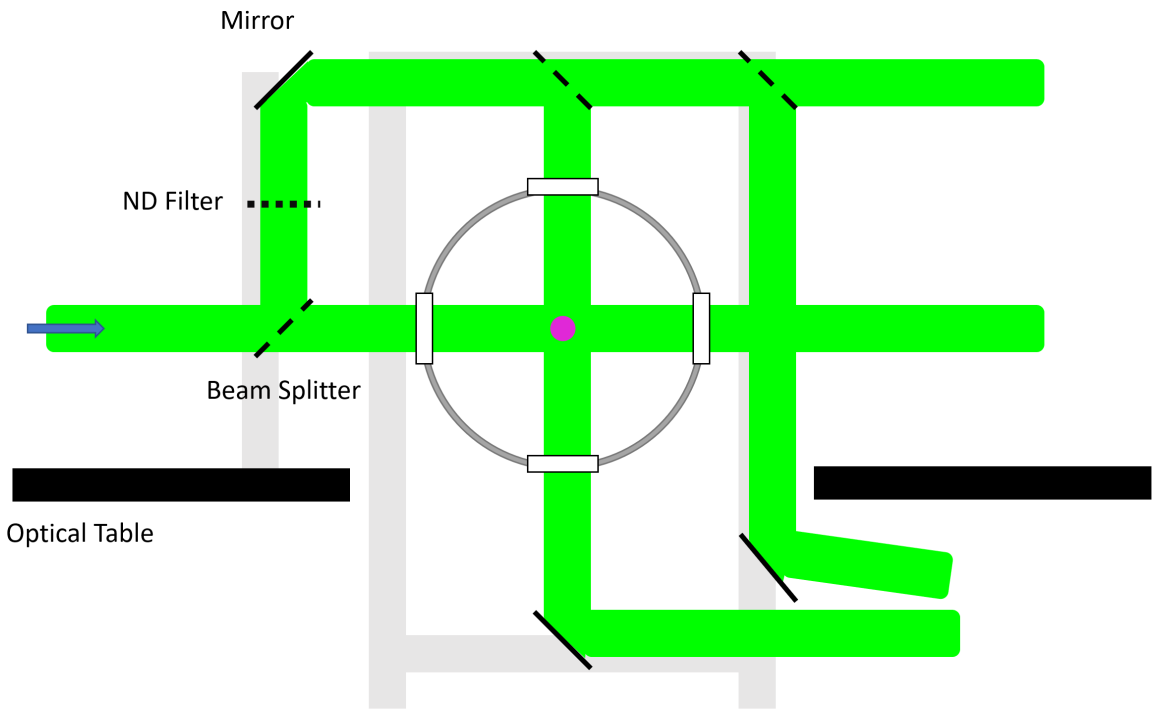

Figure 4.4: A drawing of the beam paths for 3D DHI. The arrow indicates the direction of beam propagation. The beam is split three times to form the scene and reference beams for the two chords. Additional mirrors are used downstream of the chamber to converge the two beams in the horizontal chord on a camera sensor.

4.2 Plasma Structure Measurements

Three-dimensional DHI data are processed using a similar method to the two-dimensional diagnostic. Two holograms are produced per plasma pulse, and baseline holograms are taken after every pulse. The holograms are digitally reconstructed in Matlab to produce the line-integrated density profile for the $x-z$ and $y-z$ planes. Holograms with coherent structure can be Abel inverted to obtain the electron number density.

Once the density is reconstructed, the profiles can be used to build a representation of the pinch structure in three dimensions. A program finds the radius at which the pinch density has fallen by half the peak value. These radii are used to create curves that estimate the edge of the structure. Each curve is comprised of four quadrants of an ellipse, where the major and minor radius for each quadrant are determined by the radii detected by the algorithm. The piecewise ellipses and their centroids are plotted along the z-axis to approximate the pinch structure and location.

Two line-integrated electron density profiles are shown in Fig. 4.5. The measurement of the $y-z$ plane is plotted in 4.5a and the $x-z$ plane is plotted in 4.5b. The density centroid is shown in black and the calculated edges of the structure are shown in magenta. Color contours represent particles per square meter. There is a large discrepancy between the width measured in the $y-z$ plane and the width measured in the $x-z$ plane. Higher line-integrated densities are also measured in the $x-z$ plane. The three-dimensional rendering of this structure is shown in Fig. 4.5c. The resulting structure is irregular and located far off-center in the horizontal impact parameter.

The nature of the line-integrated measurements can account for discrepancy in shape and electron density. Each chord measures a total volume inside the machine of 226.72 cm^3, given the beam diameter of 3.66 cm and the outer electrode diameter of 21.55 cm. The volume measured by both chords in the center of the machine is 38.51 cm, approximately 17% of the total chord volume. This leaves a large volume for each chord to measure plasma off axis that is not entrained in the central plasma column.

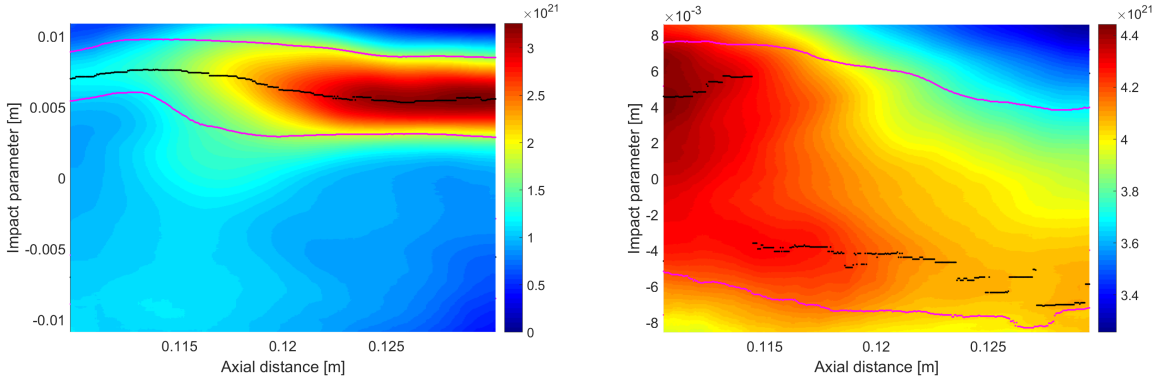

(a) Line-integrated electron density in $y-z$ plane (m^{-2}).

(b) Line-integrated electron density in $x-z$ plane (m^{-2}).

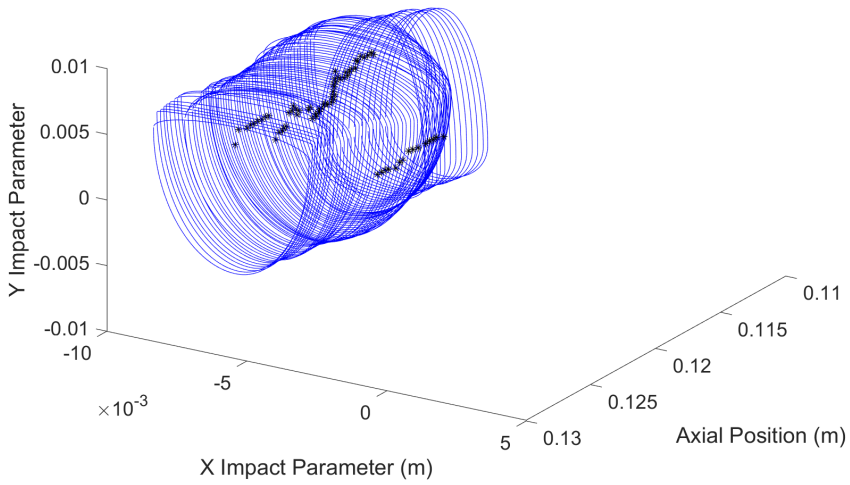

(c) Three-dimensional contours created from (a) and (b).

Figure 4.5: Line-integrated density from two DHI chords and a 3D rendering of the structure. Figure (a) shows the view of the $y-z$ plane and (b) shows the $x-z$ plane. Density contours are in number per square meter. The centroid and approximate edges of the plasma are identified and plotted as a 3D structure in (c). Data are from pulse 200114021.

The data from Fig. 4.5c are Abel inverted to resolve the electron number density and plasma structure. The two-dimensional Abel inverted density profiles are mapped in Figs. 4.6a and 4.6b. In the $y - z$ plane shown in Fig. 4.6a, all significant plasma density is included in a small, collimated structure. The $x - z$ plane plotted in Fig. 4.6b shows significant density outside of the calculated pinch radius. Once the Abel inversion is applied, the analysis again finds where the density has fallen to half the peak value to calculate the structure radius. This time, the average radius at each axial point is found. The Abel inversion assumes the profiles are cylindrically symmetric, and attempts to minimize the L2 norm of the two sides of each radial density profile. Taking the average radius extends this symmetry assumption to the 3D visualization. The three-dimensional density structure is shown in Fig. 4.6c. This plasma column is relatively uniform in radius along the z-axis. It is not centered on the axis but does not show evidence of a kink or sausage instability mode.

If the pinch is perfectly cylindrically symmetric, we expect each profile to be circular and the radius to be constant in z. In this case, we see both an axial variation in radius and that the profiles take on a more oval shape. The eccentricity of these profiles can be calculated from the two average radii,

$$e = \frac{\sqrt{a^2 - b^2}}{a} \tag{4.1}$$

where a is the major radius and b is the minor radius for each profile. A circle has an eccentricity of 0, and as eccentricity approaches 1 the shape becomes a flat line. The eccentricity gives a more quantitative measure of the profile symmetry. Error bars take into account how accurately the average major and minor radii shown in Fig. 4.6c represent the quantities measured in the Abel-inverted profiles. Larger error bars indicate a larger discrepancy in radius between the two sides of the radial profiles.

Data plotted in Fig. 4.6d show large variation in eccentricity along the z-axis. Profiles showing $e = 1$ indicate radial profiles where the density gradient caused the algorithm to calculate a radius of 0 mm, resulting in the profile being plotted as a line. Given that the average major radius for these profiles measures approximately 3 mm, an eccentricity of less than 0.75 indicates a difference between the major and minor radius of less than 1 mm.

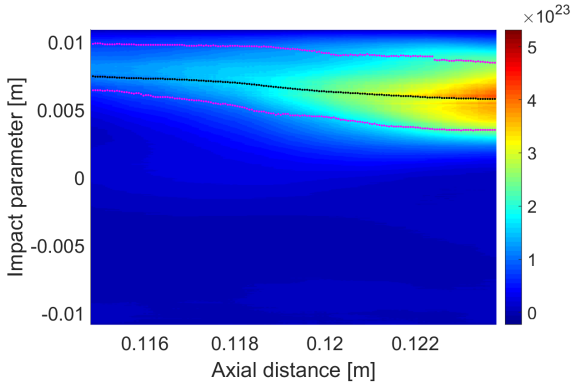

(a) Electron density in $y - z$ plane (m^{-3}).

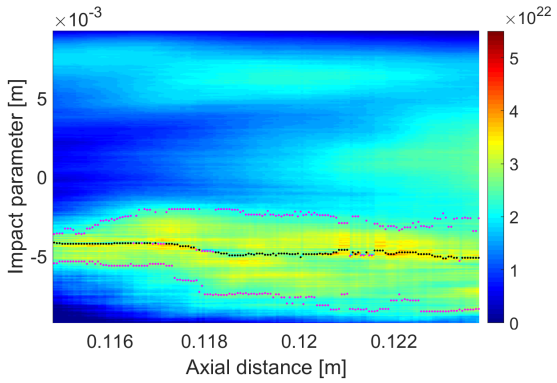

(b) Electron density in $x - z$ plane (m^{-3}).

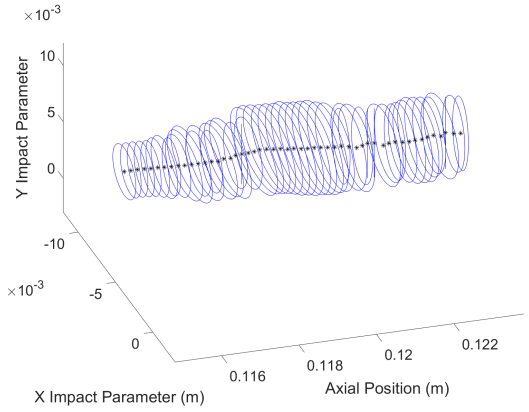

(c) Three-dimensional contours created from (a) and (b).

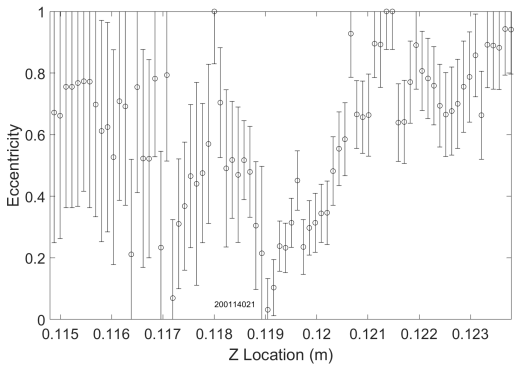

(d) Profile ellipticity of (c).

Figure 4.6: Abel-inverted electron density profiles and a 3D rendering of the resulting structure. Density in the $y - z$ plane is shown in (a) and the $x - z$ plane is shown in (b). The 3D rendering of the structure is shown in (c) and a calculation of the ellipticity of each axial profile in (d).

Many of the axial profiles have an eccentricity below this threshold, thus even though the profile shape appears to be highly elliptical along most of the axis, the discrepancy between major and minor radius is generally less than 1 mm.

The location of the density centroid found with this analysis can be compared to the magnetic mode data recorded 2 cm downstream at $z = 15$ cm. Figure 4.7 shows the average m_0 in black and magnetic field measured by probes at 0° in blue and 180° in red from the azimuthal array. Traces from the other probes in the array have not been plotted for clarity. It is important to note that the 0° label indicates an actual probe location of -22.5° from the x-axis of the machine, which means the measurement labeled 180° is actually located at 157.5° from the positive x-axis. A dotted black line indicates the trigger time for DHI. At this time, the signal from B_{180} is much higher than the average value. The normalized m_1 at P15 during this time is 0.22. Using this number and Eqn. 2.8 to relate the normalized m_1 to a displacement, the expected coordinates of the current centroid can be calculated. A value of 0.22 yields a radial displacement of 11 mm. Since the magnetic field signal at B_{180} is higher than any other probe, the expected (x, y) coordinates become

$$(x, y) = (\Delta r \cos\theta, \Delta r \sin\theta) \tag{4.2}$$

where here θ is 157.5°. The calculated (x, y) value for the given displacement is $(-10.6, 4.2)$. The centroid location calculated by DHI at $z = 12$ cm is (−5.0 mm, 6.2 mm). Using the coordinates of the centroid determined by DHI, an expected value for Δr and θ can be computed for $z = 12$. The resulting values are a displacement of 8.0 mm off axis at an angle of 128.9°, differing from the magnetic measurements by 3 mm and 28.6°. The discrepancy in angular location can be accounted for in part by the limited angular resolution of the azimuthal array; the spacing of the eight probes results in gaps of 45° between measurements. The second highest magnetic field measurement at the trigger time is at B_{135}, which is located physically at 112.5°. From the DHI measurement, we would expect this probe to measure higher magnetic field than the probe located at B_{180}. Additional factors that could account for this, as well as the difference in displacement radius, include the 3 cm axial difference in

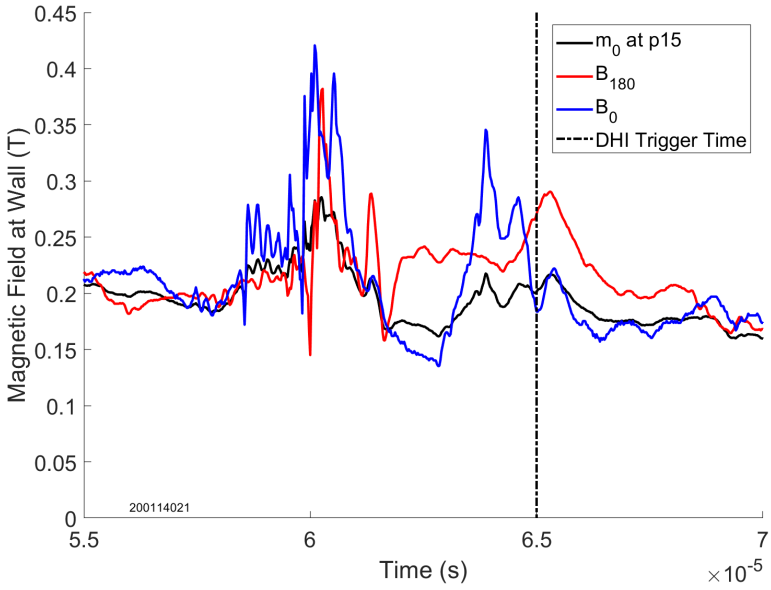

Figure 4.7: Select magnetic probe measurements from the azimuthal array at P15. The 0° index location of the magnetic probes is actually located −22.5° from the positive x-axis.

measurement location and some error in the laser beam positioning. Accounting for these differences, the centroid values computed from the magnetic data agree reasonably well with the density centroid calculations. The measured structure is located in the same quadrant as the current centroid, and has a similar displacement radius.

The dependence of the profile shape on the chosen density threshold can be measured by examining the change in the profile eccentricity as the threshold is changed. Figure 4.8 shows the calculated eccentricity for axial profiles when the edge density is set to 25%, 50%, and 75% of the peak electron density. As the edge density increases, the profile shape becomes less elliptical, but also less uniform. When an edge value of 25% of the peak n_e is chosen, the eccentricity of the profile tends to stay above 0.8 at every point along the axis. For both the 50% and 75% profiles, the eccentricity is generally lower than the 25% profiles, but is not consistent along the z-axis. This indicates greater fluctuations in the profile shape.

While the analysis used here operates under the assumption of cylindrical symmetry, the

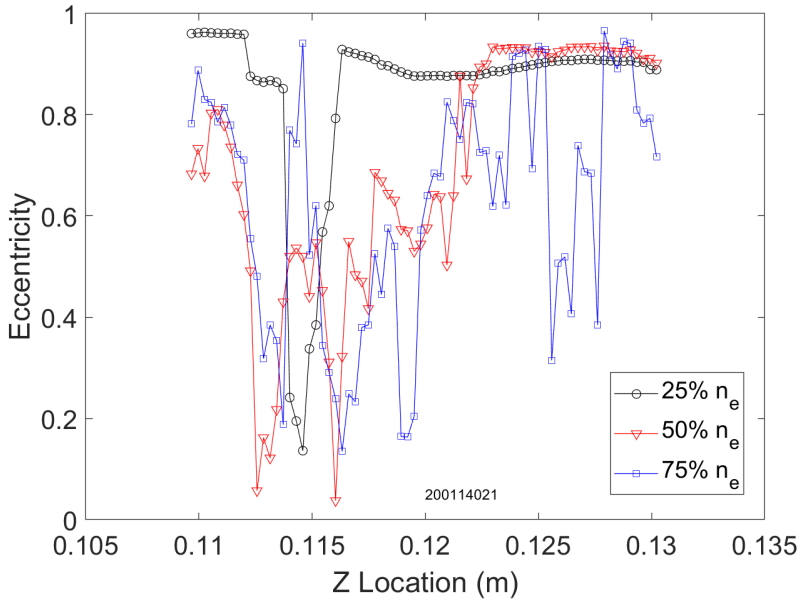

Figure 4.8: Variation in profile eccentricity with threshold density. The edge density of the pinch is set to be 25%, 50%, and 75% of the peak electron density. The eccentricity of the axial profiles is then computed for each case.

diagnostic can be used to image any plasma structure with sufficient density. Figure 4.9 shows electron density profiles for a structure that appears to be formed from several plasmoids. The holograms were captured during a spike in the magnetic mode data at $z = 15$, which is indicative of a disruption in the pinch. The structure could be a kink instability with a relatively long wavelength, approximately 2 cm based on the apparent half-wave in Fig. 4.9b. Both chords measure density in the range of 10^{23} m^{-3}, although the peak density in the $y-z$ plane in Fig. 4.9a is about twice what is calculated in the $x-z$ plane in Fig. 4.9b. The peak density measured in the $y-z$ plane occurs at an axial location where two plasmoids are seen side-by-side in the $x-z$ plane. If one structure is directly behind the other in the view of the $y-z$ chord, this provides a reasonable explanation for the discrepancy in the measured density values. The three-dimensional structure is shown in Fig. 4.9c. The shape of the structure is somewhat reminiscent of the longer-scale fluctuations seen in both the FuZE machine and ZaP-HD near the end of a pulse. However, this three-dimensional representation of the data tends to oversimplify the structure measured by the holograms. Any structure outside of the edge of the central column is neglected, and the nuances seen by comparing the axial variations in density are lost.

4.3 Suggestions for Improvements

There are a number of improvements that would benefit the 3D DHI system. To improve the measurement repeatability, a better mounting system for the vertical chord should be devised. The camera mount used currently is an optical breadboard attached to a mounting clamp on a large optical tower. The tower has a heavy base that sits on the floor of the lab, but is not bolted to a surface. Vibrations from the vacuum chamber or walking scientists can misalign the camera, and care had to be taken to check the camera alignment immediately before running an experimental campaign. Devising a system to mount the camera to the bottom of the optics table would preserve the benefits of the current system's small footprint and path length matching layout while also stabilizing the detector.

Another issue currently plaguing the 3D DHI setup is the difference in beam intensity for

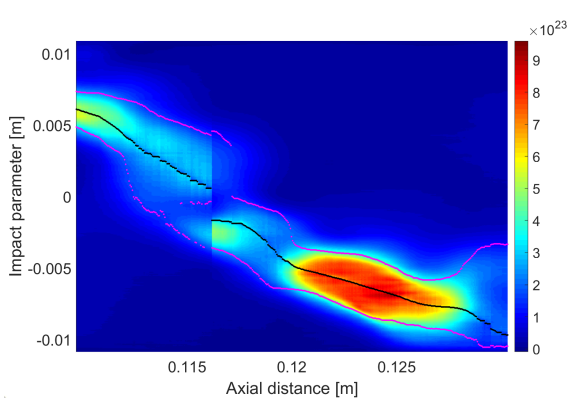

(a) Electron density in the $y - z$ plane (m^{-3}).

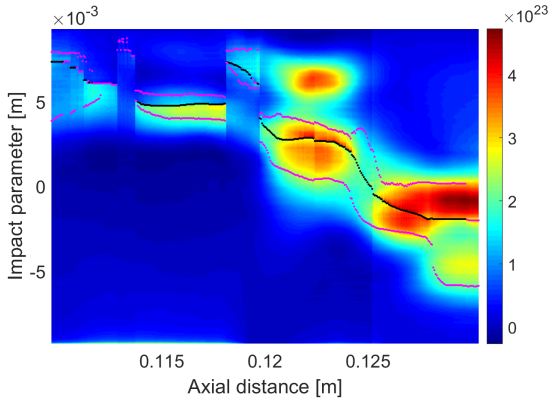

(b) Electron density in the $x - z$ plane (m^{-3}).

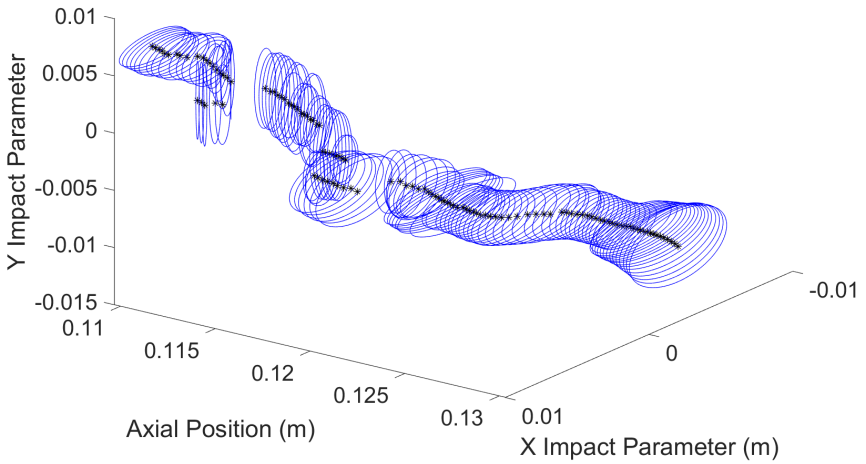

(c) Three-dimensional contours created from (a) and (b).

Figure 4.9: Electron density calculated for a more complex plasma structure. The $y - z$ plane is shown in (a) and the $x - z$ plane in (b). A three-dimensional representation of the structure is shown in (c). The plasma appears to be suffering from a kink instability.

each of the chords. In order to capture holograms close to the nosecone, where Z pinches are reliably seen on the Kirana camera, the second and third beamsplitters were placed on the optical truss. While this minimized the system footprint, it created a disparity between the intensity of the scene and reference beams for each chord, and between the chords themselves. Several other configurations were attempted, but could not fit within the footprint of the optical table. In addition, both scene beams are significantly attenuated by the rectangular windows, which become coated in soot. Part of this issue can be remedied by a reorganization of the optical tables in the lab. For instance, if this system were moved to the FuZE lab, the wider optical tables would easily facilitate an alignment where the beams are split evenly upstream of the vacuum chamber. Solving the issue of window soot would require additional modification of the experiment. An extended flange has been designed for FuZE to move the windows farther from the plasma, but has not been fabricated or implemented.

Modifying the system to have a third viewing chord would provide useful additional information for reconstructing the three-dimensional structure. A third chord passing through the same axial location at an angle to the $x - z$ and $y - z$ chords would give information to better understand the orientation of off-axis density structure. For instance, if another chord had been used to produce the data for Fig. 4.9, the information from the third view could be used to determine the y-location of the blob outside of the main structure at $z = 12.25$ cm in Fig. 4.9b, and confirm if this affected the calculated peak electron density in Fig. 4.9a. A third chord would provide a reference for the orientation of otherwise disparate structures sometimes seen in the hologram pairs.

Finally, an ideal upgrade to this diagnostic would be to fully enclose the optical tables, and design better beam tube mounts or enclosures for the truss. The setup used for these measurements incorporated beam tubes upstream of the vacuum chamber, but most of the beam path around the chamber and downstream was left untubed. This was due to a combination of a lack of space and a lack of a practical method for mounting beam tubes vertically and under the optical tables. The upstream portion of the beam path suffers the most from air currents as that portion of the system is closest to the vacuum pumps which both disturb

the air and create heat. There are a number of solutions that would reduce the effects of the vacuum pumps and other disturbances on the system. The vacuum pumps could be enclosed in an insulated box, which would have the additional benefit of reducing the sonic noise in the lab. Likewise, the optical tables could be encased in blackout boxes, which would reduce the time to align the system by eliminating all beam tubes except those immediately surrounding the vacuum chamber.

The newly expanded digital holographic interferometry system successfully captured three-dimensional density structures in the ZaP-HD machine. The Abel-inverted data have provided the first three-dimensional rendering of the flow Z pinch electron density. The diagnostic can provide insight into the plasma structure even when there is not a pinch present, as shown by the holograms of the presumed kink instability. The calculated density centroid agrees well with magnetic field measurements near the same location. Further improvements could be made to aid in the system alignment and analysis of the structures seen in the holograms. This diagnostic will provide valuable information on future experiments as the sheared flow stabilized Z pinch is scaled up to even higher densities.

Chapter 5

PLASMA-MATERIAL INTERACTION EXPERIMENTS

Plasma-material interactions (PMI) are an important but poorly understood part of many fusion experiments and electric propulsion devices. This system of processes, including sputtering, ionization, recombination, and emission, all simultaneously occur at the interface between the plasma and solid surface. This affects not only the plasma boundary, but also the bulk plasma behavior. The experimental effort presented here aims to analyze the plasma parameters and material deformation to better understand the processes occurring the ZaP-HD device and the effects of these processes on the plasma performance and material surface. The physics of energy transfer from the plasma target to the material are investigated, the material loss to the plasma is quantified, and the impacts of varied plasma parameters on the material are examined.

A number of experiments are currently used to investigate PMI in a variety of temperature and density regimes. Some are used by NASA to simulate atmospheric re-entry. The Michigan Plasmadynamics and Electric Propulsion Laboratory uses a helicon source to generate argon plasmas with densities of 10^{17} m^{-3} and electron temperatures on the order of 5 eV [33]. Additional NASA facilities use plasma wind tunnels [5], inductively heated sources [20] or hypersonic ballistic facilities [41] to achieve similar plasma parameters. Many experiments investigate conditions relevant to fusion reactor environments. The Magnum-PSI device uses a linear plasma generator with a flow-aligned magnetic field of approximately 1 T to study PMI in ITER-relevant conditions [15]. These hydrogen plasmas reach ion densities of 10^{20} m^{-3} at a temperature around 1 eV. The MAGPIE [10] and PISCES-B [21] devices create similar plasmas to assess how PMI will affect the ITER divertor. Experiments achieving the most extreme plasma parameters are used to explore material properties and

Parameter	Magnum-PSI	NAGDIS-II	PISCES-B	ZaP-HD
Electron Temperature (eV)	< 5	10	3 to 50	300 to 1000
Electron Density (m^{-3})	10^{20} to 10^{21}	10^{18} to 10^{19}	10^{17} to 10^{19}	10^{23} to 10^{24}
Ion Flux ($m^{-2}s^{-1}$)	10^{24} to 10^{25}	10^{21} to 10^{22}	10^{21} to 10^{23}	10^{27} to 10^{28}
Ion Fluence (m^{-2} per exposure)	10^{26} to 10^{28}	10^{26}	10^{26}	10^{24} to 10^{25}
Incident Ion Energy (eV)	< 400	< 100	10 to 500	300 to 1000

Table 5.1: Comparison of relevant parameters for PMI experiments from [34].

hydrodynamics for stockpile stewardship. Magnetically imploded metal liners are used at the Los Alamos ATLAS project to achieve high energy densities and particle velocities [42]. ATLAS generates a 2000 T magnetic field and rapidly heats the liner to study material failure and converging shocks in conditions relevant to nuclear explosions [58].

The ZaP-HD experiment offers a unique platform for studying PMI in a high energy environment for relatively long time scales. The Z pinches generated in ZaP are much hotter and denser than those used in plasma wind tunnels while being longer-lived than those used for stockpile stewardship applications. A comparison of parameters achieved on ZaP and some existing PMI experiments is shown in Table 5.1. Initial experiments on ZaP-HD were carried out by Jon Weed and focused on identifying the Kolmogorov scale and viscous damping time of the plasma using a tripping probe [60]. The series of experiments conducted for this dissertation investigates how changing the kinetic and thermal energy of the plasma affects the damage to the material surface and the plasma performance when a target is inserted into the plasma path.

In order to design plasma-material interaction experiments on ZaP-HD it is important to understand the experimental variables that can be controlled and the PMI processes that can be measured. The easiest variable to control on the ZaP device is the amount of energy in the plasma by manipulating the capacitor bank voltages. For this experimental campaign,

the plasma temperature was varied while the kinetic energy was held constant. The kinetic energy is set by the acceleration imparted to the plasma from the Lorentz force applied in the coaxial accelerator. The thermal energy is mostly imparted through the compression of the plasma in the assembly region. For this experimental campaign, the kinetic energy was held constant by keeping the acceleration bank voltage constant, while the compression bank voltage was varied to change the amount of current in the pinch.

A large suite of diagnostics is used to measure plasma parameters and the changes to target surfaces that have been exposed to the Z pinch. Digital holographic interferometry, spectroscopy, magnetic field probes, and the Kirana camera are all used to monitor plasma parameters near the target. A thermistor at the back of the target measures changes in the material temperature after each plasma pulse. A scanning electron microscope (SEM) and energy dispersive x-ray spectroscopy (EDS) are used to analyze topographical and chemical changes to the target surface. Data from these diagnostics provide information on changes to both the material targets and the impinging plasma.

5.1 Theory

When a solid object is inserted into a plasma, that object will generally become negatively charged with respect to the plasma potential. The light electrons have higher mobility than the more massive ions, and consequently impact the solid object first. To maintain quasineutrality in the bulk plasma, a thin layer called the sheath forms adjacent to the solid surface where the ion density exceeds the electron density. If ions enter the sheath, they are accelerated through the sheath potential and impact the solid surface, where they can recoil, become implanted, or cause sputtering.

The energy with which ions and high energy electrons impact the solid surface is determined by the properties of the bulk plasma. The Bohm Criterion dictates the minimum

speed at which particles enter the sheath as

$$v_{se} \geq c_s \tag{5.1}$$

where c_s is the speed of sound [56]. For an isothermal fluid model, this necessitates that

$$v_{se} = c_s \tag{5.2}$$

as the particle velocity cannot exceed the sound speed. This expression of the Bohm criterion is for plasmas where the ion temperature is small compared to the electron temperature. In a plasma with non-negligible ion temperature, the generalized Bohm criterion is

$$\int_0^\infty \frac{f_{se}^i(v)dv}{v^2} \leq \frac{m_i}{kT_e} \tag{5.3}$$

where $f_{se}^i(v)$ is the 1D ion velocity distribution at the sheath edge. Analysis by Riemann [43] has generalized the non-zero T_i Bohm criterion to show

$$v_{se} \geq c_s = \sqrt{(kT_e + \gamma kT_i)/m_i} \tag{5.4}$$

where $\gamma = 1$ for isothermal flow, $\gamma = 5/3$ for adiabatic flow with isotropic pressure, and $\gamma = 3$ for 1D adiabatic flow.

The particle flux density to a solid surface can be related to the plasma properties

$$\Gamma_{se} = n_{se}v_{se} = n_{se}c_s \approx \frac{1}{2}n_0[k(T_e + T_i)/m_i]^{1/2}. \tag{5.5}$$

Here *se* denotes properties at the sheath edge. Typically, the sheath thickness is much smaller than the characteristic size of the plasma, and the flux at the sheath edge is taken to also be the flux to the wall. The floating potential of the wall can be expressed by relating ion and electron flux densities. This quantity is important to calculating the particle impact energy. Taking $\Gamma_{se}^i = n_{se}c_s$ and expressing the electron flux density using the Boltzmann relation

$$\Gamma_w^e = \frac{1}{4}n_w\bar{c_e} = \frac{1}{4}n_{se}\exp[eV_w/kT_e]\bar{c_e}. \tag{5.6}$$

the particle fluxes are equated to yield the relation for the floating potential

$$\frac{eV_w}{kT_e} = 0.5 \ln \left[\left(2\pi \frac{m_e}{m_i} \right) \left(1 + \frac{T_i}{T_e} \right) \right]. \tag{5.7}$$

In a manner similar to the derivation of the particle flux to the solid surface, the heat from the plasma to the target can be related to plasma parameters. For a Maxwellian distribution, the one-way heat flux to the solid surface is

$$q_{ss}^e = 2kT_e\Gamma_{ss} = 2kT_e\Gamma_{se} \tag{5.8}$$

The expression for heat flux due to the ions is more complicated, since the ions are accelerated by the floating potential of the solid object. Stangeby [56] analyzes the ion distribution as a drifting Maxwellian with velocity c_s to define the ion power flux to the solid surface as

$$q_{ss}^i \approx (2kT_i + |eV_w|)\Gamma_{se}. \tag{5.9}$$

The second term in the right hand side is the power lost by the energetic electrons in the sheath. The total sheath heat transmission is then given by the sum of the ion and electron components,

$$q_{ss} = q_{ss}^e + q_{ss}^i \tag{5.10}$$

The equations above give the particle and heat flux for a floating surface in an unmagnetized plasma, with a drifting Maxwellian ion distribution at the sheath edge. Values computed from these equations will grossly overestimate the heat flux to the solid surface. Several adjustments can be made to more account for these discrepancies. Modeling by Bissel and Johnson showed that for a collisionless plasma with velocity-independent ionization of source neutrals, the ion heat transmission coefficient is reduced to $1.5kT_i$ [9]. In addition, the magnetic field will greatly reduce the particle flux to the target, provided the field lines are parallel to the surface. To approximate the reduction in heat flux to the solid surface, the Engelhardt model is applied. The Engelhardt model requires that the diffusion coefficient be high for all species, and the neutrals penetrate into the bulk plasma. Applying this model

to a surface geometry parallel to the magnetic field lines [55] yields the reduced particle flux to the surface

$$\Gamma = \left(\frac{D_\perp}{2Lc_s}\right)^{1/2} nc_s \tag{5.11}$$

where L is a characteristic length for the surface, chosen here to be the diameter of the target, and $D_\perp$ is the perpendicular diffusion coefficient. The Bohm diffusion coefficient is described by the plasma parameters,

$$D_\perp = \frac{1}{16}\frac{kT}{eB}. \tag{5.12}$$

The pinch current is assumed to be uniform and the average magnetic field in the pinch is used to calculate the diffusion coefficient. Employing this technique has been shown to better approximate heat fluxes in magnetized plasmas where the surface geometry is parallel to the field lines [36].

5.2 Experimental Apparatus

A variety of considerations were included when designing the PMI testbed for ZaP-HD. The initial design was based on the apparatus fabricated by Weed, but required major modifications to both the target shape and mounting system. The targets had to be cylindrical and less than 1 cm tall to fit easily in a scanning electron microscope for surface analysis. The target diameter was optimized to be approximately the same size as larger Z pinches seen in ZaP. A rendering of the design is shown in Fig. 5.1. A translation stage is attached to an extended flange so the target may be moved in and out of the assembly region of the vacuum chamber. A copper adapter connects the translation stage to the 1/2" boron-nitride mast with a 1/4-28 set screw. The mast holds a cylindrical graphite target 3/8" in diameter by 0.3" long.

A cross sectional drawing of the boron-nitride mast is shown in Fig 5.2. The mast is hollow, allowing a ceramic thermistor to be inserted behind the target. The thermistor leads exit the mast through a hollow set screw and a hole in the copper adapter. The leads are attached to gold crimp connectors which facilitate easy detachment for target removal. The

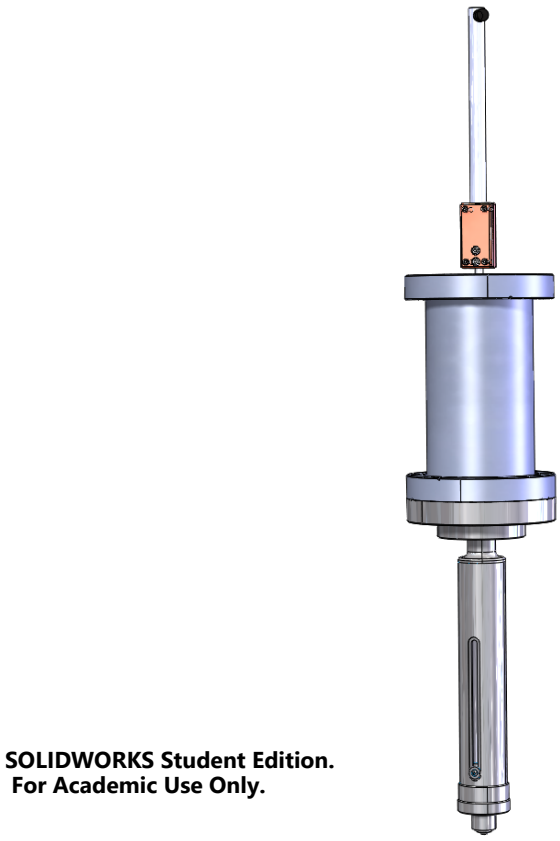

Figure 5.1: A render of the full PMI target testing assembly. A translation stage is attached to a vacuum flange. The rectangular copper adapter is threaded, and a set screw connects it to the 1/2" boron-nitride mast. The mast holds the 3/8" diameter target, shown here in black.

gold crimp connectors attach to a shielded twisted pair of magnet wire leads connecting to a DB25 vacuum feed-through. On the air side of the feed-through, a DB25 breakout board is used to connect the thermistor to a multimeter. This allows the operator to check the target temperature before and after each plasma pulse.

The target shape is designed to test the effects of the plasma kinetic energy and thermal energy on the plasma-surface boundary. The target shape is a 3/8" diameter cylinder that is 0.3" long. Targets are constructed from graphite and boron-nitride. Initially, targets were held in place with a 4-40 stainless steel set screw that was threaded into the top of the boron-nitride mast. After four targets were inserted into and removed from the testing apparatus, the threads had worn down and were no longer able to hold the set screw in place. The design was modified so the current fastening system uses holes that are drilled and tapped into the targets and a longer 4-40 set screw that pins the targets into place. A picture of the boron-nitride mast with a graphite target before being exposed to plasma is shown in Fig. 5.3a. Figure 5.3b is an image of the target and BN mast after being installed in the vacuum chamber. The target sits approximately 24 cm downstream of the nosecone tip.

Two experimental variables were changed for this campaign: the compression bank voltage and the number of pulses. The compression bank voltage was varied to change the plasma thermal energy while holding the kinetic energy constant. Varying the number of pulses varies the total particle fluence and thus the total amount of energy deposited to the surface. The experimental parameters for each graphite target tested are shown in Table 5.2.

5.3 Measured Plasma Parameters

As was shown in section 5.1, the properties of particles impacting the solid surface are dependent upon the bulk plasma parameters. Although the Z pinches produced on ZaP-HD have been well characterized, the plasma parameters were closely monitored during the experimental campaign to determine how a solid object in the path of the flowing plasma would

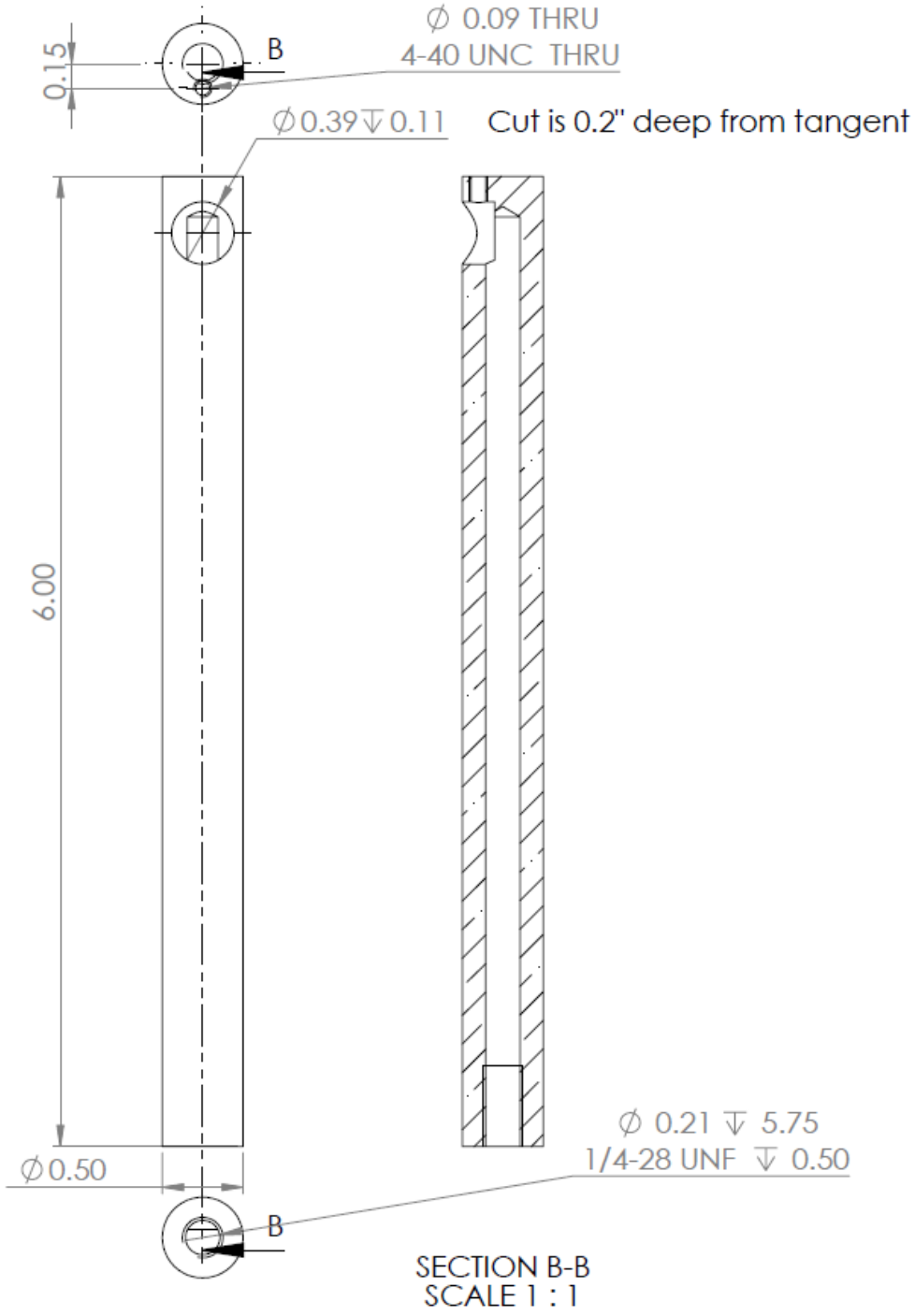

Figure 5.2: A SolidWorks drawing of the boron-nitride mast used to hold PMI targets in the Z pinch. The mast is hollow to allow a thermistor to be inserted behind the target.

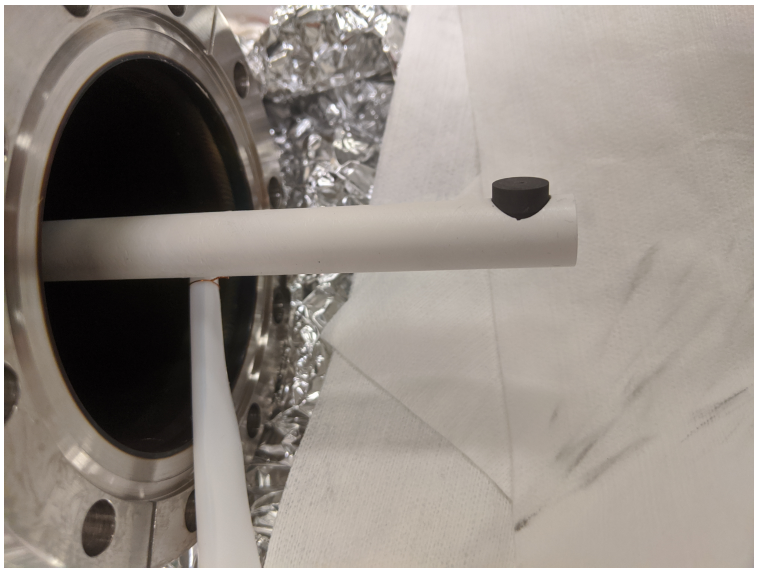

(a)

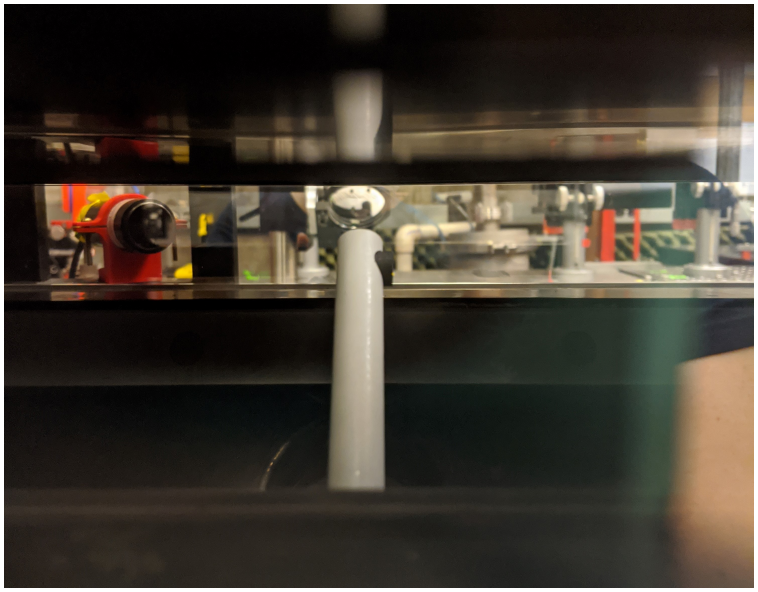

(b)

Figure 5.3: Images of the boron-nitride mast and graphite target. (a) The mast and graphite target outside of the vacuum chamber before the first target exposure. (b) The mast and target fully extended in the vacuum chamber. The target sits approximately 24 cm downstream of the nosecone. Plasma flows from right to left in the image.

	Low Thermal Energy		High Thermal Energy
Low Fluence	9 kV/3 kV, 20 pulses	9 kV/5 kV, 20 pulses	9 kV/7 kV, 20 pulses
	9 kV/3 kV, 40 pulses	9 kV/5 kV, 40 pulses	9 kV/7 kV, 40 pulses
High Fluence	9 kV/3 kV, 60 pulses	9 kV/5 kV, 60 pulses	9 kV/7 kV, 60 pulses

Table 5.2: Parameters for exposing graphite targets to ZaP-HD plasmas.

affect the Z pinch. Measurements from spectroscopy, DHI, fast-framing photography, and magnetic probes provide insight into the plasma behavior when the target and mount block the plasma flow.

Measurements of ion temperature and velocity are shown in Figs. 5.4 and 5.5. Ion Doppler spectroscopy measurements are collected with the ICCD to resolve radiation from the carbon-V impurity line. The split fiber bundle is used to make simultaneous measurements of temperature and velocity. Data are collected at a location 5 cm upstream of the target face. The trigger time for the ICCD is varied to measure the temperature and velocity over the course of the plasma pulse. Each data point represents an average of the measured property within 1 cm of the machine axis. Temperature data are shown in Fig. 5.4. Values computed from the Doppler broadening of carbon-III are shown in black, while values from carbon-V are in red. Each plot is a compilation of 60 plasma pulses with different compression voltages. Figure 5.4a has a compression voltage of 3 kV, Fig. 5.4b 5 kV, and Fig. 5.4c 7 kV. The data show the expected trend of increased ion temperature as the compression bank voltage is increased. For the 3 kV setting, the ion temperature has a small spike early in time of around 400 eV, but falls to around 200 eV for the remainder of the pulse. When the voltage is increased to 7 kV, the carbon-III temperature shows a similar behavior of spiking and dropping, but the temperature computed from carbon-V indicates that the ion temperature continues to increase to over 1 keV over the course of the pinch lifetime. Both the carbon-III and carbon-V measurements were taken simultaneously, with the carbon-III measurements

likely coming from colder plasma not entrained in the pinch.

Velocity measurements are shown in Fig. 5.5 for the three different compression bank settings. The velocity is calculated from the Doppler shift of the carbon-III impurity line. Each data point is an average of the values measured within 1 cm of the machine axis. All three plots exhibit a similar trend in ion velocity over the plasma lifetime. The plasma is moving faster at the beginning of the pulse when current in the acceleration region is high, and decreases with the current over time. The value of the velocity is unaffected by compression voltage; the charge voltages for Figs. 5.5a, 5.5b, and 5.5c are 3 kV, 5 kV, and 7 kV respectively. This affirms the assumption that varying the compression voltage will affect the thermal energy of the plasma hitting the target but not the kinetic energy.

Measuring the plasma ion temperature and velocity is important to determining the energy at which ions will strike the target surface. To determine the ion flux from the plasma to the solid, we require a measure of the plasma density around the target. DHI is positioned to measure the electron density directly in front of the target. A number of characteristic structures seen upstream of the PMI target are shown in Fig. 5.6. The DHI scene beam is aligned such that the right most edge of the hologram is coincident with the edge of the target cylinder and the vertical center of the target is located at the 0 impact parameter, which also coincides with the machine axis. In Fig 5.6a, the density map shows a pinch with a radius of approximately 2 mm impinging on an edge of the target. The density is fairly uniform in z, although slightly higher where the pinch is hitting the solid surface. These data were captured at 52.5 μs, approximately half way through the pinch quiescent period for a 7 kV pulse. Figure 5.6b does not show a pinched structure but rather a stagnated cloud of plasma surrounding the target. The structure looks similar to a normal shock. A discussion of the plasma sound speed and fluid velocity is presented later in this chapter. This image was taken at 55 μs for a 3 kV pulse, after the quiescent period had ended. Figure 5.6c shows some structure but relatively low density everywhere except directly in front of the target face. This high-density cloud around the target can appear with or without a pinch structure upstream. This plot was captured for a 3 kV pulse at 55 μs, before the end of the quiescent

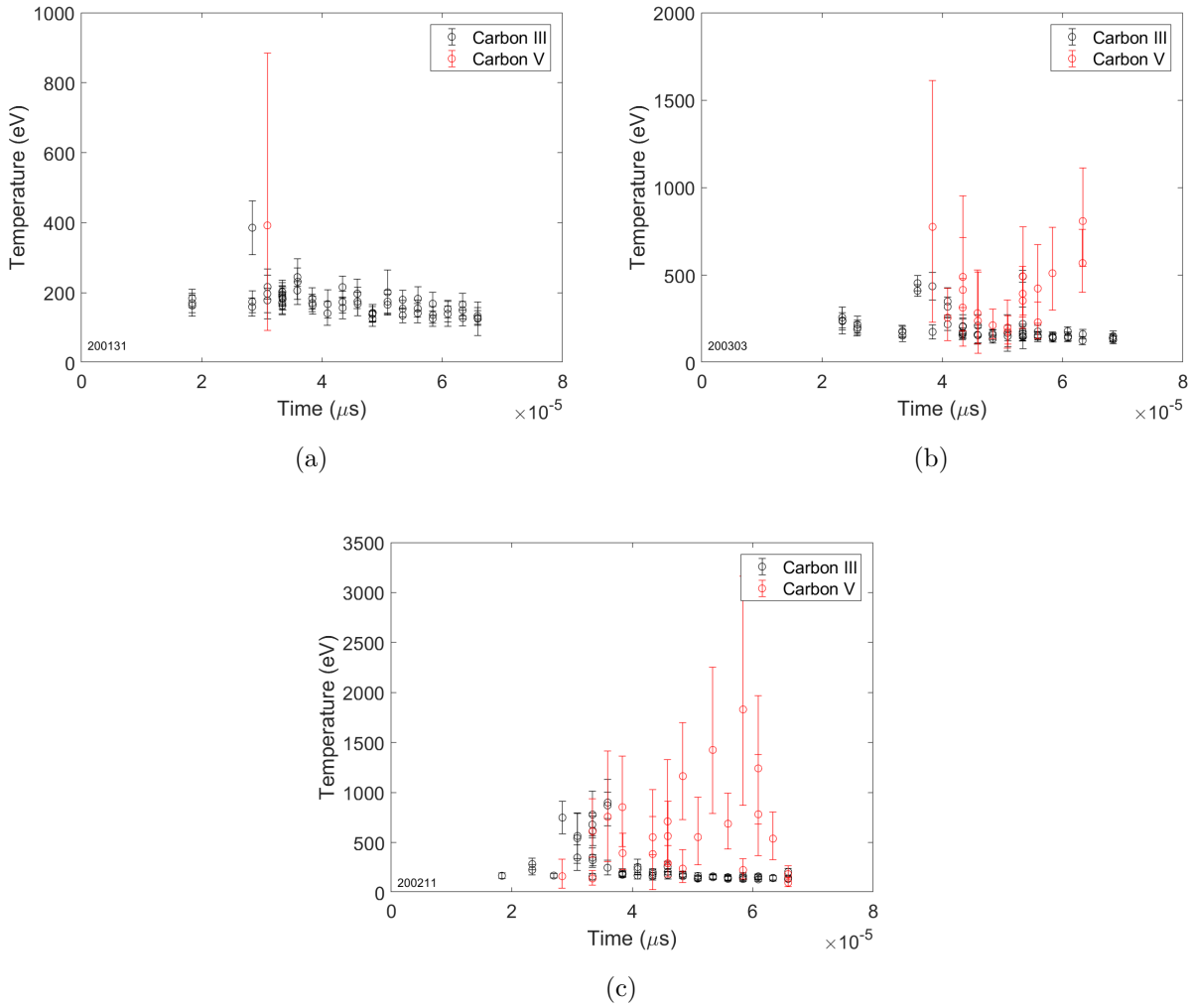

(a) (b) (c)

Figure 5.4: Plasma ion temperature measured upstream of the target. Each temperature measurement is the average temperature within 1 cm of the machine axis at a location 5 cm upstream of the target face. Values are computed from the Doppler broadening of the carbon-III and carbon-V lines. The compression voltage was set to (a) 3 kV, (b) 5 kV, (c) 7 kV to vary the ion temperature. Ion temperature in (a) remains constant at approximately 200 eV throughout the pulse, while (b) and (c) show more peaked profiles with temperatures between 500 and 1000 eV for (b) and 1000 to 2000 eV for (c).

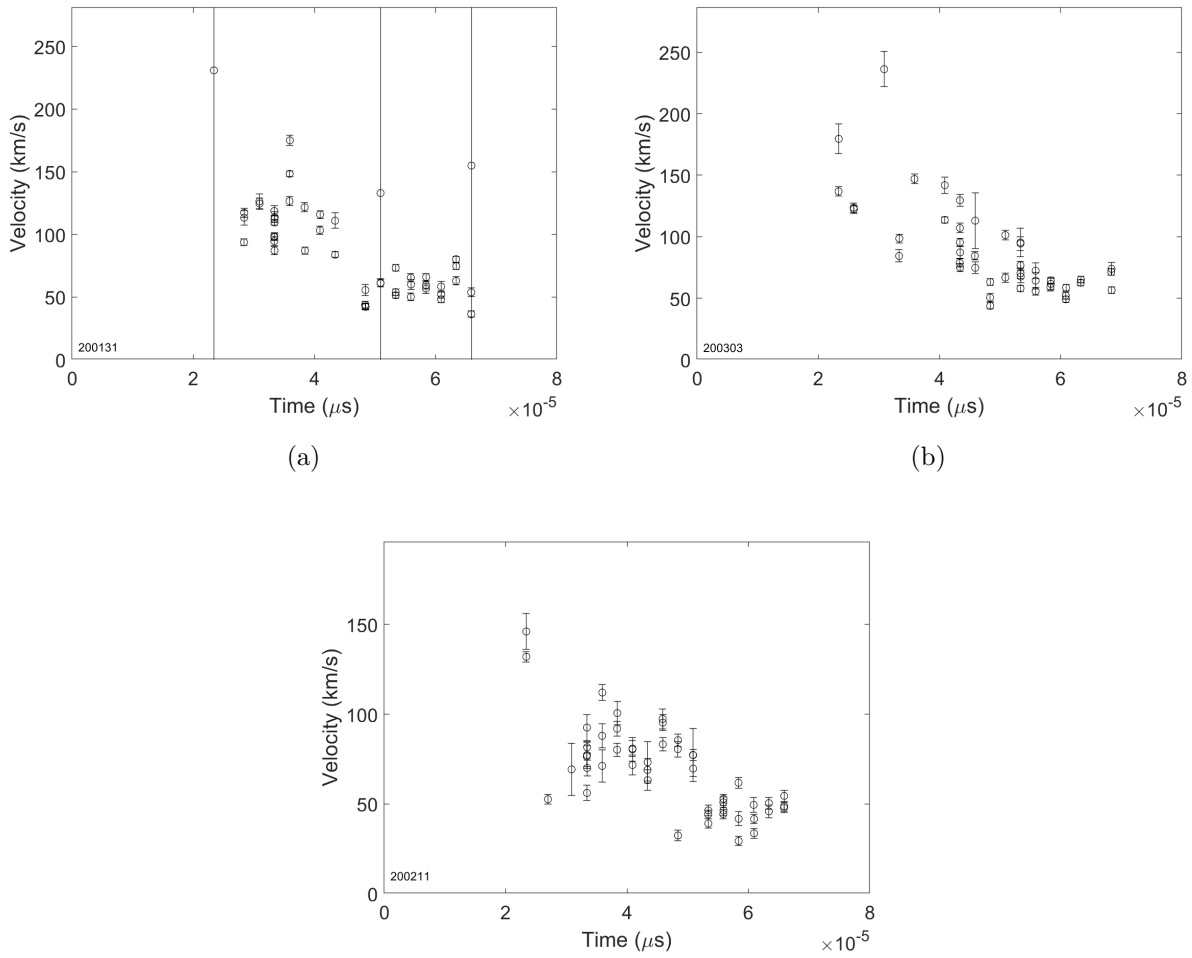

Figure 5.5: Ion velocity measured upstream of the target. The velocity measurements are also an average of the measured values within 1 cm of the machine axis. Values are computed from the Doppler shift of the carbon-III line. Velocity is computed for three compression voltages, (a) 3 kV, (b) 5 kV, and (c) 7 kV. The plasma velocity is relatively insensitive to compression voltage.

period. The average density measured for pulses of all compression voltages was on the order of 2×10^{23} m^{-3}.

In addition to DHI, the plasma structure is also imaged with the Kirana camera. The camera records visible radiation through the rectangular window at an angle such that the camera is looking slightly upstream at the target. The camera cannot be placed perfectly perpendicular to the rectangular window due to the location of the DHI optical towers. This view of the target slightly compresses the axial structure seen in the video. A still from a 3 kV pulse is shown in Fig. 5.7. The image is shown in false color to make the structures easier to see. The testing apparatus, which includes the boron-nitride mast and graphite target, are visible on the left-hand side of the image. The flat face of the target is pointing away from the camera, towards the impinging plasma. Upstream of the target, a collimated plasma structure extends for the length of the assembly region imaged by the Kirana. This structure is much more dim than the plasma surrounding the target, where it appears stagnation has begun to occur. Energetic ions will radiate at higher wavelengths, and therefore might not be captured by the Kirana, which can only image in the visible range without the ultraviolet intensifier. The bright cloud surrounding the target could be colder plasma, or hot neutral atoms which have been sputtered or re-emitted from the testing apparatus.

The Kirana images a similar variety of structure to the data recorded by DHI. Figure 5.8 shows a close-up of the BN mast and target during a pulse. Light emitted by the plasma is shown in false color. Plasma appears to have stagnated around the target and mast, with no structure visible upstream of the apparatus in the original full size image. The thin structure seen just in front of the target has a similar shape to the data shown in Fig. 5.6b. The structure is normal to the direction of plasma flow and appears to span beyond the 5 cm height of the rectangular window. In the video, structures such as these are transient; they appear briefly before becoming distorted and flowing downstream.

Plasma structure seen in the Kirana videos can be compared to data taken simultaneously with digital holographic interferometry. Figure 5.9 shows a frame from a Kirana video with the density contours measured by DHI overlaid on the image. The DHI profile has been com-

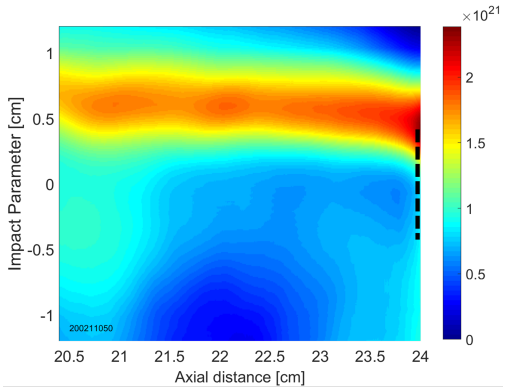

(a) Electron density (m^{-3}).

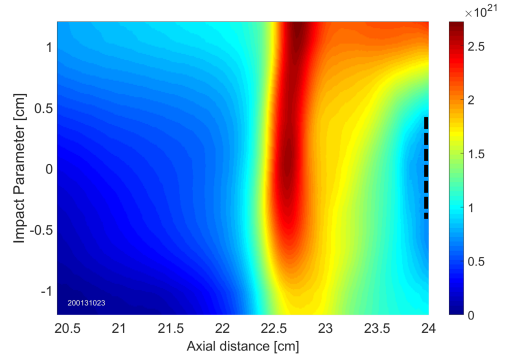

(b) Electron density (m^{-3}).

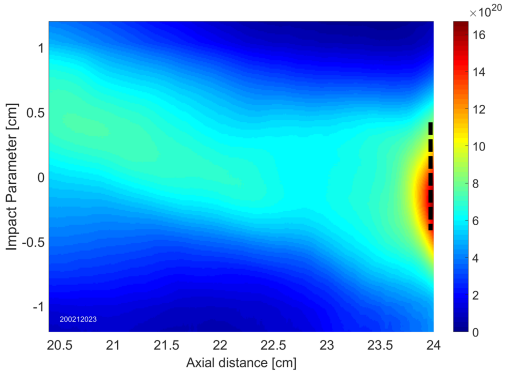

(c) Electron density (m^{-3}).

Figure 5.6: Several characteristic structures seen in line-integrated density data in front of the PMI target. (a) A collimated pinch with little axial variation in line-integrated density. (b) A stagnated layer of plasma surrounding the target surface. (c) Relatively low density except for immediately in front of the target face. The black dashed line indicates approximately the target diameter. The face of the target is located at the right edge of the density map.

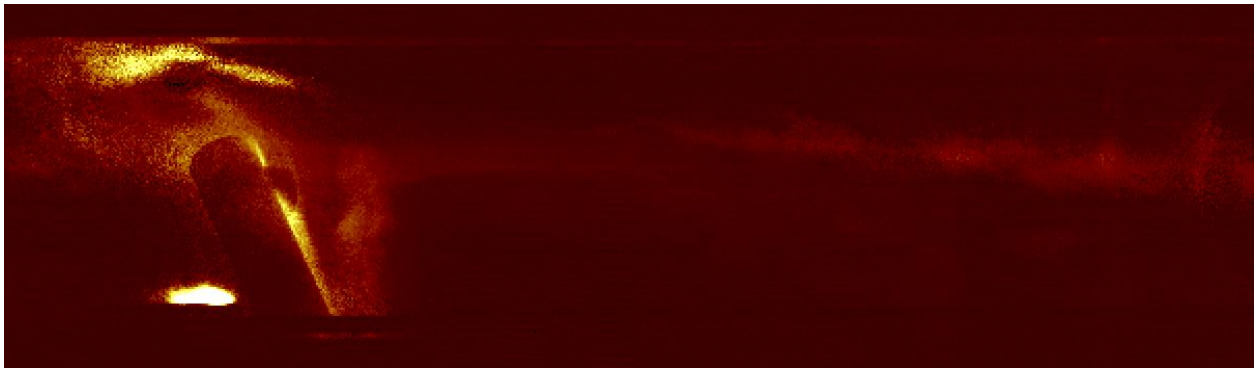

Figure 5.7: A false color frame from a Kirana video. The boron-nitride mast and graphite target are outlined by radiation from the plasma on the left hand side of the image. Plasma flows from right to left. A plasma column is visible upstream of the testing apparatus. The plasma appears to have stagnated around the target. The Kirana is angled slightly upstream to view the span of the assembly region from the nosecone to slightly downstream of the target, a distance of approximately 30 cm.

pressed axially to match the camera viewing angle. Dotted white lines indicate the outline of the mast, while dotted green lines roughly show the outline of the target. The brightest part of the image is the boron-nitride mast. Radiation from this area could be stagnated plasma or sputtered neutrals. Upstream of the target, a dim structure similar in shape to the DHI measurement is visible. Both the Kirana and DHI data indicate a pinch structure with a radius of less than 5 mm impinging on the center of the target. Visible radiation in the Kirana videos does not always correspond to structure seen in the DHI density contour plots. Data from the Kirana can provide a qualitative picture of the behavior of radiating ions and neutrals, but understanding quantitative aspects of the recorded structure requires additional diagnostics, such as DHI or spectroscopy.

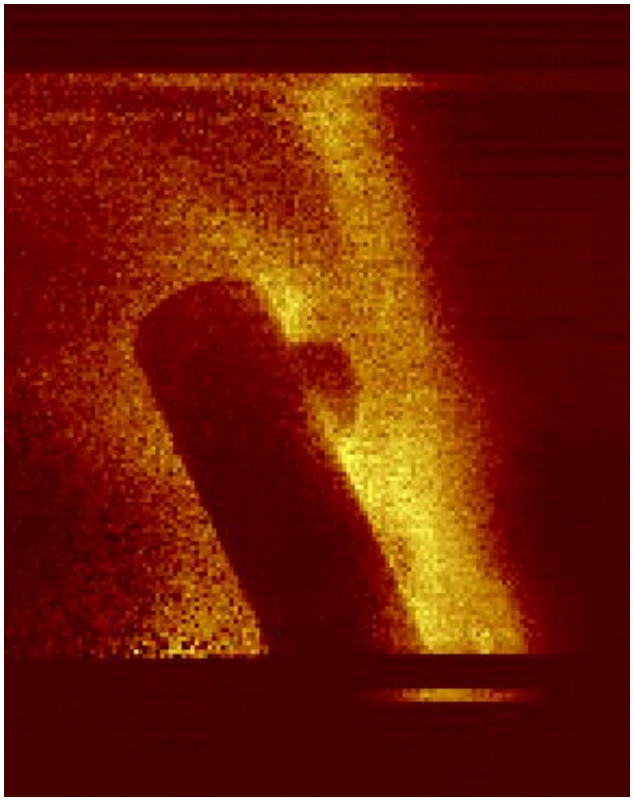

Figure 5.8: A close-up of the target and mast surrounded by plasma. The bright structure in front of the target is a similar shape to the structure seen in the DHI data in Fig. 5.6b.

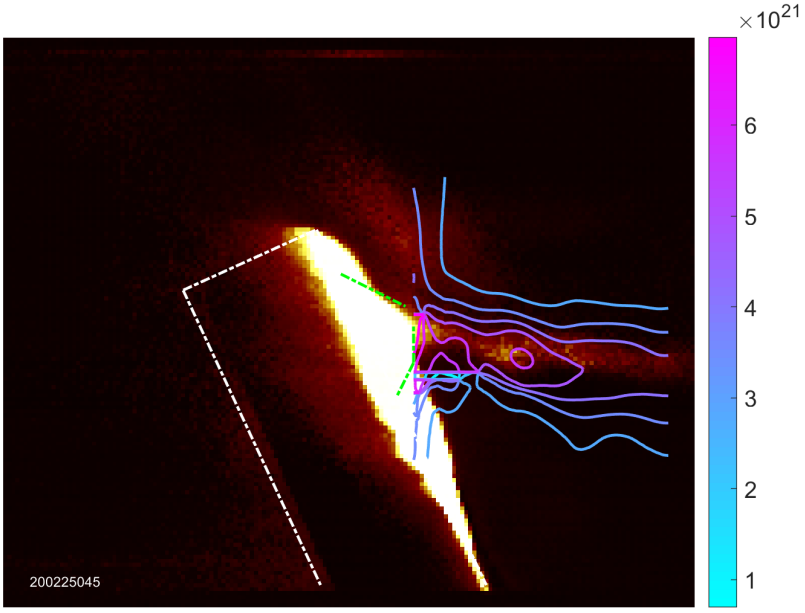

Figure 5.9: A false-color still from a Kirana video with a density contour overlay. In this frame, the brightest radiation comes from the plasma hitting the solid target. The density structure recorded by DHI corresponds to much less intense radiation from the plasma upstream of the target. A white outline indicates the back of the boron-nitride mast and the edge of the graphite target is shown roughly with green dotted lines.

5.4 Qualitative Results from Micrographs

Analysis of the target surface required the student resources available at the UW Material Analysis Facility (MAF). Target surfaces are imaged with an FEI Sirion scanning electron microscope (SEM). Surface composition can be analyzed with an attached energy dispersive X-ray spectrometer (EDS). The tool provides an easy method to perform surface mapping and elemental analysis at the same time.

Scanning electron microscopes produce images of a sample surface by scanning a specimen with a focused beam of electrons. The Sirion SEM can collect both secondary and back scattered electrons. Secondary electrons are sensitive to the surface topography, while back scattered electrons are dependent upon material Z and help contrast differences in materials. SEM is a technique that requires a conductive sample, otherwise charge accumulation can blur and distort the image. The FEI Sirion XL30 has a resolution of 1.5 nm and a magnification of up to 800 kX.

Energy-dispersive X-ray spectroscopy is used to analyze the elemental composition of a sample. A beam of X-rays of specified energy is focused on the target surface, and the resulting X-rays emitted by the specimen are measured with an energy-dispersive spectrometer. The composition of the sample is determined by analyzing the relative intensities of the emitted X-rays. The Sirion EDS automatically identifies the composition based on the measured spectra and provides a quantitative analysis of the data. Depending on the X-ray beam energy, elements with as few as six electrons (carbon) can be identified.

To monitor surface deformation due to plasma exposure, the SEM is used to capture micrographs of the target before and after exposure to plasma. For this analysis, the "top" of the target will refer to the flat face of the cylinder that sits normal to the plasma flow, while the "side" will indicate the curved surface oriented parallel to the direction of plasma flow. Micrographs of both the top and side are studied before and after plasma exposure to understand the effects of the plasma flow on surface deformation.

Images from the tops of targets exposed to plasmas with a 3 kV compression bank volt-

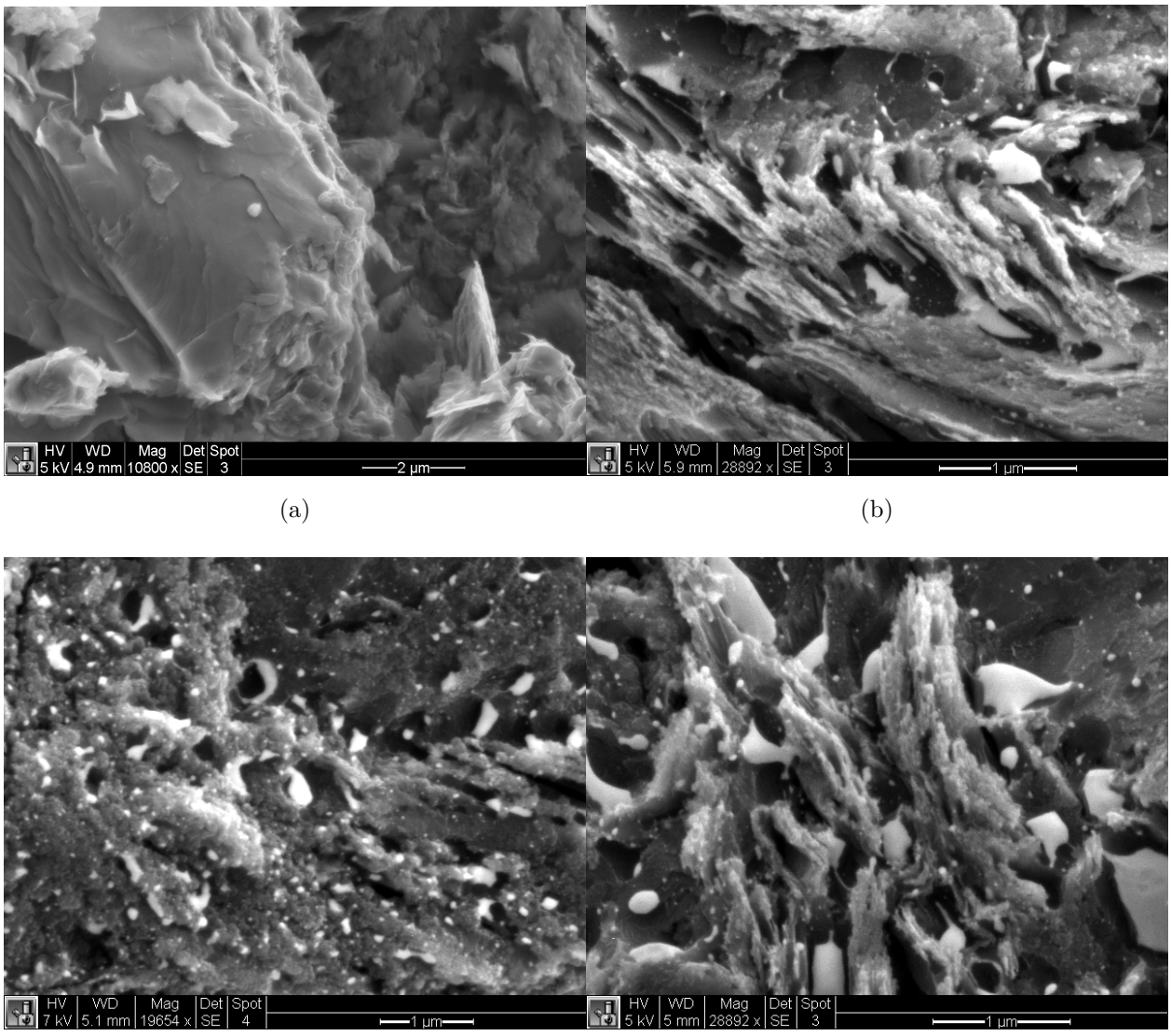

(a) (b)

(c) (d)

Figure 5.10: Micrographs of graphite targets exposed to 3 kV plasma pulses. All micrographs are from the face oriented normal to the plasma flow. (a) A control image before plasma exposure. Targets were exposed for 20 (b), 40 (c), and 60 (d) pulses. The smooth, white, bulbous structures visible in (b) – (d) are melted tungsten.

age are shown in Fig. 5.10. The control surface is shown in Fig. 5.10a. The targets were manufactured on a lathe and while the surface appears smooth at low magnification, a closer look reveals some sharp edges and uneven surface height likely due to the scraping of the lathe bit to remove material. A scale is located in the bottom right hand corner of each image. The three micrographs in Figs. 5.10b, 5.10c, and 5.10d show the target surface after exposure to 20, 40, and 60 pulses respectively. Even after 20 pulses, the surface has been significantly deformed from the original image. Crystal-like striations appear in all three images. The structures appear to be larger in the 60 pulse image. A white substance seen on all three samples is determined to be tungsten by EDS. The tungsten beads appear to have caused damage to the surface. Craters can be seen near larger droplets, particularly in Fig. 5.10c where the tungsten appears to be most evenly distributed. The metal likely originated from the cathode nosecone, which was originally tungsten-sprayed copper. The nosecone tip has been melted significantly since installation and is now bare copper within approximately 2 cm of the tip. The surface composition for all samples is approximately 2% tungsten, indicating the deposition was insensitive to the compression charge voltage.

Structures seen on the target face normal to the flow were significantly different to those found on the parallel face. Figure 5.11 shows micrographs of the target side before exposure (Fig. 5.11a) and after 20, 40, and 60 pulses in Figs. 5.11b, 5.11c, and 5.11d respectively. The control surface is slightly flatter than the surface in Fig. 5.10a because it was extruded rather than turned down on the lathe. The post-plasma exposure images show signs of melting, particularly in the 20 and 60 pulse images. Melted material congeals into droplets, which solidify as the sample cools. Under conditions at standard pressure, graphite will sublimate once it is heated beyond 3900 K. Graphite will only melt at 4000 K if the pressure exceeds 110 atmospheres. The magnetic field required to balance this pressure is approximately 5 T. Using the measured electron density and assuming $n_i = n_e$, the thermal pressure will exceed 110 atm if the temperature is greater than 350 eV, a threshold exceeded by even the low-energy pulses. The sharp crystal striations seen on the front face of the targets are not present in these samples.

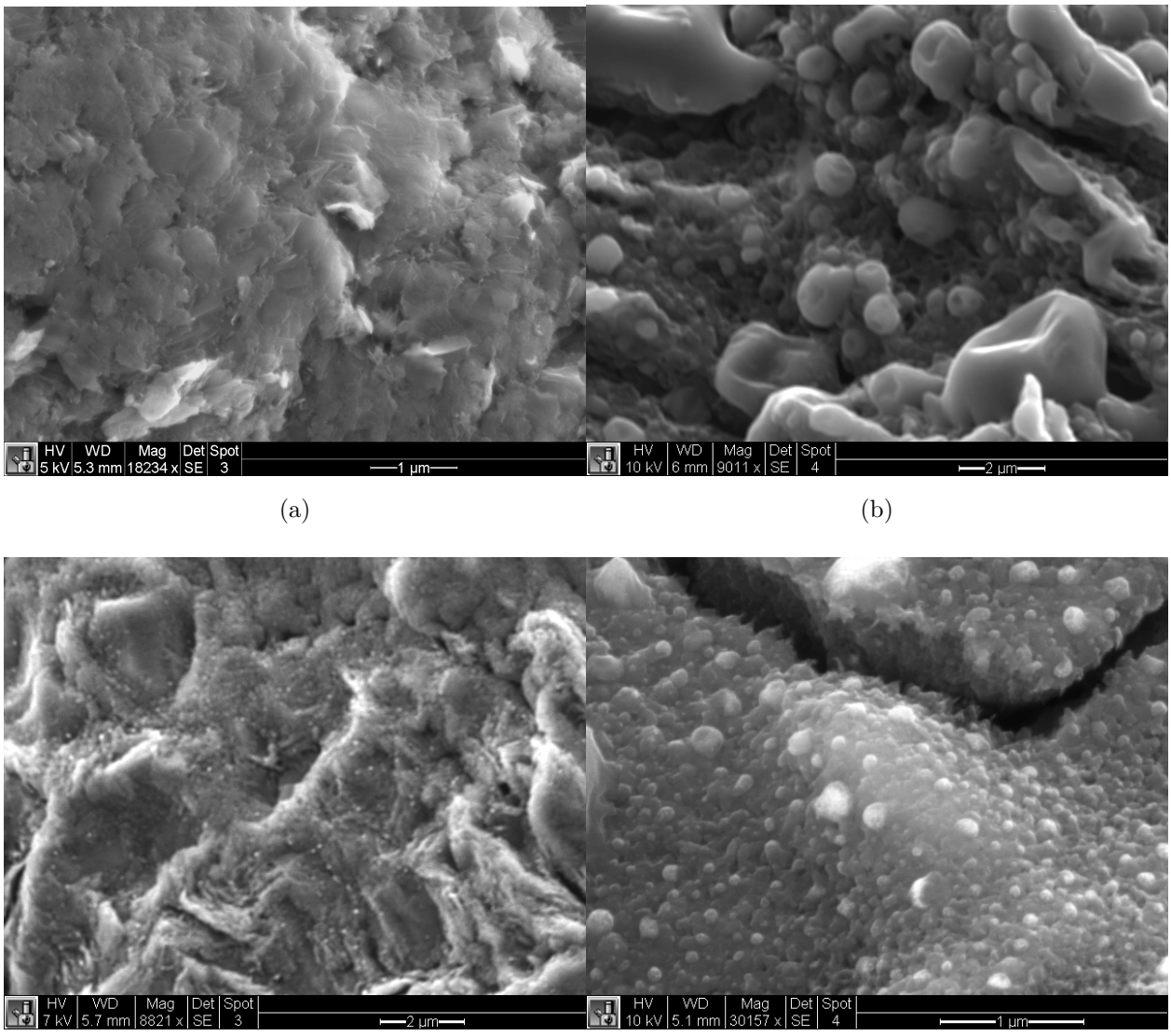

(a) (b)

(c) (d)

Figure 5.11: Micrographs of target sides after exposure to 3 kV plasma pulses. (a) The surface of a target side before plasma exposure. Images show targets after 20 (b), 40 (c), and 60 (d) plasma pulses. Contrast for these images shows only surface features, EDS showed no evidence of tungsten contamination.

The surface topography of samples exposed to plasma pulses with a 7 kV compression bank charge voltage, and therefore higher ion temperatures, is shown in Fig. 5.12. The unexposed target top is shown again for reference, followed by the target tops exposed for 20 (Fig. 5.12b), 40 (Fig. 5.12c), and 60 (Fig. 5.12d) pulses. All three exposed surfaces show evidence of tungsten sputtering, much like the targets exposed to lower temperature plasmas. However, the sharp-edged ridges seen in the low-temperature samples are missing. Instead, it appears that the surface is flattened as the number of exposures is increased. There is some evidence of the droplets seen on the sides of targets exposed to lower-temperature plasmas, particularly in Fig. 5.12c. This could indicate that the tops of these targets are undergoing similar PMI processes as the sides of the targets exposed to lower-temperature plasmas. We might expect thermal processes to dominate for both the tops and sides of the targets exposed to high-temperature plasmas, as the thermal energy of the plasma in this case is much larger than the kinetic energy.

Micrographs of the sides of targets exposed to plasmas generated with a 7 kV compression bank charge are shown in Fig. 5.13. The control image of the target side is again shown in Fig. 5.13a, and the 20, 40, and 60 pulse targets in Figs. 5.13b through 5.13d respectively. The structure seen on these targets is very similar to the target sides in the lower voltage cases. Small droplet-like structures have formed across the entire target surface. As the number of exposures is increased, the droplets become less distinct and look more like a singular, lumpy mass. This could be the result of increased melting with increased total ion fluence.

A limited amount of data was collected on targets made from boron-nitride. Boron-nitride targets were machined from an AX05-grade rod on a lathe and had the same dimensions as the graphite targets. The targets were tested for four cases: 3 kV compression and 20 pulses, 3 kV compression and 60 pulses, 7 kV compression and 20 pulses, and 7 kV compression and 60 pulses. Micrographs of the target tops were collected on a TFS Apero-S scanning electron microscope and are presented in Fig. 5.14. This microscope is better at resolving images of insulating materials, although collecting clear images of the BN is still challenging.

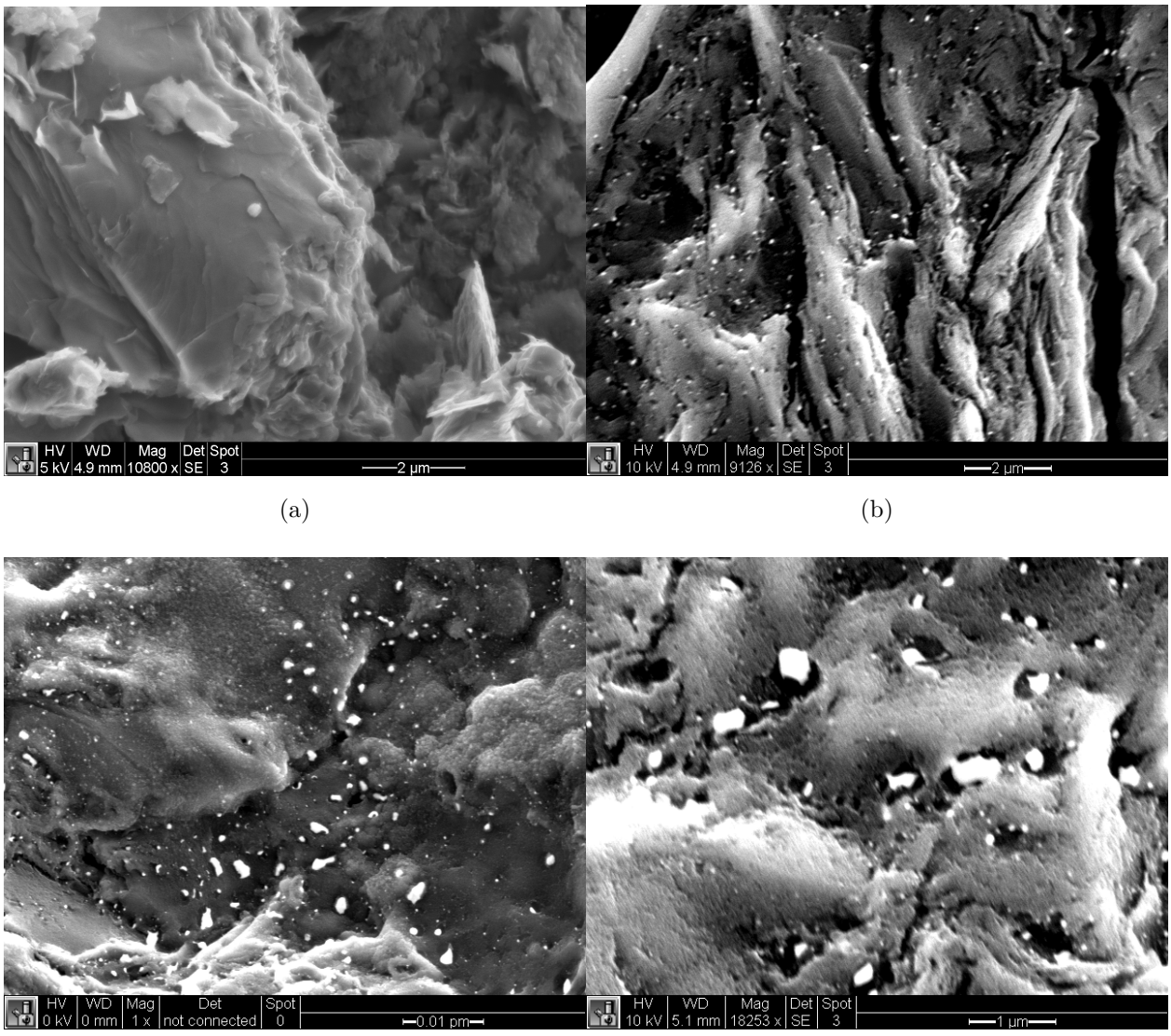

(a) (b)

(c) (d)

Figure 5.12: Micrographs of target tops after exposure to 7 kV plasma pulses. (a) The control image, shown again for reference. Images show targets after 20 (b), 40 (c), and 60 (d) plasma pulses. Tungsten droplets are again seen on every plasma-exposed surface, although smaller and more evenly distributed for (b) and (c). The scale for (c) should read 2 μm.

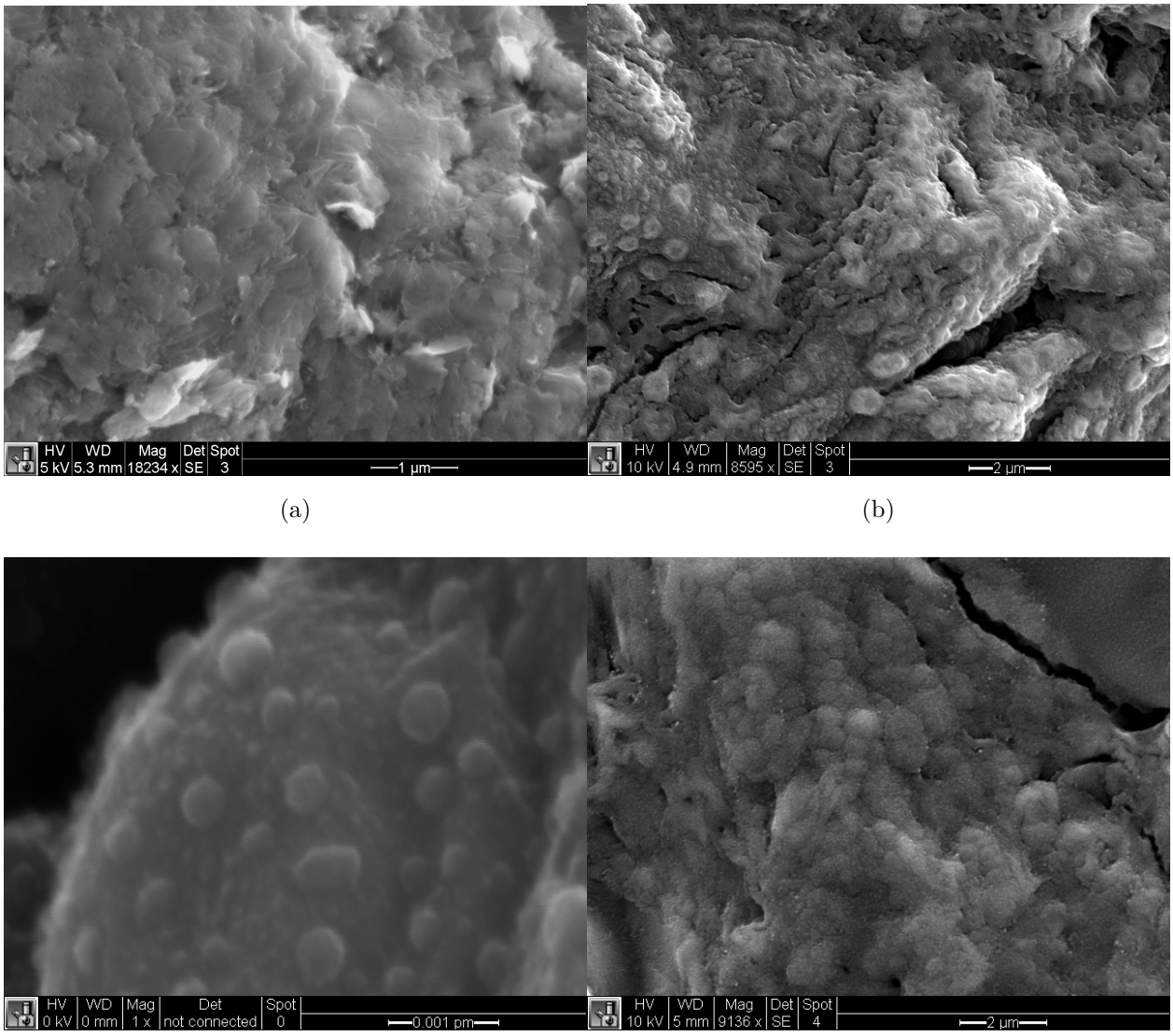

(a) (b)

(c) (d)

Figure 5.13: Micrographs of target sides after exposure to 7 kV plasma pulses. (a) The control image, shown again for reference. Images show targets after 20 (b), 40 (c), and 60 (d) plasma pulses. All three targets show evidence of droplet formation from melting, and look similar to the target sides from the 3 kV plasma pulses. The scale for (c) is 500 nm. Header information has been lost from the .tif file.

The control surface of the BN target top is shown in Fig. 5.14a. Figures 5.14b and 5.14c show target tops after 20 and 60 exposures to plasmas with a 3 kV compression voltage. Figure 5.14d shows the surface of a target that has been exposed to 60 pulses with a 7 kV compression voltage. Qualitatively, the surfaces appear to have undergone similar changes despite varying the ion fluence and temperature between the samples. All three show signs of melting and erosion, but do not exhibit the cratering or striations visible on some of the graphite targets. There does not appear to be tungsten contamination on these samples, although the EDS tool was not used to analyze the surface composition of these targets.

Micrographs of the surfaces of targets taken before and after exposure to plasma reveal a variety of processes occurring on the target surfaces. Graphite targets exposed to low-temperature plasma show sharp crystal structures on the face normal to the plasma flow, but amorphous melting on faces parallel to the plasma flow. High-temperature plasma interactions with graphite produced much smoother surfaces on the normal face and melting similar to the low-temperature targets on the sides. For boron-nitride targets, it was difficult to discern differences between targets exposed to varying plasma temperatures and ion fluences. The next section will quantify some of the features seen in the micrographs and correlate the target surface topography to plasma parameters.

5.5 Correlating Plasma Parameters and PMI Phenomena

5.5.1 Heat Deposition

The interplay between the plasma parameters and the processes affecting the solid target is extremely complex. Plasma ion temperature, density, and stability evolve rapidly in time, exposing the target to transient events that may not be accounted for by steady-state analysis. However, in order to calculate quantities relevant to the plasma-material system, the behavior will be approximated as steady-state and incorporate time-resolved data wherever possible. The quantitative data presented provide upper and lower bounds for parameters encountered by the target.

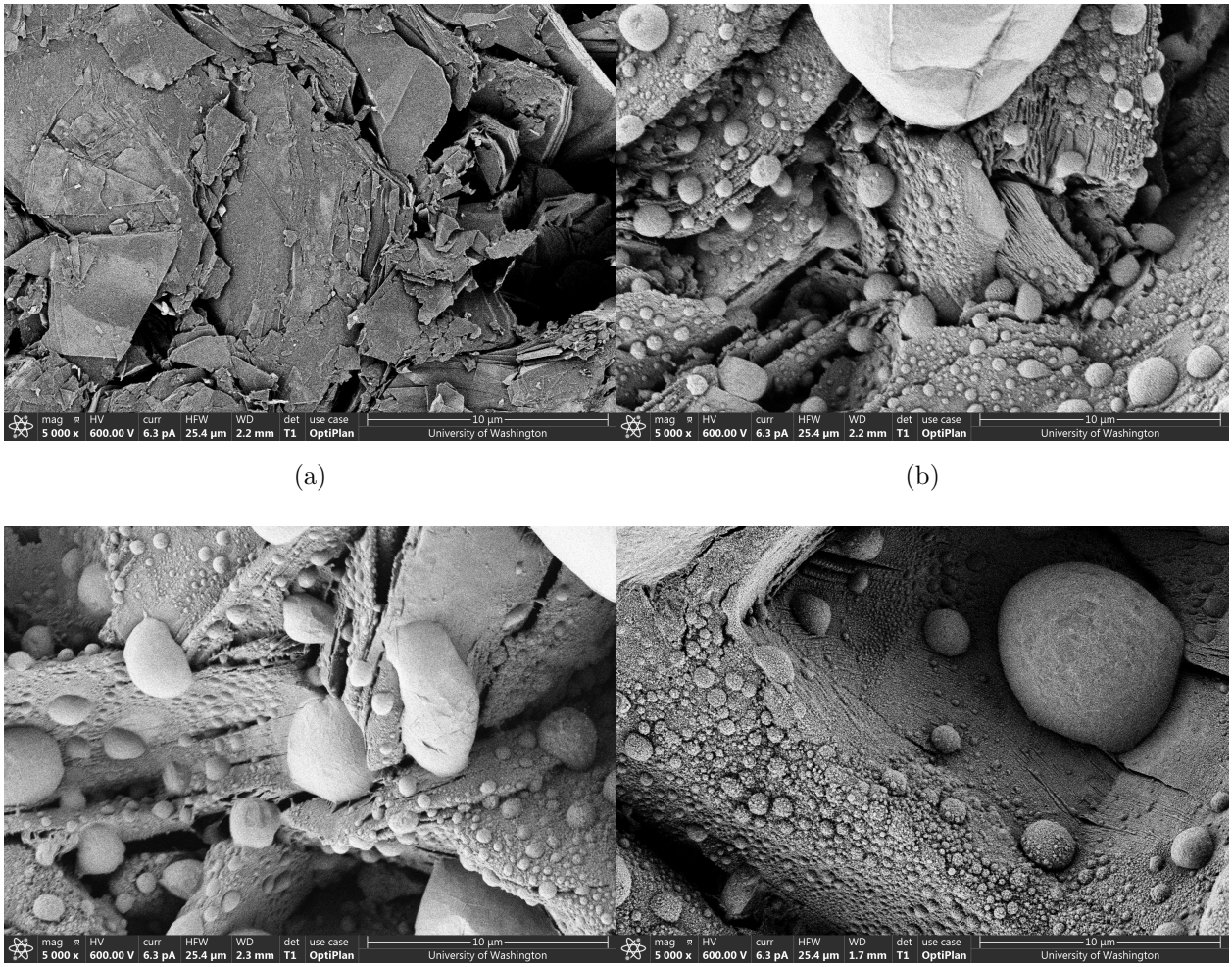

(a) (b)

(c) (d)

Figure 5.14: Micrographs of boron-nitride targets before and after exposure to plasma. (a) The normal face of a boron-nitride surface before plasma exposure. (b) A target top exposed to 20 pulses with a 3 kV compression bank voltage. (c) A target top after 60 pulses with 3 kV compression. (d) A target top after 60 pulses with 7 kV compression.

Data from Section 5.3 can be used to calculate the properties described in Section 5.1 that are important to understanding PMI phenomena. Calculating quantities such as the ion sound speed and particle flux requires several assumptions. To calculate the sound speed, the average temperature at each point in time is used. If temperature is found from both carbon-III and carbon-V, the average of the two values is used. This assumes equal populations in both temperature states, which may not accurately represent the distribution. The sound speed calculated from the average of the carbon-III and carbon-V measurements can be thought of as an upper bound. Using spectroscopy data, the sound speed is calculated with Eqn. 5.4, assuming $\gamma = 1$ and $T_i = T_e$. Plots of the calculated sound speed are shown in Fig. 5.15. Figure 5.15a shows the sound speed calculated for the low-temperature setting, with a 3 kV compression bank charge voltage. As expected, the sound speed tracks with the shape of the temperature evolution, remaining relatively constant throughout the pulse. It is interesting to note that ion velocity measured with spectroscopy is on the order of the calculated sound speed for this setting between 25 and 35 μs. Sound speed for the high-temperature, 7 kV compression bank pulse is shown in Fig. 5.15b. Here, the sound speed starts around the same value as seen in the low-temperature plasma, but quickly increases to approximately 300 km/s. Measured velocities for this pulse series are much lower than the sound speed.

To calculate the heat deposition from plasma parameters, the particle flux is first calculated from DHI density measurements and computed sound speed. The average density near the target for all initial conditions is found to be 2×10^{23} m^{-3}. This assumes that the plasma column has a flat density profile and a diameter of 1 cm, and that the ion and electron densities are equal. As was shown in the Theory section, the heat flux to the surface can be calculated in a variety of ways. Without including the magnetic field, the particle flux to the surface is found to be $10^{28} - 10^{29}$ m^{-2}s^{-1}. Using Eqn. 5.11, the particle flux is calculated to be $10^{27} - 10^{28}$ m^{-2}s^{-1}, an order of magnitude smaller. The floating potential of the target is then calculated from Eqn. 5.7 and heat flux to the solid surface from the ions and electrons is found from Eqns. 5.8 and 5.9, using the reduced coefficient from Bissel and

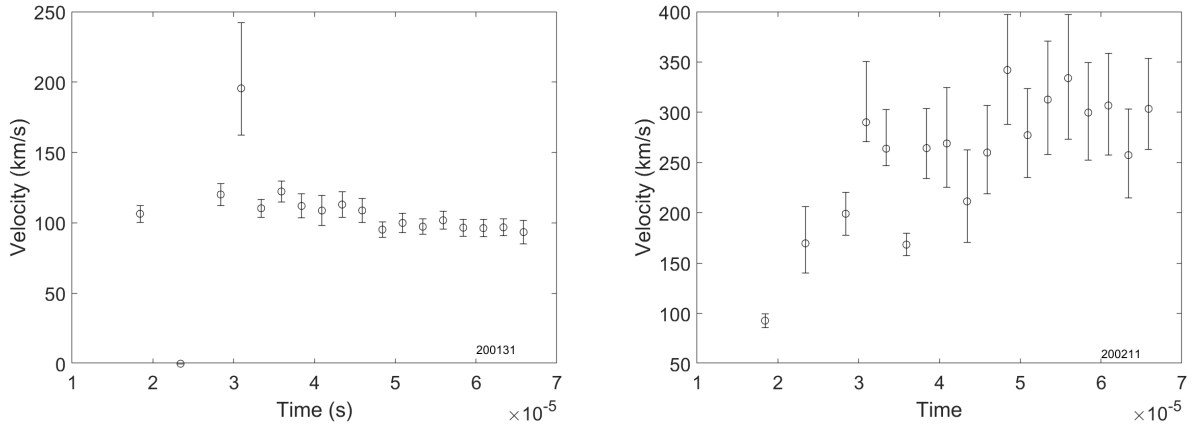

(a) (b)

Figure 5.15: Sound speed calculated for low- and high-temperature plasmas. (a) The sound speed calculated for a plasma with 3 kV compression bank voltage, almost exclusively from carbon-III measurements. (b) Sound speed calculated for a plasma with 7 kV compression bank charge voltage, an average of measurements from carbon-III and carbon-V.

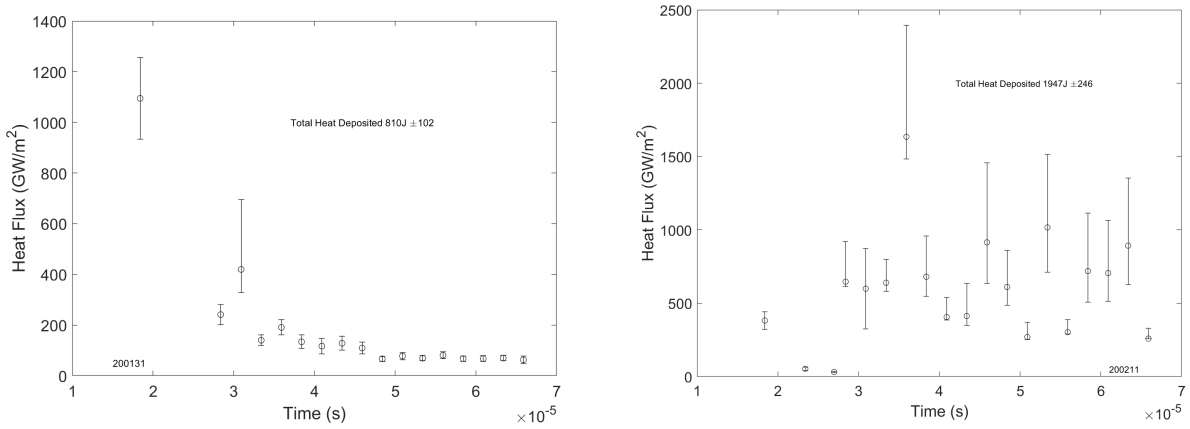

(a) (b)

Figure 5.16: Heat flux calculated for low- and high-temperature plasmas. (a) The heat flux calculated for a plasma with 3 kV compression bank voltage. (b) The heat flux calculated for a plasma with 7 kV compression bank charge voltage. The total deposited heat is calculated for the target surface area and printed on the plots. Heat fluxes are extremely high, but the duration is on the order of tens of microseconds.

Johnson. The time-resolved heat flux using the particle flux perpendicular to the magnetic field is calculated and plotted in Fig. 5.16. Heat flux for the low temperature plasma formed with a 3 kV compression bank charge voltage is plotted in Fig. 5.16a and for the high-temperature, 7 kV compression bank voltage plasma in Fig. 5.16b. The heat flux for the lower-temperature plasma varies between 100 to 400 GW/m^2, while the high temperature setting shows between 500 and 1000 GW/m^2. The latter heat flux is roughly equivalent to an electron beam welding torch [4]. However, these values correspond to a heat flux on the order of 10 to 100 MW over the cross-sectional area of the pinch.

The total heat deposited to the target per pulse is calculated by integrating under the heat flux curve and multiplying that value by the area of the target. The total heat to the front face of the target and standard deviation is printed on each plot. Total heat deposited

from the lower-temperature plasma is 0.8 kJ, while the higher-temperature plasma deposited 1.9 kJ. This assumes that the plasma density is constant and the plasma well-centered over the course of the entire pulse. The total heat can be compared to the energy stored in the capacitor banks. The total energy stored in the capacitor banks is $E_B = \frac{1}{2}\left(C_A V_A^2 + C_C V_C^2\right)$ where the subscript A denotes the acceleration bank and C the compression bank. Both capacitor banks have a capacitance of 680 μF. For the lower compression voltage, the total bank energy is 30.6 kJ. For the higher compression voltage, the total energy is 44.2 kJ. This means that roughly 2.6% of the bank energy would be deposited to the target for the lower charge voltage and 4.2% for the higher bank energy. In addition, data from experimental campaigns with identical parameters but boron-nitride targets yield similar results. The heat deposited per pulse for the 3 kV compression voltage plasma was calculated to be 0.5 kJ, and 1.9 kJ for the 7 kV compression voltage setting. Inserting the target into the path of the pinch creates a chaotic environment where the temperature, density, and magnetic field can fluctuate rapidly. Estimating the density as constant will tend to overestimate the number of particles hitting the target surface. However, assuming the magnetic field is parallel to the target face will tend to underestimate the particle flux. While these assumptions oversimplify the dynamics of the system, they are necessary to extract quantitative information about the interactions between the plasma and the targets.

The heat flux to the target sides can also be approximated using the perpendicular diffusion coefficient. Approximating the density around the sides of the target to be uniform, the equation to find the magnetic field strength on the side of the target is

$$\frac{B_2}{B_1} = \frac{n_2}{n_1}. \tag{5.13}$$

The density around the sides of the target is estimated to be approximately half of the density in front of the target. Spectroscopic measurements are used to calculate the heat flux with Eqn. 5.11. The total deposited heat to the target side is found to be 0.6 kJ for the low-temperature case and 1.4 kJ for the high-temperature case. This brings the total deposited heat to roughly 4.6% and 7.4% of the total capacitor bank energy respectively.

The use of the cross-field diffusion coefficient requires the assumption that the magnetic field does not penetrate the target. Graphite has a relatively high conductivity, but boron-nitride is an insulator. The diffusion time of the magnetic field into a material can be calculated using a dimension of the material and the resistivity,

$$\tau = \frac{\mu_0 L^2}{\eta}. \tag{5.14}$$

Using the length of the cylinder as the characteristic length, the magnetic field will soak into the graphite target within 2.5 μs, and will essentially instantaneously penetrate the boron-nitride target. However, if any plasma stagnates around the target, this stagnated plasma will act to oppose the magnetic field from the bulk plasma. Image currents generated in the stagnated plasma will shield the target from the magnetic field generated by the pinch. To calculate the soak-in time for a stagnated plasma layer, the Spitzer resistivity of the plasma is calculated from

$$\eta_S = \frac{4\sqrt{2\pi}}{3} \frac{Ze^2 m_e^{1/2} ln\Lambda}{(4\pi\epsilon_0)^2 (k_B T_e)^{3/2}}. \tag{5.15}$$

An average temperature is found for each set of initial conditions to compute the resistivity. For the low-energy case, the average temperature is 330 eV and the resistivity is calculated to be 2.8×10^{-7} Ω-m. The high-energy case has an average temperature of 950 eV and resistivity 5.0×10^{-8} Ω-m. The thickness of the stagnated layer around the entire target cannot be directly measured, but can be estimated from the thickness of the high-density region in front of the target measured by DHI. The thickness of this region is not constant, but a range of values can be used to calculate the expected soak-in time for different plasma parameters. In general, the stagnated layer appears to be between 0.1 and 1 cm thick. The computed soak-in times for the two cases presented are 5.3 to 530 μs for the 330 eV case and 25 μs to 0.25 ms for the 950 eV case. These characteristic length scales, particularly for the high-temperature case, indicate that it is plausible that the stagnated plasma effectively shields the target from the magnetic field for the length of the pulse.

An angle of incidence can be incorporated into the energy analysis for the non-magnetized case, which would reduce the calculated heat flux without assuming a magnetic field profile.

If the flux is incident at an angle α to the surface, the particle flux to the surface will be

$$\Gamma_{\perp} = \Gamma_{\parallel} sin\alpha \tag{5.16}$$

A plot of the heat flux as a function of this angle for the high and low charge voltage cases is shown in Fig. 5.17. The total calculated heat deposition per pulse is plotted for both the 3 kV and 7 kV compression voltage cases. For the high-temperature plasma, an angle of incidence greater than 34° will result in enough energy being deposited to sublimate the entire target. This analysis is particularly relevant for the target sides, where the plasma flow is parallel or nearly parallel to the surface. An incidence angle of less than 3° will yield a heat deposition less than 0.16 kJ for the low-temperature plasma and less than 1.0 kJ for the high temperature plasma. This limited particle flux could explain in part the difference in surface geometry seen on the front and side of each target.

The thermistor at the back of the target provides another method for estimating the heat deposited to the target per pulse. Though the diagnostic cannot measure the change in temperature during the pulse, it can provide a measure of the temperature before and after each plasma exposure. Monitoring this change in temperature and assuming no heat is radiated by the target before the final temperature is recorded, the heat deposited to the target can be written as

$$h = c\Delta T \tag{5.17}$$

where c is the heat capacity of the material in J/g-K. Multiplying h by the target density and volume yields the total energy deposited from the plasma to the target. Assuming the energy is deposited in the first half cycle of the capacitor bank discharge, the power can be calculated by dividing the heat by the pulse time and target surface area,

$$\dot{Q} = \frac{H}{\tau A}. \tag{5.18}$$

Figure 5.18 shows plots of the measured temperature change for one experimental campaign and the computed values of the heat deposited and average heat flux per pulse. The

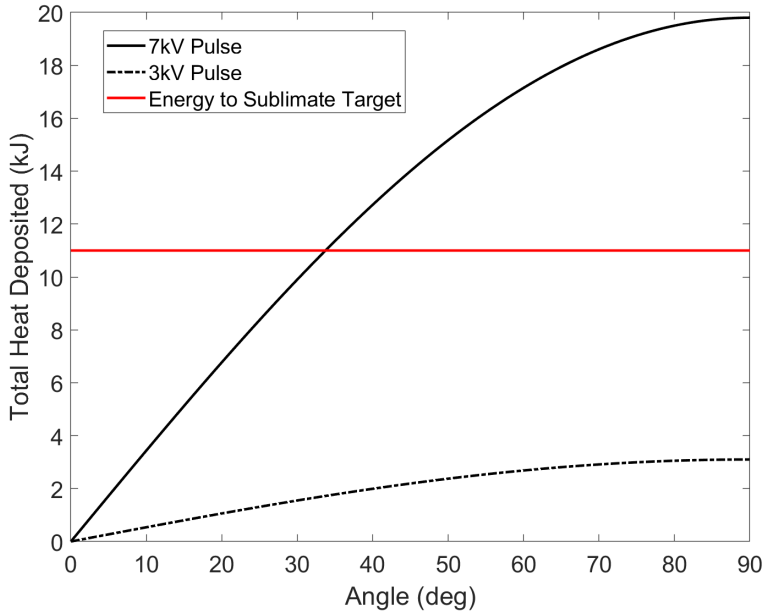

Figure 5.17: Energy deposition dependence on incidence angle to target. Total energy per pulse is shown for both the 3 kV and 7 kV cases. The red line indicates where the total heat deposition is enough to completely sublimate the target.

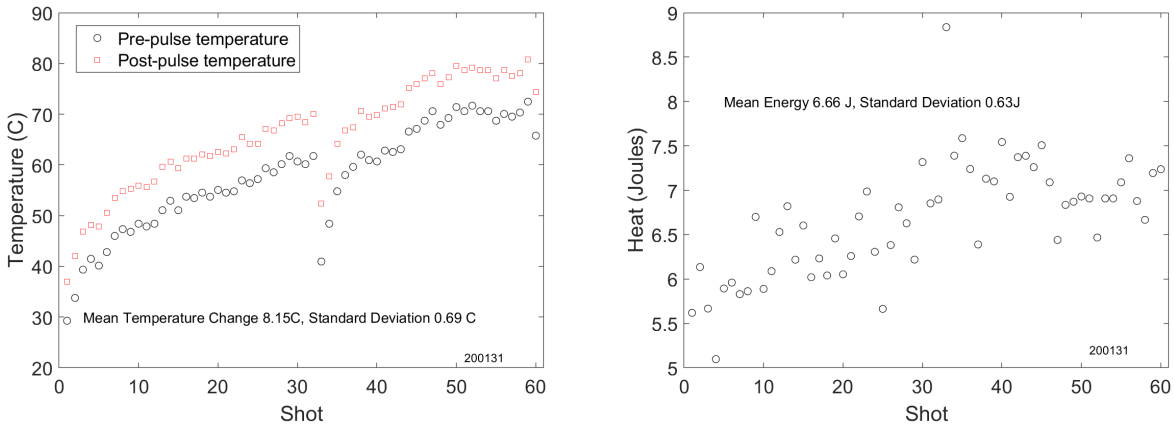

(a)

(b)

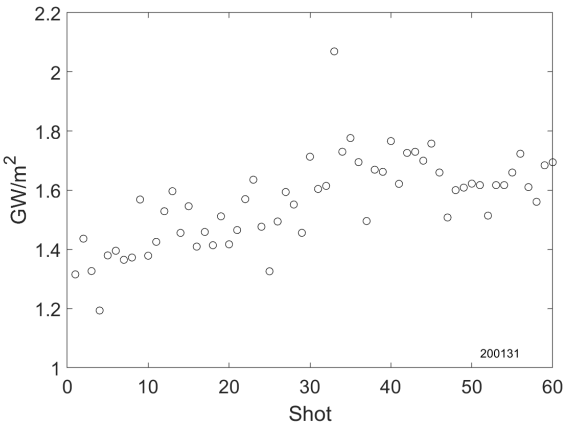

(c)

Figure 5.18: Sample data from the thermistor measurements at the back of the target. (a) The temperature at the rear of the target before and after each pulse over one run day. (b) Calculated heat deposition from the change in temperature. (c) An average measure of power per unit area per pulse.

energy deposition and heat flux are related by the average pulse duration, which is a constant, and therefore the trends are simply scaled between plots. Both plots have been included here to provide an example of the order of magnitude of the values and the fluctuations between pulses. The thermistor temperature measurements are plotted for each pulse in Fig. 5.18a. The target temperature increases steadily throughout the day, with a drop in temperature at shot 32 where there was a break in experimental operations. The change in target temperature is relatively constant, which produces a linear trend in calculated energy deposited to the target and heat flux from the plasma. A linear interpolation of $c(T)$ is used to calculate the change in energy of the target. The mean energy deposited to the target is calculated to be 6.7 J, roughly three orders of magnitude less than the value calculated from spectroscopy. Using the measured plasma properties, the target exposure time would have to be less than one microsecond to deposit this energy. There are a number of factors that could cause the discrepancy between the measurements. Some energy will be lost to melting and sputtering of the material during a pulse. Further energy will be radiated and conducted away from the target immediately following the pulse. While the e-folding time of the thermistor is 0.6 seconds, it took approximately five minutes for the thermistor to reach a steady temperature. This could be indicative of poor thermal contact between the thermistor and the target back. The magnitudes of these loss mechanisms will be evaluated later in the chapter.

A comparison of the calculated energy deposited to the target from thermistor data for a number of pulse series is shown in Fig. 5.19. The data in the plot are from four experimental campaigns with two initial condition settings. Data in black show calculated energy deposited to the target for plasma formed with a 3 kV compression bank charge, while red shows data for plasma with a 7 kV compression bank charge. Data are from both boron-nitride and graphite targets, with different heat capacities used to calculate the results. In general, the measured heat deposition appears constant for each pulse, with no clear difference seen between target type or compression bank voltage setting. This contradicts the expectation that a hotter plasma would heat the target more than a cool plasma. One possibility for this unexpected result could be that the thermistor is measuring the temperature

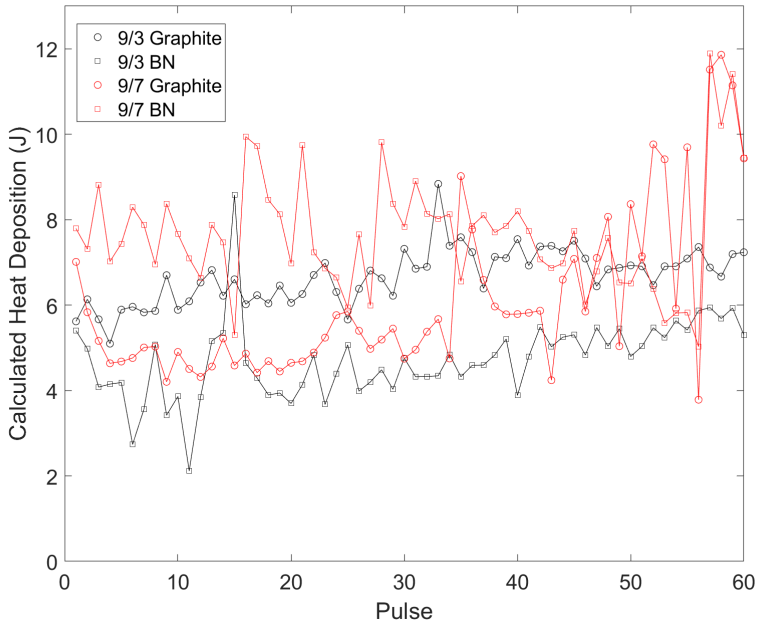

Figure 5.19: A comparison of calculated heat deposition for four pulse series. Each series consists of 60 pulses. Red markers indicate plasmas formed with a 7 kV compression bank charge, black shows plasmas with a 3 kV charge. The circles show data for graphite targets and the squares indicate boron-nitride targets.

of the boron-nitride mast, rather than the temperature of the target. The thermistor was not mounted to the target, but rather inserted into a close-fit slot. If the thermistor were displaced during installation, the thermistor measurements would grossly underestimate the target temperature, as any heating of the thermistor would take place through radiation or conduction through the diffuse gas remaining in the chamber immediately after the pulse.

5.5.2 Sputtering

Sputtering is the process by which a neutral atom from a solid surface is removed by an ion impact. There are two types of sputtering: physical and chemical. Physical, or knock-

on, sputtering, occurs when the energy from ion collisions overcomes the surface binding energy of the material. Chemical sputtering occurs when molecules are formed between the surface atoms and incident ions with low enough binding energies to be desorbed at the target temperature. Sputtering yields are dependent on a myriad of factors, including the ion energy and species, and chemical composition and temperature of the target. Due to the complexity of this process, the governing equations for yield determination are partially empirical [48], and yield coefficients are generally determined through reference tables.

The effects of the plasma properties on the target surface topography can be examined quantitatively using the modeling program SRIM. SRIM, the Stopping Range of Ions in Matter, calculates features of the transport of ions in matter using information about the ions and solid materials. The program uses statistical algorithms to analyze collisions between ions and atoms and compute properties such as the ion recoil distribution, damage to the solid material, and sputtering yields. Using data collected from the ZaP-HD diagnostics, the sputtering yield for different plasma parameters can be estimated and used to analyze the target surfaces. The impact energy is calculated using the same methods that were used to calculate the heat flux and total energy deposited to the target from the plasma. This energy is input to SRIM along with target material properties, and sputtering yields and material damage is calculated using a binary collision approximation. These yield coefficients can then be used to estimate physical sputtering of the ZaP-HD targets. Some sample sputtering yields for ZaP-HD plasmas are shown in Table 5.3. The sputtering yield does not necessarily increase with increased ion energy. If an ion is too energetic upon impact, it will be deeply implanted in the surface, rather than knocking off a superficial atom. Higher angles of particle incidence also result in higher sputtering yields. However, it is challenging to know exactly the angle of incidence, because the target surface is rough and local electric fields will act to change the particle trajectory. In general, the impact angle is assumed to be normal to the surface if the actual sputtering angle is not known.

Sputtering yields are calculated for the low, medium, and high temperature plasmas for three cases. The first case estimates yield from the front face of the target, calculated using

Ion Energy (eV)	0° Impact Angle	85° Impact Angle
350	0.0228	0.0545
700	0.0200	0.0932
950	0.0161	0.114

Table 5.3: Graphite yield coefficient calculations from SRIM using ZaP-HD plasma parameters.

particle flux with a magnetic field parallel to the surface. The second case estimates yield from the side of the target with the same method. The third estimates yield from the side of the target, calculated with a glancing angle of 3°. Figure 5.20a shows yields per plasma pulse for three incident ion energies based on measured plasma parameters and SRIM results. In all cases, the sputtering yield is significantly lower for the case with a small angle between the flux and the surface. The yield is highest for the low-energy case on the front face. The low energy ions also have the largest difference between the expected sputtered mass on the front and side faces of the target. Results for the 700 eV and 950 eV incident ion energy cases are roughly the same. All yields are in the range of micrograms of graphite.

Results from these calculations can be used to estimate the wear on the electrodes during operation. Understanding how often the electrode will need to be replaced is an important consideration to the design of a Z-pinch fusion reactor. The sputtering rate per area is found and used along with the density of the graphite to estimate the number of pulses necessary to sputter away 1 mm of material, shown in Fig. 5.20b. At the lowest incidence energy, the electrode will be eroded by 1 mm after only 200 to 300 pulses for the magnetized case. This does not consider material redeposited to the surface or material sublimated due to electrode heating. The higher energy cases show between 300 to 450 pulses are required to erode the same thickness.

It is important to note that in a fusion reactor configuration, the graphite would not

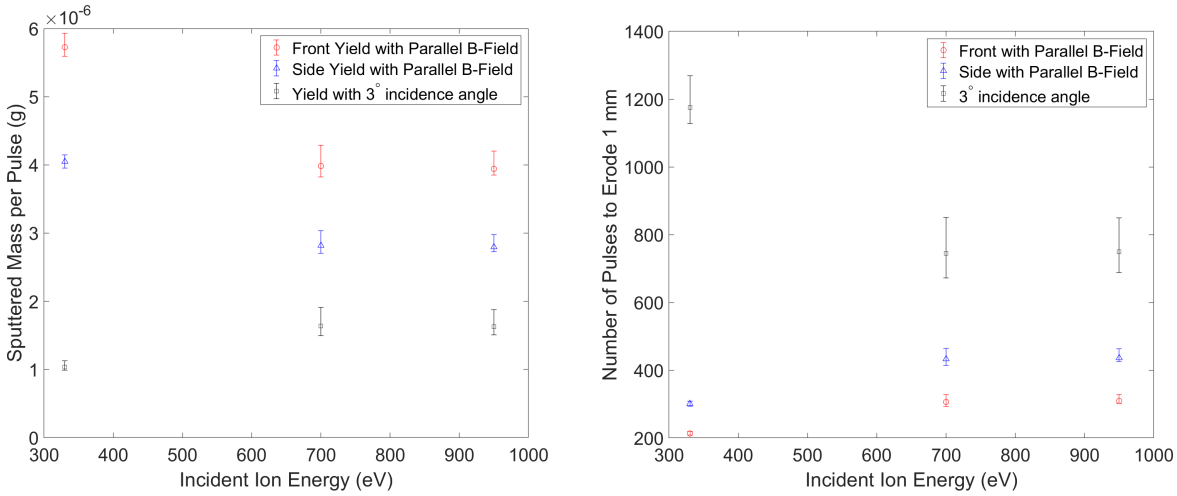

(a) (b)

Figure 5.20: Calculated sputtered mass per pulse and erosion rates for incident ions of varying energy. (a) Calculated sputtering mass for graphite per pulse with varying ion fluxes to the surface. (b) The number of pulses required to erode 1 mm of material (per area) given the sputtering yield per pulse.

be floating but have a bias voltage, and the temperature of the ions would be much higher than those produced in ZaP-HD. These factors will result in significantly higher impact energies for the ions. Experimental studies by Yamada [61] showed that carbon sputtering peaks below incident hydrogen ion energies of 1 keV. Therefore, the effects of sputtering in a reactor configuration could be reduced from the values presented here, although this would also be dependent on the particle flux to the surface, which will increase with the plasma density. In addition, this does not account for the additional electrode heating and melting that would occur. A sacrificial electrode could be designed with a geometry to minimize the ion flux to the surface. Creating an electrode design that is robust to erosion will be imperative to the functionality and cost of a Z-pinch fusion reactor.

Once sputtered, impurity atoms can become ionized and radiate energy in the plasma. A study on the PISCES device showed that if the ionization mean free path was shorter than the characteristic length of the plasma, graphite sputtered with hydrogen would be redeposited onto the surface as a crystal structure [11]. In the ZaP-HD case, the ionization mean free path can be compared to the Larmor radius to determine if sputtered atoms might be redeposited onto the targets. The ionization mean free path is calculated from

$$\lambda_{iz} = \frac{v_{th,n}}{\nu_{en}} \tag{5.19}$$

where $v_{th,n}$ is the thermal velocity of the sputtered neutrals and

$$\nu_{en} = n_n < \sigma_{en} v_e > . \tag{5.20}$$

Here σ_{en} is the momentum transfer cross section from ions to neutrals, the value for which varies with electron temperature and is found in Ref. [57]. The density of neutrals around the target is found using the particle fluxes determined in the previous section and the sputtering yields from SRIM. The neutral thermal velocity is calculated from the mean sputtered atom energy, which is also a parameter found with SRIM. 350 eV plasma ions sputter neutrals with an average energy of 19.5 eV, while atoms sputtered from 950 eV ions have an average energy of 28.45 eV. The ionization mean free path for the two cases is found to be .02 cm

and .035 cm respectively. To calculate the Larmor radius, the equation

$$r_L = \frac{mv_\perp}{eB} \tag{5.21}$$

is used, where $v_\perp$ is assumed to be the neutral thermal velocity. The Larmor radius for each case is found to be 0.28 cm and 0.16 cm for the low- and high-ion-energy cases, respectively. Therefore, for both cases it is expected that sputtered carbon atoms from the surface would be redeposited. However, only the micrographs for the 3 kV plasma show the characteristic structures that indicated redeposition in the PISCES experiments.

One explanation for the lack of redeposited structures on the targets exposed to high-temperature plasma is that those targets heated up beyond the graphite sublimation temperature. Graphite will begin to sublimate between 3900 and 4000 K, unless the pressure is greater than 110 atmospheres, at which point the graphite would melt. The target temperature after a pulse can be calculated using the calculated energy deposited from the heat flux analysis and Eqn. 5.17. A mean value of c = 0.8 J/g-K is used to find the change in temperature of the target. The change in temperature from the low-energy plasma exposure is found to be 1800 K ± 220 K while the high-energy plasma produces a ΔT of 4300 K ± 500 K. The targets exposed to high-temperature plasmas likely exceed the sublimation temperature for graphite. The small redeposited structures would be sublimated to a flat surface, due to their poor thermal conductivity with the more dense intact target. A gray body radiation analysis of the target indicates that the five-minute interval between pulses is enough to cool all targets to 400 to 500 K between each pulse, preventing the targets in the 3 kV plasma from exceeding the sublimation temperature threshold.

The sublimation of the target surface after exposure to the 7 kV plasma pulses could ultimately be beneficial to machine operations with a graphite electrode. A flatter surface will increase the likelihood that ions will impact at a 90° angle. This will lead to less sputtering, and therefore fewer impurity ions entering the bulk plasma. The impurity ions absorb energy through additional ionization and lose energy through radiation, lowering the efficiency of the bulk plasma. Reducing impurity sputtering through plasma processing would improve

the bulk plasma performance and be beneficial to a reactor configuration.

5.5.3 Boron-Nitride Melting

Boron-nitride micrographs shown in Fig. 5.14 indicate extensive melting of material. The BN targets are challenging to analyze with surface diagnostics due to their low conductivity. Surfaces could not be analyzed with EDS without applying a coating that would destroy some structures. Analysis here has been completed assuming that the melted structures are made of boron-nitride, rather than tungsten or another material that has been sputtered from the ZaP-HD device. The lower voltage used to obtain the SEM images should highlight surface features, rather than material Z, and therefore we might assume that the brightness of the droplets seen in each image is a result of difference in height from the bulk surface, rather than a difference in material.

The extent of surface melting can be measured by determining the size and number of melted features in the micrographs. Images are analyzed in Matlab using the Hoshen-Kopelman algorithm to efficiently measure the bubbles of melted material [22]. The micrographs are converted to a binary format such that the bubbles are defined from the background. The Hoshen-Kopelman algorithm identifies unique clusters in the binary array and tracks their location and size. A sample of the difference in contrast is shown in Fig. 5.21. Measured features are required to be larger than four pixels in radius and have an eccentricity less than 0.5 to prevent the algorithm from identifying the background as a melted feature. The number and size of the melted features are collected and used to analyze the surface damage. A sample of identified features in a binary micrograph is presented in Fig. 5.22.

The data are examined in relation to measured plasma parameters in Fig. 5.23. The total area covered by melted features is calculated and shown as a percentage of the imaged area for each set of initial conditions. These percentages are compared to plasma exposure time (5.23a), measured energy deposition from the thermistor (5.23b), and calculated energy

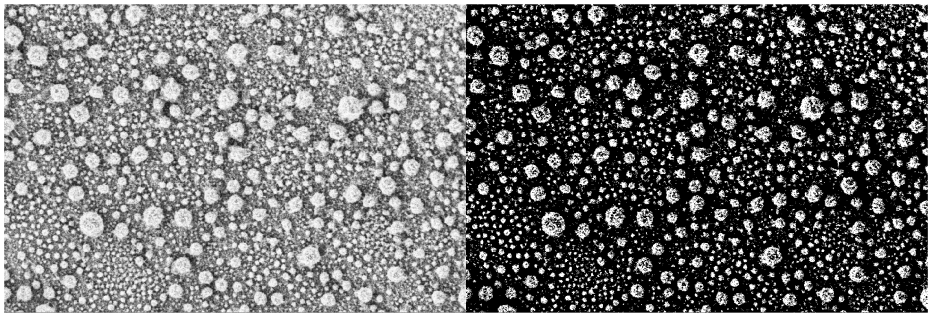

Figure 5.21: A comparison of a micrograph of the BN surface and the same micrograph after being converted to a binary image.

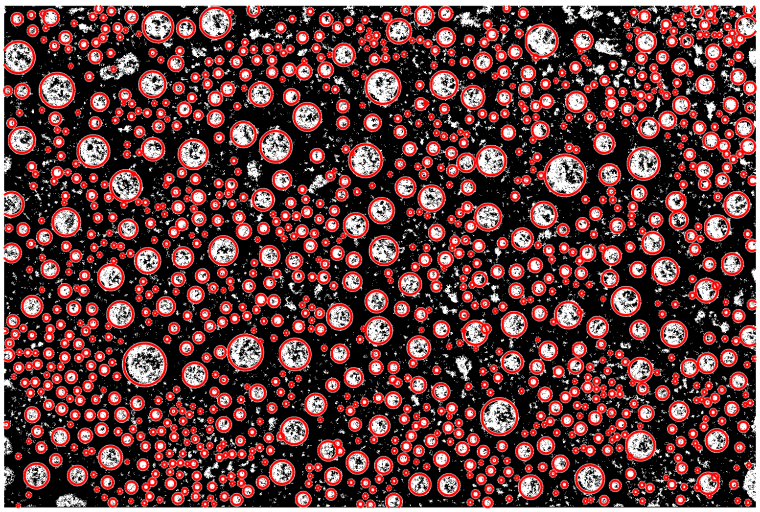

Figure 5.22: Melted boron-nitride identified by the analysis. The Hoshen-Kopelman algorithm finds and identifies unique clusters in a binary array. Red circles indicate melted area identified by the algorithm.

deposition from spectroscopy (5.23c). The images were all obtained for the front face of the target, therefore the parallel magnetic field case was used to calculate the deposited energy for the spectroscopy data. Figure 5.23d shows a comparison of the total number of features identified in each micrograph and the mean radius of the features.

The data in Fig. 5.23a indicate that longer exposure to the plasma results in an increase in melted material. It also appears that the targets exposed to the hotter plasmas showed less melting than targets exposed to cooler plasma. However, for the targets exposed to 60 plasma pulses the error is large enough that the melted area may not be significantly different. Figures 5.23b and 5.23c do not show a clear relationship between the energy deposited per pulse and the amount of melting detected. The average feature radius, shown in Fig. 5.23d, is similar across all initial conditions, although all pulses except the 20 exposure, 7 kV plasma show high variance in the measured radius. As the exposure time is increased, the melted material becomes less spherical and is less easily identified by the algorithm. Micrographs taken at low magnification, shown in Fig. 5.24, capture widespread melting with features at a larger scale than those analyzed with the Matlab algorithm. Both targets in this figure have been exposed to 60 plasma pulses, with the target in Fig. 5.24a in a 3 kV plasma and the target in Fig. 5.24b in the 7 kV plasma. A low-magnification image of an unexposed surface has been included for reference in Fig. 5.24c. Melting and erosion is apparent in both cases, and the amount of damage visible on each surface is similar. Unfortunately, the jagged surface makes automatic identification of the melted area of the target challenging, and the melted area could not be quantified for low-magnification micrographs. From this analysis, it appears that surface melting is more dependent on prolonged exposure to the plasma, rather than the energy of the individual ion impacts.

At atmospheric pressure and 3400 K, boron-nitride will dissociate rather than melt. To reach a liquid state, there must either be a large (>5%) concentration of nitrogen in the plasma [40], or the pressure must exceed 400 Pa [53], which is equivalent to the magnetic pressure from a 0.03 T field. Conditions in ZaP-HD far exceed this pressure threshold for melting. Although challenging to determine from micrographs alone, plasma exposure ap-

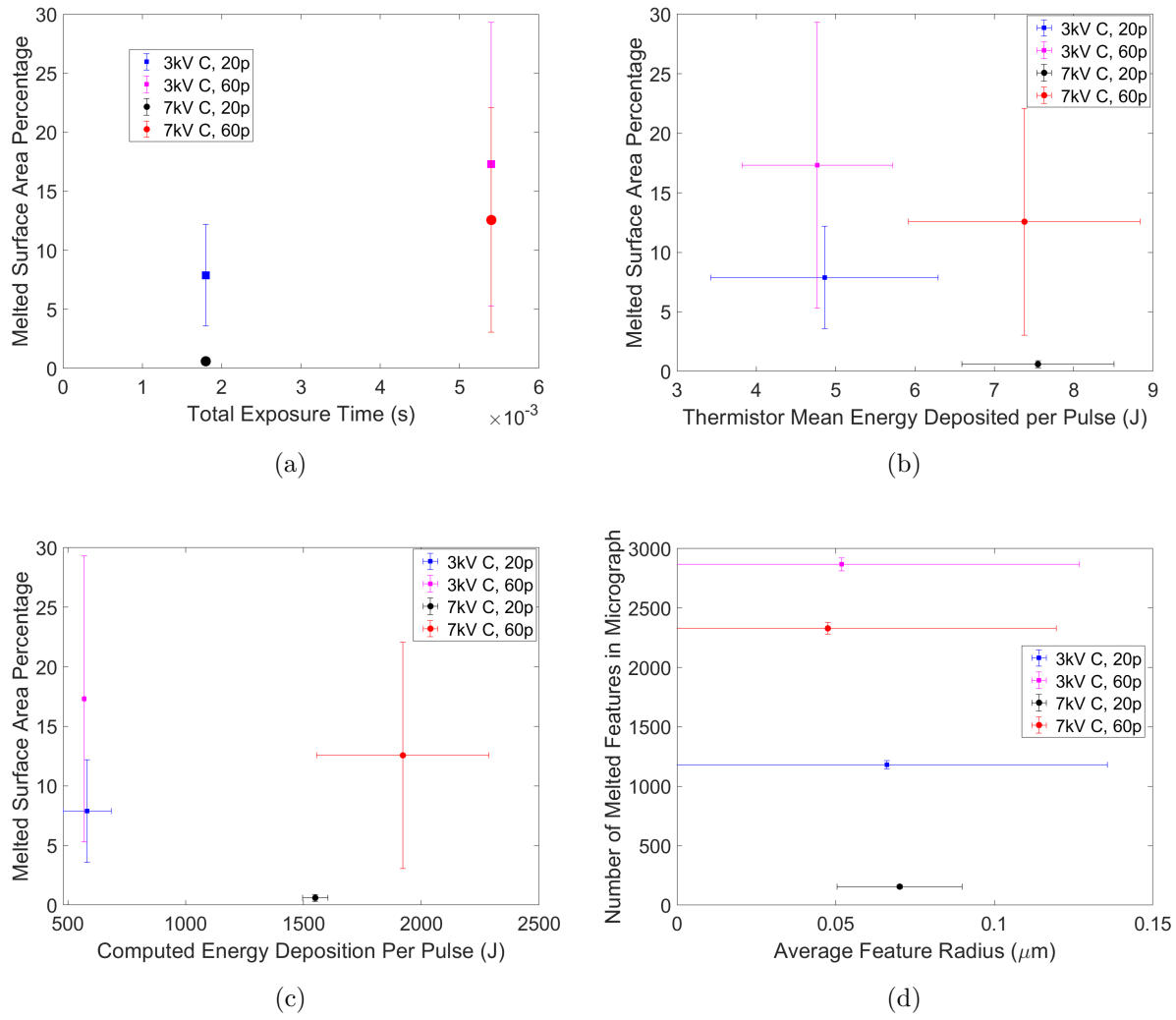

Figure 5.23: A comparison of melted surface area to various plasma parameters. Except for (d), the melted area is shown as a percentage of the total area imaged in the micrograph. (a) Percent coverage of melted BN compared to total plasma exposure time. (b) Percent coverage of melted BN compared to pulse energy measured by thermistor. (c) Percent coverage of BN compared to pulse energy calculated from spectroscopy. (d) A comparison of mean feature radius and number of melted features for all initial conditions.

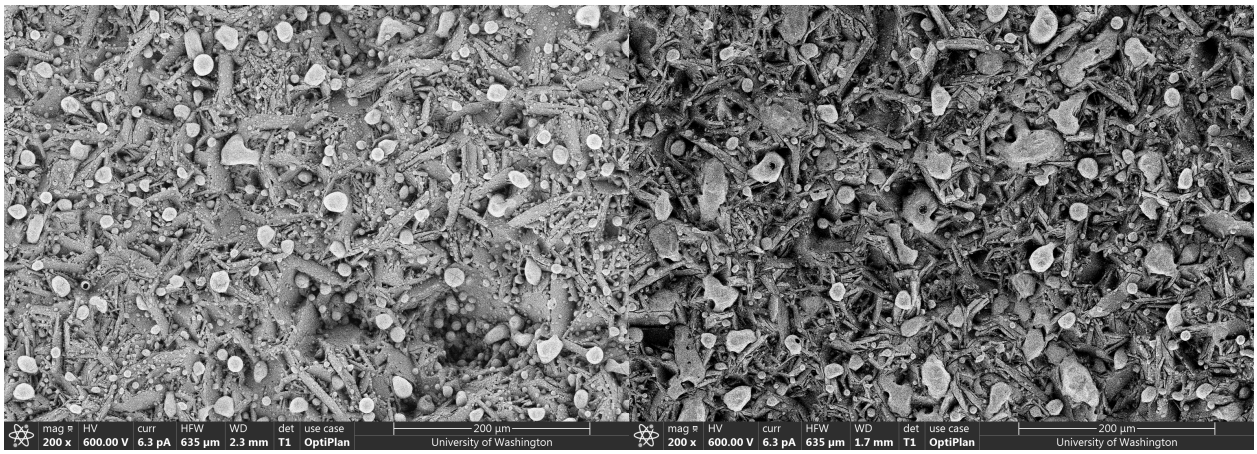

(a) (b)

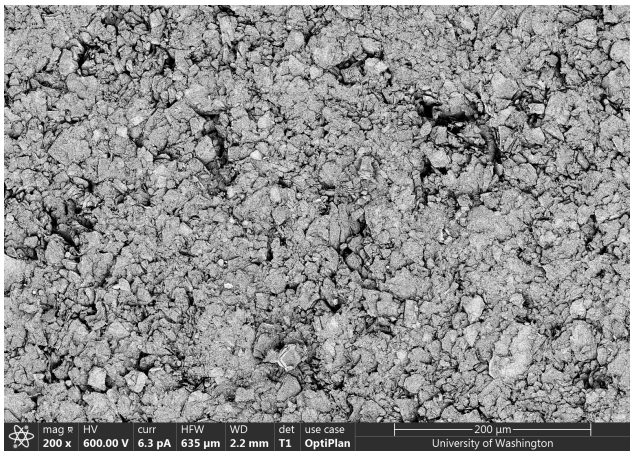

(c)

Figure 5.24: A low magnification comparison of two plasma-processed BN targets and a control surface. Both targets were exposed to 60 plasma pulses. The target in (a) was placed in a low-temperature plasma while (b) was exposed to a high-temperature plasma. Surface deformation appears to be more dependent on exposure time than plasma energy. The control surface is included for reference in (c).

pears to have increased the surface roughness of the targets. While BN is not chemically affected by melting, changes in the surface roughness can increase the material resistivity and friction between the surface and a flowing fluid. Minimizing the plasma contact with BN surfaces will ensure that changes in material properties do not affect plasma performance. These preliminary results suggest boron-nitride may not be a suitable material choice for applications with prolonged exposure to energy-dense plasmas, such as in a reactor or fusion-propulsion configuration.

5.6 Suggestions for Improvements to the Testing Apparatus

The design of the PMI target test stand was intended to adapt an existing experiment for a new purpose with as few modifications as possible. While the design worked reasonably well, additional PMI campaigns on the ZaP-HD device may want to modify the experimental set-up for ease of use and reliability.

The system of connections between the translation stage, thermistor, and target would benefit from a redesign. The current set-up uses a set screw to connect the boron-nitride mast to the copper adapter. Even though the mast did not need to be removed and replaced often, the BN began to wear early in the experimental campaign. Boron-nitride is slippery, and the combination of the cantilevered weight of the target and the orientation of the threads relative to the weight distribution caused the target to occasionally sag before or during testing. Several times, testing was halted (or not begun) because the orientation of the target had significantly changed and the front face was no longer normal to the plasma flow. The simplest method to fix this would be to move the translation stage to the $-x$ side of the machine. This would change the direction of the target moment such that it tightened the mast on the set screw, rather than loosened it. Another fix might be to revert to the clamping system used by Jon Weed, although this would require a much larger copper adapter.

The interface between the thermistor and the target should be adjusted to provide a more

accurate reading of the target temperature. The Honeywell HRTS Resistance Temperature Detector has a time constant of 0.6 seconds, but took approximately three to five minutes to heat up to an equilibrium temperature after each pulse, indicating poor thermal contact with the target. In the current configuration, the thermistor is tightly fitted into the center of the BN mast, but there are no other provisions to stop it from rotating or slipping down the mast during installation. Machining a slot at the top of the rod to precisely fit the thermistor dimensions, or adding a slot to the target for the thermistor to occupy, would provide a better connection between the sensor and the target and therefore a more accurate measurement of temperature. Another option may be permanently attaching a thermistor to the back of each target to ensure good contact. The operating temperature range of the thermistor should also be considered. The Honeywell HRTS-5760-B-U-0-12 is designed for an operating range of -70 to 260° C. The calculated target temperatures from spectroscopy data were an order of magnitude higher than this range. As most thermistors are only able to operate up to 300° C, finding a different method for determining the temperature of the target may benefit the experiment.

Finally, using a translation stage with less freedom of positioning would improve the repeatability of the target placement in the machine. The set-up uses a translation stage with micrometer adjustment and 6" of travel. For these studies, the target only needed to be located in one of two positions: outside of the chamber or on the chamber axis. Changing the position of the target took at least 5 minutes each time due to the accuracy of the the micrometer. The centered position was marked on the translation stage, but the stage indicator was missing from the translation stage assembly, and therefore the ultimate position of the translation stage could only be approximated. A simpler mounting system with only two positions would make it easier to reliably put the target in the center of the machine every time.

Chapter 6

CONCLUSION

The ZaP-HD Flow Z-Pinch Experiment was designed to investigate scaling the sheared-flow stabilized Z pinch to higher energy densities. Experimental campaigns led to a better understanding of machine operation and achieved densities of over 1×10^{24} m^{-3} and temperatures of up to 1 keV. Spectroscopic measurements showed evidence of a hot core pinch with a peaked temperature profile surrounded by a uniform, lower-temperature background plasma. These measurements combined with magnetic mode data indicated these small-radii pinches are stable for up to 45 μs even with the background plasma present. The performance gains over the original ZaP device seen on ZaP-HD indicate a tri-axial electrode configuration may benefit high-power devices like the FuZE experiment.

Time-resolved spectroscopy provides an easy method for expanding spectroscopic measurements during a plasma pulse with existing equipment. Simultaneous collection of temperature and velocity data can provide a more complete picture of the plasma behavior during a pulse. The time-resolved velocity shear plots show a new way of looking at the evolution of plasma shear over the pinch lifetime. The diagnostic is easily integrated into existing spectroscopy set-ups, and can be expanded to make measurements at multiple locations in the experiment. Peaked temperature profiles were measured from carbon-III radiation at low capacitor bank voltages. Temperature profiles flattened as the bank voltages were increased in a manner similar to the flat background measured with the ICCD. The duration and magnitude of computed velocity shear increased dramatically with the capacitor bank voltage. This coincided with extended quiescent periods, further suggesting hotter temperatures might be measured from higher ionization states of carbon or other impurity ions.

Three-dimensional digital holographic interferometry was developed to make the first

measurements of the 3D pinch structure on the ZaP-HD Device. Holograms showed a variety of structures present during the course of the pulse. The three-dimensional renderings of Abel-inverted data indicate the approximate geometry of the pinch along one to two centimeters of the z axis. Looking at orthogonal views of the plasma reveals structure that might go otherwise undetected with a single viewing chord.

Plasma-material interaction experiments were performed to better understand the damage to solid surfaces in high-energy environments. Data were collected for a range of ion impact energies and ion fluences. Inserting a target into the Z pinch does not appear to have affected the temperatures and densities of the upstream plasma. Stagnated plasma surrounds the target throughout the pulse. Theoretically, this stagnated plasma prevents the pinch magnetic field from penetrating into the target material. The magnetic field and the direction of plasma flow act to reduce the particle flux and therefore energy deposited from the bulk plasma to the surface. Micrographs indicate that targets exposed to ions with lower impact energies show evidence of redeposition of sputtered carbon, while targets exposed to high-energy ions lack the same structure. The targets in hotter plasmas could exceed the graphite sublimation temperature, removing these redeposited structures as a result. The sides of the targets all show evidence of melting, which can only occur in a high-pressure environment. This discrepancy in topography could be caused by the pinch could be bending around the target and therefore the hottest, high-pressure plasma would make contact with the target sides while missing the front. Unlike the graphite, boron-nitride targets all show evidence of melting, with a dependence on total ion fluence but not ion impact energy. Results from these experiments can be used to lay the groundwork for developing electrodes that will survive fusion reactor conditions.

Chapter 7

FUTURE WORK

Though the data presented in this thesis represents a large experimental effort, many unexplored avenues remain for both the diagnostics and PMI investigations on the ZaP-HD machine. Further studies of the stabilizing effects of velocity shear could be made with time-resolved spectroscopy. Additional materials and manufacturing methods should be tested in PMI experiments, and the effects of magnetic fields further explored. A more thorough investigation of asymmetries in target deformation would also be beneficial.

Time-resolved spectroscopy was developed to resolve the ion temperature and velocity for the entire plasma pulse. A focused series of experiments should be made to better understand the nature of the velocity shear and correlate the presence of shear with data from other diagnostics. Measuring velocity with the 20-chord fiber bundle would provide better spatial resolution and therefore would better resolve the location and magnitude of the shear. In addition, velocity measurements should be made from line radiation from other impurity ions. Given that the measurements of high-energy plasma indicated carbon-III radiation came from the background plasma and not the pinch core, the velocity of this core must also be measured to understand the behavior of the Z pinch. This might be accomplished by measuring emission from an oxygen line, such as oxygen-IV, V, or VI. Increasing the spatial resolution and changing the impurity line of interest could help better understand the physics of shear-flow stabilization of the small, energy dense Z pinches produced on ZaP-HD.

Plasma-material interaction experiments studied two materials commonly found in plasma applications. Graphite is a conductor, while boron-nitride is an insulator. However, both materials are low Z. Continuing the investigation with copper-tungsten targets would provide evidence of how high Z materials are affected by high-energy ion bombardment. In addition,

testing this material might provide more information about the Z-pinch formation, which relies on secondary electron emission from the tungsten-coated copper electrode. Different manufacturing methods could also be investigated. Additional machining to reduce surface roughness, or using additive manufacturing to increase surface roughness, would likely be effective in manipulating conditions at the target surface and reducing or increasing the sputtering yield.

The analysis in this work postulated that the particle fluence to the surface was limited by the magnetic field. The effects of magnetic field near the target can be tested directly with several experiments. A permanent magnet could be embedded in the target, changing the field profile to open field lines to the target surface. The damage and change in target temperature compared to data without the magnet could be used to quantify the degree to which the pinch magnetic field limits the particle flux. Targets could also be exposed to unmagnetized plasmas using a vacuum chamber extension like the one currently installed on the FuZE device. An unmagnetized plasma would have particle flux that adheres more closely to the simple Bohm criterion presented in the Theory section of Chapter 5. Without the limiting magnetic field, differentiating between the effects of thermal and kinetic energy on target surface deformation might be made easier. Additional research is necessary to quantify how much plasma actually escapes the outer electrode to the vacuum chamber extension before this experiment could be performed.

Due to time constraints, only one site on the side of each target was examined to obtain micrographs. Given the geometry of the target, it is expected that the stagnated cloud of plasma would tend to build up on the top and bottom, where the mast sticks out prominently, and would tend to be thinner on the left and right sides. The effects of the mast blocking plasma flow could be quantified by a more thorough cataloging of the target surface with the scanning electron microscope. It may also be beneficial to add indexing marks to the target. This would allow the measurements to be correlated to the target orientation relative to the mast during testing.

Finally, a more thorough and reliable method for directly measuring the target temper-

ature should be developed to quantify the heat deposited from the plasma to the target. This might be accomplished by embedding a thermocouple into the target, or by attaching one permanently with high-temperature adhesive. Another suitable method might be to monitor infrared radiation from the target surface. IR temperature sensors are a commonly used diagnostic, but the windows currently used on ZaP-HD and FuZE block IR radiation. Installing a new window or an optical fiber in the experiment to pass IR radiation would provide a simple method to directly measure the surface temperature of the target without installing an invasive diagnostic.

BIBLIOGRAPHY

[1] Sheared flow stabilization of the m= 1 kink mode in z.

[2] Fernando Mendoza Santoyo Tonatiuh Saucedo-A et al. Araceli Sánchez, H Manuel. Simultaneous 3d digital holographic interferometry for strain measurements validated with fem. *Optics and Lasers in Engineering*, 58.

[3] LA Artsimovich, AM Andrianov, OA Bazilevskaya, Yu G Prokhorov, and NV Filippov. An investigation of high-current pulsed discharges. *Journal of Nuclear Energy (1954)*, 4(2):203–208, 1957.

[4] Anthony G Atkins, Tony Atkins, and Marcel Escudier. *A dictionary of mechanical engineering*. Oxford University Press, 2013.

[5] Monika Auweter-Kurtz, Markus Feigl, and Michael Winter. Diagnostic tools for plasma wind tunnels and reentry vehicles at the IRS. Technical report, STUTTGART UNIV (GERMANY FR) INST FUERRAUMFAHRTSYSTEME, 2000.

[6] Christopher Robert Ball and Joel S Lash. Sandia Z Machine Overview and Debris Measurements. Technical report, Sandia National Lab.(SNL-NM), Albuquerque, NM (United States), 2015.

[7] Rainer Behrisch and Wolfgang Eckstein. *Sputtering by particle bombardment: experiments and computer calculations from threshold to MeV energies*, volume 110. Springer Science & Business Media, 2007.

[8] Willard H Bennett. Magnetically self-focussing streams. *Physical Review*, 45(12):890, 1934.

[9] RC Bissell and PC Johnson. The solution of the plasma equation in plane parallel geometry with a maxwellian source. *The Physics of fluids*, 30(3):779–786, 1987.

[10] Boyd D Blackwell, Juan Francisco Caneses, Cameron M Samuell, John Wach, John Howard, and Cormac Corr. Design and characterization of the Magnetized Plasma Interaction Experiment (MAGPIE): a new source for plasma–material interaction studies. *Plasma Sources Science and Technology*, 21(5):055033, 2012.

[11] J Bohdansky, CD Croessmann, J Linke, JM McDonald, DH Morse, AE Pontau, RD Watson, JB Whitley, DM Goebel, Y Hirooka, et al. Behavior of graphite under heat load and in contact with a hydrogen plasma. *Nuclear Instruments and Methods in Physics Research Section B: Beam Interactions with Materials and Atoms*, 23(4):527–537, 1987.

[12] David Book and JD Huba. NRL plasma formulary. Technical report, NAVAL RESEARCH LAB WASHINGTON DC PLASMA PHYSICS DIV, 2002.

[13] Michael R Brown, CD Cothran, and J Fung. Two fluid effects on three-dimensional reconnection in the swarthmore spheromak experiment with comparisons to space data. *Physics of plasmas*, 13(5):056503, 2006.

[14] M Coppins, ID Culverwell, and MG Haines. Time dependent Z-pinch equilibria. *The Physics of fluids*, 31(9):2688–2694, 1988.

[15] B de Groot, Z Ahmad, RP Dahiya, R Engeln, WJ Goedheer, NJ Lopes Cardozo, and V Veremiyenko. Magnum-psi, a new linear plasma generator for plasma-surface interaction studies in ITER relevant conditions. *Fusion engineering and design*, 66:413–417, 2003.

[16] Raymond Golingo. *Formation of a Sheared Flow Z-Pinch*. PhD thesis, University of Washington, 2006.

[17] RP Golingo and U Shumlak. Spatial deconvolution technique to obtain velocity profiles from chord integrated spectra. *Review of scientific instruments*, 74(4):2332–2337, 2003.

[18] H Grote, W Bohmeyer, H-D Reiner, T Fuchs, P Kornejew, and J Steinbrink. Comparison of chemical sputtering yields for different graphites at high ion flux densities. *Journal of nuclear materials*, 241:1152–1155, 1997.

[19] DJ Den Hartog and RP Golingo. Telecentric viewing system for light collection from a Z-pinch plasma. *Review of Scientific Instruments*, 72(4):2224–2225, 2001.

[20] Georg Herdrich, Monika Auweter-Kurtz, HL Kurtz, Torsten Laux, and Michael Winter. Operational behavior of inductively heated plasma source IPG3 for entry simulations. *Journal of Thermophysics and Heat Transfer*, 16(3):440–449, 2002.

[21] EM Hollmann, A Yu Pigarov, R Seraydarian, DG Whyte, and SI Krasheninnikov. Particle balance measurements during detachment in a gas-target divertor simulator. *Physics of Plasmas*, 9(4):1226–1232, 2002.

[22] Joseph Hoshen and Raoul Kopelman. Percolation and cluster distribution. i. cluster multiple labeling technique and critical concentration algorithm. *Physical Review B*, 14(8):3438, 1976.

[23] Joseph D Huba. NRL plasma formulary. Technical report, NAVAL RESEARCH LAB WASHINGTON DC PLASMA PHYSICS DIV, 2006.

[24] Ian H Hutchinson. Principles of plasma diagnostics. *Plasma Physics and Controlled Fusion*, 44(12):2603, 2002.

[25] Leonid Pinkhusovich IAroslavskii and Nikolai Stepanovich Merzliakov. Methods of digital holography. *Moscow Izdatel Nauka*, 1977.

[26] B Jones, CA Jennings, JE Bailey, GA Rochau, Y Maron, CA Coverdale, EP Yu, SB Hansen, DJ Ampleford, PW Lake, et al. Doppler measurement of implosion velocity in fast Z-pinch x-ray sources. *Physical Review E*, 84(5):056408, 2011.

[27] BB Kadomtsev et al. Hydromagnetic stability of a plasma. *Reviews of plasma physics*, 2:153–199, 1966.

[28] Sean D Knecht, Raymond P Golingo, Brian A Nelson, and Uri Shumlak. Calculation of the equilibrium evolution of the zap flow Z-pinch using a four-chord interferometer. *IEEE Transactions on Plasma Science*, 43(8):2469–2479, 2015.

[29] JA Koch, RE Stewart, P Beiersdorfer, R Shepherd, MB Schneider, AR Miles, HA Scott, VA Smalyuk, and WW Hsing. High-resolution spectroscopy for doppler-broadening ion temperature measurements of implosions at the national ignition facility. *Review of Scientific Instruments*, 83(10):10E127, 2012.

[30] Nikola Konjević. Plasma broadening and shifting of non-hydrogenic spectral lines: present status and applications. *Physics reports*, 316(6):339–401, 1999.

[31] A. Kramida, Yu. Ralchenko, J. Reader, and and NIST ASD Team. NIST Atomic Spectra Database (ver. 5.7.1), [Online]. Available: `https://physics.nist.gov/asd` [2017, April 9]. National Institute of Standards and Technology, Gaithersburg, MD., 2019.

[32] Robert A Langley, J Bohdansky, W Eckstein, P Mioduszewski, J Roth, E Taglauer, EW Thomas, H Verbeek, and KL Wilson. Data compendium for plasma-surface interactions. *Nuclear Fusion*, 24(S1):S9, 1984.

[33] KM Lemmer, AD Gallimore, and TB Smith. Using a helicon source to simulate atmospheric re-entry plasma densities and temperatures in a laboratory setting. *Plasma Sources Science and Technology*, 18(2):025019, 2009.

[34] Guang-Hong Lu, Long Cheng, Kameel Arshad, Yue Yuan, Jun Wang, Shaoyang Qin, Ying Zhang, Kaigui Zhu, Guang-Nan Luo, Haishan Zhou, et al. Development and optimization of STEP—a linear plasma device for plasma-material interaction studies. *Fusion Science and Technology*, 71(2):177–186, 2017.

[35] John Marshall. Performance of a hydromagnetic plasma gun. *Physics of Fluids (US)*, 3, 1960.

[36] GF Matthews, SJ Fielding, GM McCracken, CS Pitcher, PC Stangeby, and M Ulrickson. Investigation of the fluxes to a surface at grazing angles of incidence in the tokamak boundary. *Plasma Physics and Controlled Fusion*, 32(14):1301, 1990.

[37] Robert D Matulka and Daniel J Collins. Determination of three-dimensional density fields from holographic interferograms. *Journal of Applied Physics*, 42(3):1109–1119, 1971.

[38] V Milosavljević and G Poparić. Atomic spectral line free parameter deconvolution procedure. *Physical Review E*, 63(3):036404, 2001.

[39] Masayoshi Nagata, Roger Raman, Vlad Soukhanovskii, Brian A Nelson, Ronald E Bell, Dennis Mueller, Thomas R Jarboe, Michael G Bell, NSTX Research Team, et al. E× B plasma rotation and n= 1 oscillation observed in the NSTX-CHI experiments. *Plasma and Fusion Research*, 2:035–035, 2007.

[40] Jonathan Phillips, Seth S Gleiman, and Chun-Ku Chen. Spherical boron nitride particles and method for preparing them, November 25 2003. US Patent 6,652,822.

[41] Daniel Reda, Michael Wilder, David Bogdanoff, and Joseph Olejniczak. Aerothermodynamic testing of ablative reentry vehicle nosetip materials in hypersonic ballistic-range environments. In *USAF developmental test and evaluation summit*, page 6829. 2004.

[42] Robert E Reinovsky. Pulsed power experiments in hydrodynamics and material properties. *IEEE Transactions on Plasma Science*, 28(5):1563–1570, 2000.

[43] K-U Riemann. The Bohm criterion and sheath formation. *Journal of Physics D: Applied Physics*, 24(4):493, 1991.

[44] Michael Ross. *Exploring Plasma Stability and Confinement with High Resolution Density Measurements on the ZaP-HD Flow Z-Pinch*. PhD thesis, University of Washington, 2016.

[45] MP Ross and U Shumlak. Digital holographic interferometry employing fresnel transform reconstruction for the study of flow shear stabilized Z-pinch plasmas. *Review of Scientific Instruments*, 87(10):103502, 2016.

[46] J Roth, J Bohdansky, W Poschenrieder, and MK Sinha. Physical and chemical sputtering of graphite and sic by hydrogen and helium in the energy range of 600 to 7500 ev. *Journal of Nuclear Materials*, 63:222–229, 1976.

[47] Ulf Schnars. Direct phase determination in hologram interferometry with use of digitally recorded holograms. *JOSA A*, 11(7):2011–2015, 1994.

[48] Krishna Seshan and Dominic Schepis. *Handbook of thin film deposition*. William Andrew, 2018.

[49] VD Shafranov. The stability of a cylindrical gaseous conductor in a magnetic field. *The Soviet Journal of Atomic Energy*, 1(5):709–713, 1956.

[50] U Shumlak, CS Adams, JM Blakely, B-J Chan, RP Golingo, SD Knecht, BA Nelson, RJ Oberto, MR Sybouts, and GV Vogman. Equilibrium, flow shear and stability measurements in the Z-pinch. *Nuclear fusion*, 49(7):075039, 2009.

[51] U Shumlak, R Lilly, C Adams, R Golingo, S Jackson, S Knecht, and BA Nelson. Advanced space propulsion based on the flow-stabilized Z-pinch fusion concept. In *42nd AIAA/ASME/SAE/ASEE Joint Propulsion Conference & Exhibit*, page 4805, 2006.

[52] Uri Shumlak, BA Nelson, EL Claveau, EG Forbes, RP Golingo, MC Hughes, RJ Oberto, MP Ross, and TR Weber. Increasing plasma parameters using sheared flow stabilization of a Z-pinch. *Physics of Plasmas*, 24(5):055702, 2017.

[53] Vladimir L Solozhenko, Vladimir Z Turkevich, and Wilfried B Holzapfel. Refined phase diagram of boron nitride. *The Journal of Physical Chemistry B*, 103(15):2903–2905, 1999.

[54] Lyman Spitzer. *Physics of fully ionized gases*. Courier Corporation, 2006.

[55] PC Stangeby, CS Pitcher, and JD Elder. The nature of plasma fluxes to surfaces nearly tangential to the magnetic field. *Nuclear fusion*, 32(12):2079, 1992.

[56] Peter C Stangeby. *The plasma boundary of magnetic fusion devices*. CRC Press, 2000.

[57] Hiroya Suno and Takako Kato. Cross section database for carbon atoms and ions: Electron-impact ionization, excitation, and charge exchange in collisions with hydrogen atoms. *Atomic Data and Nuclear Data Tables*, 92(4):407–455, 2006.

[58] RJ Trainor, WM Parsons, EO Ballard, RR Bartsch, JF Benage, GA Bennett, RL Bowers, DW Bowman, JH Brownell, JC Cochrane, et al. Overview of the Atlas project. In *Digest of Technical Papers. 11th IEEE International Pulsed Power Conference (Cat. No. 97CH36127)*, volume 1, pages 37–46. IEEE, 1997.

[59] GV Vogman and U Shumlak. Deconvolution of stark broadened spectra for multi-point density measurements in a flow Z-pinch. *Review of scientific instruments*, 82(10):103504, 2011.

[60] Jonathan Robert Weed. *Investigating plasma viscosity with fast framing photography in the ZaP-HD Flow Z-Pinch experiment*. University of Washington.

[61] R Yamada. Chemical sputtering yields of graphite. *Journal of Nuclear Materials*, 145:359–363, 1987.

VITA

Eleanor Forbes was born in Rochester, New York in 1994. Her family moved to the Pacific Northwest in 1999. Her interest in science fiction developed into a passion for STEM classes at Port Townsend High School. She graduated in 2012 and moved to Seattle to pursue a degree in Aeronautics and Astronautics at the University of Washington. Spurred by encouragement from the undergraduate academic adviser for the A&A department, she joined the ZaP Flow Z-Pinch Laboratory in 2014 as a sophomore. She continued working in the ZaP lab for the rest of her undergraduate tenure, in addition to completing an internship at the Princeton Plasma Physics Lab. She earned a Bachelors of Science in 2016. She remained at the University of Washington to further her work on the ZaP-HD experiment, earning a Doctor of Philosophy from the William E. Boeing Department of Aeronautics & Astronautics in 2020.